EUV/FUV Sounding Rocket Observations of Epsilon CMa to Better Constrain the B Star Contribution to Ionization in the Universe

by

Nicholas Erickson

B.S., The College of New Jersey, 2014

M.S., The University of Colorado, 2020

A thesis submitted to the

Faculty of the Graduate School of the

University of Colorado in partial fulfillment

of the requirements for the degree of

Doctor of Philosophy

Department of Astrophysical and Planetary Sciences

2021

Committee Members:

James Green, Chair

Tom Ayres

Brian Fleming

Kevin France

Scott Palo

Erickson, Nicholas (Ph.D., Astrophysics)

EUV/FUV Sounding Rocket Observations of Epsilon CMa to Better Constrain the B Star Contribution to Ionization in the Universe

Thesis directed by Prof. James Green

Hot star models are foundational for understanding the ionizing outputs of star forming galaxies and the contribution of stars to ionization in the Universe across cosmic time. When tested against 505-730 Å EUVE observations of B star Epsilon CMa, these hot star models appear to underpredict hot star EUV flux by a factor of 10-20×, calling into question their accuracy in predicting the strength of the B star contribution to ionizing flux in the Universe.

I have obtained the first-ever observation of a hot, massive, ionizing star (Epsilon CMa) in the critical 730-900 Å bandpass in which neutral hydrogen is most sensitive to ionization. By comparing this new, highly-ionizing spectrum to stellar models generated using the range of published stellar parameters of Epsilon CMa, the goal of this work is to determine if and to what extent these models fail to correctly predict the most ionizing fluxes of massive hot stars, and whether the role of B stars as sources of large-scale ionization in the Universe needs to subsequently be revised.

I constructed, calibrated, and launched the DEUCE sounding rocket to obtain this first-ever spectrum of Epsilon CMa near the Lyman Limit and allow the predictive power of hot star models to be more comprehensively tested and appraised in the EUV. In this thesis, I discuss the motivations for this observation, the construction and calibration of the the DEUCE instrument, the DEUCE launches and the reduction of their data, and the accuracy of hot star models when compared to these data in the EUV.

Dedication

Thank you to the many, many people who have made this thesis possible. If I look back at the adventure of the last six years, I'm extremely moved by the help, support, and encouragement I've received from so many people in so many ways. I'm humbled and extremely grateful for all of your help. Thank you.

Thank you to my parents. You never left me alone in the past six years, and this support meant the world to me. Thank you for always being there, for the uncountable phone calls, for your prayers and love, and for never letting me forget the Road on which I have been walking throughout this beautiful adventure.

Lastly, thank you to Jim Green. Jim, your support and example have meant so much to me while working on DEUCE and this thesis. I have learned immensely from you in these years, on both a personal and a professional level. You have given me a foundation of confidence, experience, critical thinking, and sensibility that I know will serve me for my entire life. You've been an example to me of how to be precise, yet reasonable, authoritative, yet not despotic, hard-working, yet enjoying the beauty of life and the process. Thank you for being such an awesome example of a good, generous, kind person doing amazing work– it's an example that means a lot to me. I'm moved and will be forever grateful for having been your student. Thank you.

Acknowledgements

I gratefully acknowledge NSROC and the personnel at Wallops Flight Facility and White Sands Missile Range who helped coordinate, integrate, launch, and recover the DEUCE payload. Thank you to Sensor Sciences and Oswald Siegmund for a fantastic MCP detector and help with its troubleshooting and testing. Thank you to Robert Kane for the original DEUCE mechanical design, as well as Michael Klapetzky for design work and support later on in the DEUCE life cycle. Thanks to Nicholas Nell for repeated help with anything and everything electronic, and for keeping me humble throughout the entire process. Thank you to Keri Hoadley, for being my original mentor and helping me to learn the ropes under CHESS-2. Thank you to Nick Kruczek, for your sharing of expertise and occasional help on DEUCE and for the start of my education in Rocket League. Thank you to Emily Witt, for all of your help on the DEUCE build up and launches.

Thank you specifically to the many amazing undergraduates who helped on DEUCE in a variety of essential ways: Devin Bazata, Melissa Buckley, Christian Carter, Christopher Creery, Liam O'Connor, Elise Hobbs, Matthew Lehmann, Emily Levis, Jarrod Puseman, Nicholas Renninger, Alex Sico, Jack Swanson, James Wiley, Jacob Wilson, and Samantha Valenteen.

Thank you to Brian Fleming, for your science discussions, general support, and helpful advice in critical moments over the past years. Thank you to Kevin France, for similar support at a critical moment in the early DEUCE life cycle.

Thank you especially to Mike Kaiser– your cheerful, kind, and helpful presence over the course of the thesis made such a difference in my day to day work. Thank you so much for the good-natured, positive atmosphere you brought to my time at CASA ARL.

Contents

Chapter

Tables

Table

Figures

Figure

Chapter 1

Introduction

1.1 Introduction to O and B-type stars

O and early-B-type stars are extremely hot (>20,000 K), luminous (>10^4 $L_\odot$), massive (>10 $M_\odot$) stars which produce significant amounts of their flux below 912 Å, at energies capable of ionizing neutral hydrogen [90]. These energetic stars have an outsize effect on their environments on both local and large scales. On smaller scales, such stars inject large amounts of energy and momentum into the interstellar medium (ISM) through protostellar outflows, stellar winds, ionizing radiation, and supernovae [62], significantly impacting the pressure, temperature, velocity, and ionization state of their surroundings [79]. The Local Bubble in which the Sun resides, for instance, has been profoundly shaped by the presence of such stars [69], specifically B-type star Epsilon CMa, as described in Section 1.6. On a larger scale, O and B-type stars create vast shells and bubbles of hot, ionized H II regions [81] and play a fundamental role in the mass and energy balance of galaxies, helping to regulate star formation through galactic feedback [80].

1.2 The metagalactic ionizing ultraviolet background

On the largest scales, OB stars play a critical role as contributors to the metagalactic ionizing ultraviolet background (UVB), the multi-directional, sub-912 Å radiation field pervading the Universe. The developing UVB was directly responsible for originally ionizing the intergalactic medium (IGM) between z=15-30 and z=6 [70, 78], and it continues to maintain the ionization state of the modern and low-z Universe in the face of recombination [8]. The UVB plays a fundamental role

in reionization modelling and theory, where it is influenced by time-varying factors including the number and density of ionizing sources such as star forming galaxies (SFGs) and active galactic nuclei (AGN), the escape fraction of ionizing photons from these sources, and the opacity of the IGM. On a more general level, the strength and hardness of the UVB influences the physical properties of the IGM [103] and is a fundamental input for cosmological hydrodynamical simulations investigating the ionization and cooling of the IGM [35] and simulating the Universe on a large scale. In cosmological studies, the UVB is used in ionization-correction of observations of neutral hydrogen and ionized species like O VI to determine the total elemental and overall baryon content of the IGM in different phases [104]. Understanding the IGM's state and evolution over time, and thus the state of the 70+% of the known baryonic matter in the Universe that it holds [87], requires understanding the UVB and the sources that generate it.

1.3 Hot star contribution to the UVB

Hot stars have played an important role in the generation of the UVB across cosmic time. It is generally accepted that the energetic photons that reionized the Universe were produced by a mix of AGN and the hot stars present in SFGs (Figure 1.1), but the contribution of each class of object continues to be a subject of debate [76, 27, 75].

Hot stars in SFGs are proposed to have been the dominant sources enabling reionization [75, 23], although their exact contribution is highly dependent on the escape fraction of ionizing photons from their local environments into the IGM. Under certain conditions, however, AGN are also proposed to significantly contribute to or even dominate reionization [76]. AGN have been proposed to dominate UVB production for z<=3 [48, 23], but SFGs and the hot stars that comprise them may also play an important role even at these lower redshifts [103, 109]. While there is no current consensus as to the exact contribution of AGN and star forming galaxies to the UVB at low and high redshifts, it is certain that star forming galaxies are important potential contributors to the UVB that must be studied and taken into account in order to understand the ionization state and history of the Universe.

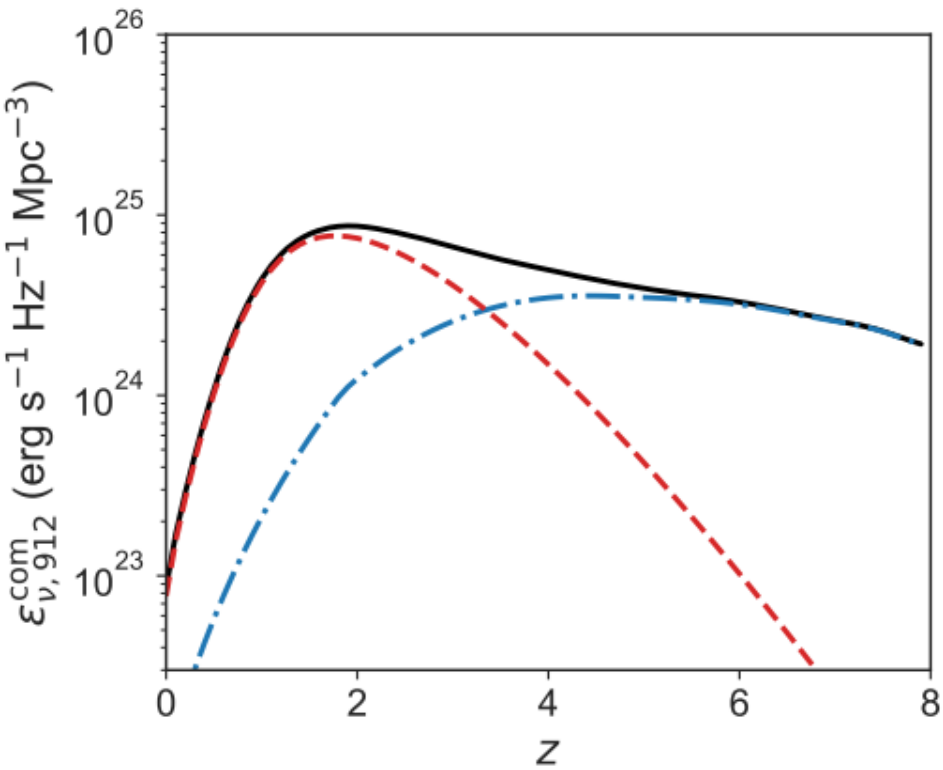

Figure 1.1: A figure taken from [23] showing proposed AGN (red), SFG (blue), and total (black) 912 Å emissivities as a function of redshift. In these specific models, AGN are proposed to dominate UVB production for z<3, while SFGs provide the majority of ionizing photons for early reionization. The exact relative contribution of AGN and SFGs to ionization at different times remains debated.

1.4 Stellar models: a foundation

Understanding how the hot stars in SFGs contribute to the UVB in both modern and high-z epochs comes down to to a foundation upon which estimates of SFG ionizing fluxes are based: individual stellar models. Typical UVB models [48, 23] consider the contribution of SFGs by taking observed and interpolated galaxy luminosity functions, integrating them over a range of luminosities, and assuming a specified ionizing flux output for each luminosity class of galaxy. These ionizing fluxes come from stellar population synthesis codes like GALAXEV [7], STARBURST99 [66], or BPASS [21] that combine stellar population tracks predicting individual stellar parameters (e.g., T, log g, R, M, etc) as a function of time with SFG galaxy initial mass functions (IMFs) predicting the number of stars in a galaxy as a function of stellar mass. Essentially, these codes

follow simulated populations of stars through their stellar life cycles, tracking the evolution and resulting stellar parameters of these stars as the SFG ages and evolves.

To convert these simulated populations of stars with time-varying parameters into estimates of ionizing flux that contribute to the UVB, the listed population synthesis codes utilize Kurucz [63, 13] or similar stellar model atmospheres to generate a predicted ionizing spectrum for each hot O and B-type star in the population at each stage of its evolution. These fluxes, generated for individual stars at specific times, are then summed over time (Figure 1.2) and across the population before being combined with factors like escape fraction to estimate the time-dependent ionizing output of SFGs (Figure 1.3). Ultimately, then, the flux outputs of SFGs as estimated for the purposes of understanding modern and high-z ionization come down to the synthesized, combined predictions of a multitude of individual stellar models at ionizing wavelengths. A critical foundation supporting the understanding of the contribution of SFGs to the UVB is thus the predictive power of these individual stellar atmospheric models in estimating the strength of the ionizing spectra produced by individual hot O and B type stars.

Changes in these underlying stellar models can have significant effects on the predicted strength of SFG contributions to the UVB. The correction of stellar models for rotation [103, 43] was found to increase the predicted LyC production of stellar populations by 50%, while accounting for binarity, which increases hot stars' main-sequence lifetimes, boosted escape fractions and resultant hot star ionizing outputs by factors of 4-10 [73]. Both of these increases were proposed to significantly change the contribution of SFGs to the onset and maintenance of reionization. The predictions of individual stellar models can clearly have a fundamental impact on estimates of the stellar contribution to the UVB and the subsequent understanding of the time-dependent state of the IGM.

1.5 A lack of observations

Given the dependence of estimates of the SFG UVB contribution on individual stellar models, it is important that these foundational models be as accurate as possible. Models are tested by their

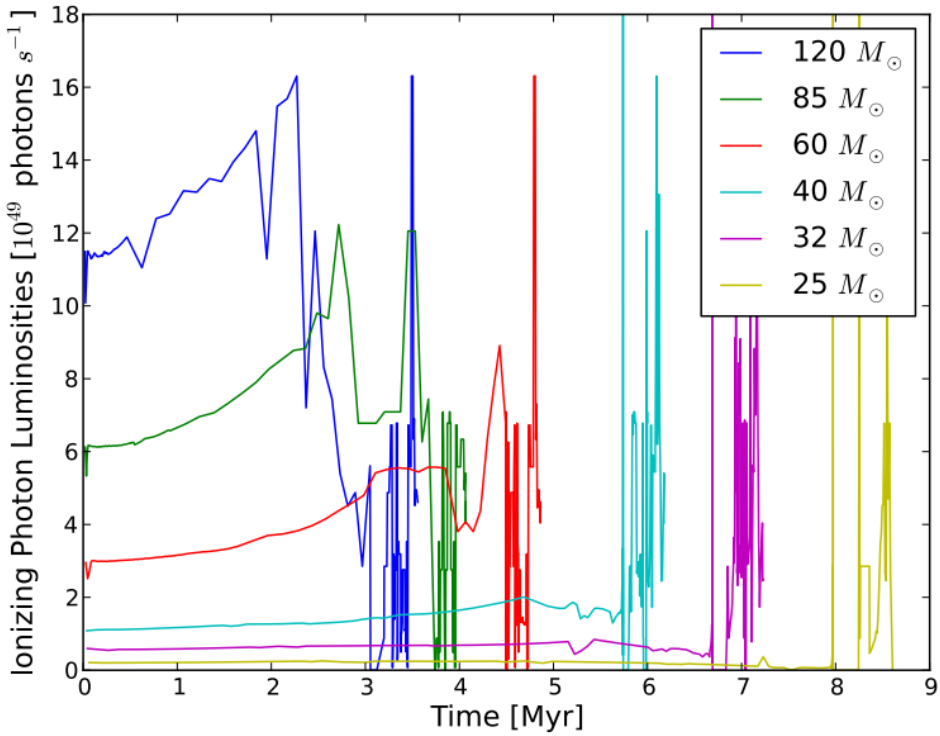

Figure 1.2: Estimates of ionizing photon luminosities as a function of time for select massive stars, taken from [114]. These luminosities represent the summation of individual stellar model spectra of each mass star generated at a variety of physical stellar parameters as the star progresses through its life cycle and eventually dies. These individual outputs form the basis for SFG ionization modeling, as in Figure 1.3.

predictive power compared to data in the form of observations, and in this respect, these stellar models run up against a fundamental problem: **no observations of hot O and B-type stars in the most highly ionizing wavelengths from 730-912 Å have ever been made.** There has therefore been no observational verification of the predictive power of these stellar models at the wavelengths which most strongly ionize neutral hydrogen in the Universe.

This lack of observations is not without reason; observations of hot stars below 912 Å are very difficult, primarily due to the strong attenuation of hot star ionizing fluxes by neutral hydrogen present in the local ISM between Earth and even the nearest hot stars. For atomic hydrogen in the n=1 level undergoing a bound-free transition due to interaction with an ionizing photon of wavelength <912 Å, the attenuation of ionizing flux is defined [108] as:

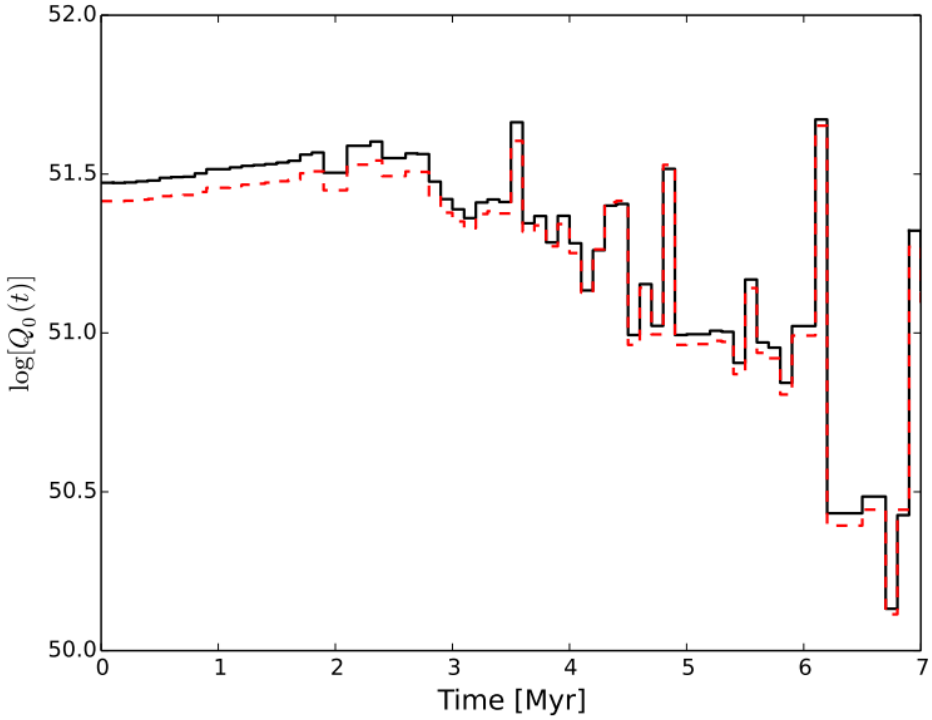

Figure 1.3: Estimates of the ionizing photon production rate ($Q_0(t)$, [$photons/s$]) of two representative clusters of mass 100,000 $M_\odot$, taken from [114]. These are essentially the outputs of Figure 1.2, summed over a galaxy IMF. Estimates of SFG ionizing output like these are used to calculate the stellar contribution to the UVB, and ultimately depend on the summation of the predicted ionizing spectra of a multitude of individual single hot star models.

$$I_\nu = I_\nu(0)e^{-Ns_\nu}, \tag{1.1}$$

where $I_\nu(0)$ is the emitted intrinsic flux, I_ν is the observed flux, N is the attenuating neutral hydrogen column density (N(H I)) along the sightline, and the absorption coefficient s_ν takes the form:

$$s_\nu = 7.91 \times 10^{-18}(\frac{\nu_1}{\nu})^3 g_{1f}, \quad g_{1f} = 8\pi 3^{1/2}(\frac{\nu_1}{\nu})\frac{e^{-4z\ cot^{-1}(z)}}{1-e^{-2\pi z}}, \quad z = \sqrt{\frac{\nu_1}{\nu-\nu_1}}, \tag{1.2}$$

where ν is the frequency of the ionizing photon, ν_1 is the reference frequency of a 912 Å photon, and g_{1f} is a 'Gaunt Factor'.

This continuum absorption is a very strong function of N(H I) and is strongest at the Lyman

Limit (912 Å), decreasing at higher energies. To demonstrate its strength, it is informative to consider Zeta Ophiuchi, one of the nearest O stars to Earth with a distance of 112 pc and an N(H I) column density of 5×10^{20} cm^{-2} [47]. With a Gaunt Factor of approximately .797 at 912 Å, the transmission fraction of its emitted 912 Å flux as observed at Earth calculated using equations (1) and (2) is e^{-3153}. For an even lower theoretical N(H I) column density of 5×10^{18} cm^{-2}, the transmission fraction is still e^{-32}. These calculations show the impossibility of direct observation of ionizing flux for almost all local hot stars in the ISM, for which sightlines with column densities $> 5 \times 10^{18}$ cm^{-2} are common [47]. For this reason, despite their obvious value for testing stellar models and helping to verify the estimated ionizing outputs of SFGs, hot-star observations at wavelengths near the Lyman Limit have historically not been made.

1.6 Epsilon CMa

Epsilon Canis Majoris (CMa) is a hot (20-25,000 K) B2-II type star located at a distance of 124 pc. Against expectations, observations in 1992 with the ROSAT satellite detected strong 520-730 Å photometric flux from Epsilon and nearby B1 II-III star Beta CMa [52]. Subsequent photometric survey and 70-730 Å spectroscopic observations with the EUVE satellite found Epsilon to be the brightest EUV source in the sky, outshining the previous brightest source, white dwarf HZ 43, by a factor of 30 [10, 116]. The observability of Epsilon's EUV flux was discovered to be due largely to its highly sparse sightline, N(H I) $2 - 12 \times 10^{17}$ cm^{-2}, which is proposed to have been created by Epsilon CMa itself as its ionizing radiation carved out a Stromgren sphere that includes the location of the Sun and Earth. The tenuous N(H I) sightline to Epsilon and Beta CMa evidenced by the ROSAT and EUVE observations is essentially unique in the local ISM for hot, massive stars: Epsilon and Beta CMa are the only known O or B-type stars with low enough N(H I) sightlines to allow for their EUV fluxes at the Lyman limit to be directly measured at Earth. Taking advantage of this unique sightline, the EUVE observations below 730 Å determined Epsilon to be the dominant source of 450-730 Å ionizing photons in the local ISM near the Sun [116], with its EUV flux playing a central role in shaping the ionization state, temperature, and structure of

the local ISM [69].

Outside of their importance in ascertaining Epsilon's importance to the local bubble, the EUVE observations were extremely valuable in allowing for the first ever direct test of the predictive power of hot star models at the ionizing wavelengths constituting the UVB. Based on contemporary estimates of Epsilon's stellar parameters and sightline N(H I) column, Vallerga et al. [10] compared Epsilon's EUV spectrum to a 21,000 K, log g =3.2 Kurucz stellar model with a column density of 1×10^{18} cm^{-2}. Rather than matching the observed ionizing flux of Epsilon CMa, **the 21,000 K model underpredicted the observed spectrum by factors of 10-20**$\times$ (Figure 1.4). This discrepancy was proposed to be the result of the stellar model underpredicting the temperature of Epsilon's outer atmosphere [10], with the authors concluding that the Kurucz models significantly underestimated the EUV portion of Epsilon's flux while generally matching its FUV flux seen in other observations (e.g. from the IUE satellite [4]).

1.7 Implications

The proposed underprediction of Epsilon CMa's EUV flux by stellar models as demonstrated by comparison to the EUVE data has important potential implications for understanding the role that hot stars play in local and high-z ionization. If the observation-model discrepancy found by EUVE is valid and Epsilon CMa is assumed to be a representative B star, then the hot star models used as the basis for understanding the SFG and hot star contribution to the UVB may be in need of revision and might significantly under-predict the ionizing flux contribution of B stars to SFG ionizing outputs. B stars are typically ignored as ionizing sources due to their reduced ionizing photon production compared to hotter O stars [114]. If the EUV fluxes of B stars are truly being underpredicted by a factor of 20$\times$, however, their role and importance as sources of ionizing photons may have to be reconsidered. Since the winds and supernovae of short-lived, massive O stars are thought to generate feedback that increases galactic escape fractions [50], it is also possible that longer lived B stars may have higher average escape fractions than initial O stars, giving them a more significant contribution to the ionizing flux escaping galaxies and actually impacting the IGM.

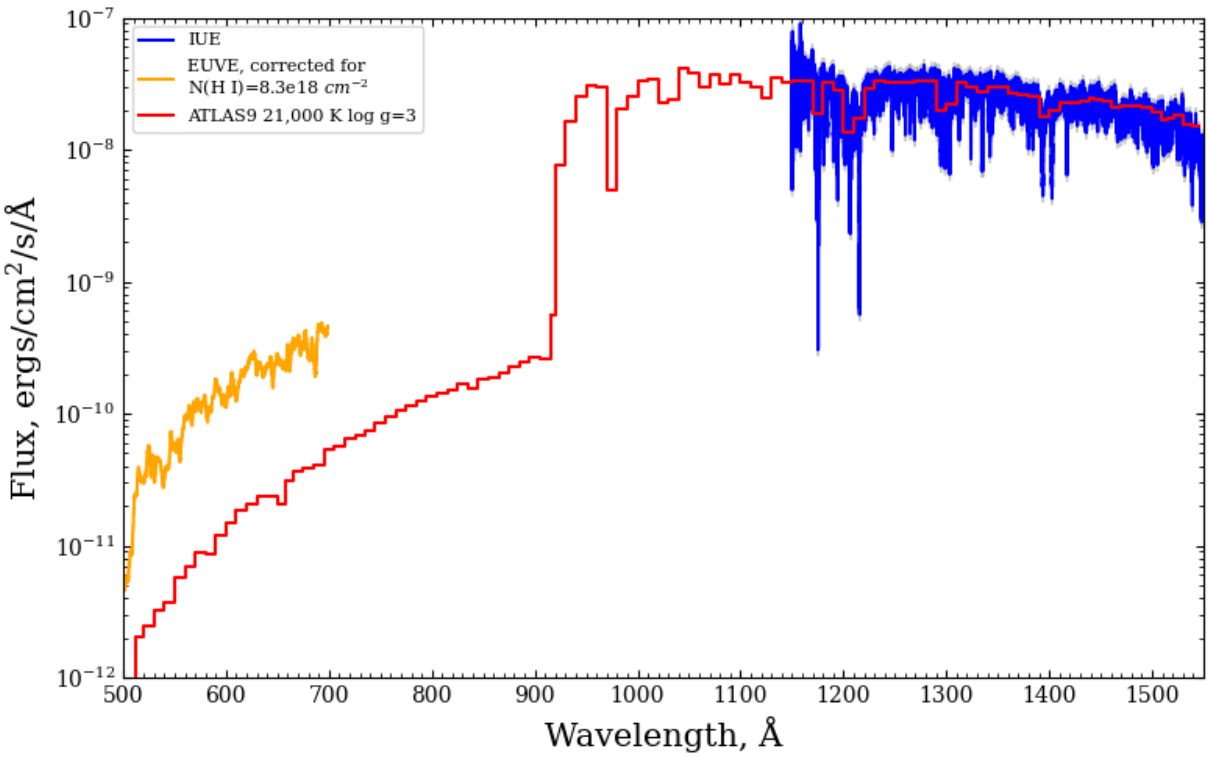

Figure 1.4: The EUVE observations of Epsilon CMa from 504-730 Å compared to an ATLAS9 Kurucz model generated using a 21,000 K, log g=3 model with a N(H I) attenuation of 8.3×10^{17} cm^{-2}. The model underpredicts Epsilon's EUV flux while generally fitting the FUV portions of its spectrum from the IUE satellite.

Finally, if stellar models are under-predicting B star ionizing spectra, it is entirely possible that they are also under-predicting the EUV spectra of brighter, more highly ionizing O stars, which have also never been tested observationally. If B star or general hot star EUV flux is truly more significant than previously estimated, then accounting for this boost of ionizing output in SFG modelling could change the paradigm of how SFGs contribute to UVB production across cosmic time.

1.8 Further steps

EUVE's observations of Epsilon CMa have proposed a potentially alarming failure of stellar models in correctly predicting hot star EUV flux. To understand whether this proposed discrepancy

truly warrants a revision of the B-star contribution to ionizing flux in the UVB, however, requires further confirmation and analysis. While groundbreaking, the EUVE observations were ultimately limited by the satellite's bandpass, which had an upper limit of 730 Å. This limit means that no EUV observations currently exist from 730 Å to the edge of the Lyman Continuum at 912 Å, where neutral hydrogen is most sensitive to photoionization. It is thus currently uncertain if and how severely the discrepancies proposed below 730 Å continue into this critically ionizing region of the spectrum that has the strongest impact on the stellar contribution to the hydrogen-ionizing UVB.

Observations above 730 Å provide a second important advantage over the EUVE spectra that similarly comes from the high ionization efficiency of photons at these wavelengths. The high λ-dependent photoionization cross section of hydrogen that makes the 730-912 Å regime especially important for understanding large-scale ionization also means that it is the most sensitive to the effects of attenuation by *local* neutral hydrogen. This increased sensitivity allows the attenuating effect of Epsilon's N(H I) sightline on observations to be more precisely constrained, modelled, and removed from observations, generating a more fiducial intrinsic hot-star spectrum to compare to models.

Lastly, the published comparison between EUVE's observations and the Kurucz models assumed a single set of values for Epsilon CMa's temperature, surface gravity, and N(H I) column. Although they were considered by the authors to be the best estimates known at the time, these assumed values had associated error and were not necessarily definitive, even at that time. Observations in the intervening time since EUVE's observations have produced additional estimates of Epsilon CMa's stellar parameters and N(H I) values, and these new estimates must also be considered in any model-observation comparisons. A thorough analysis of the proposed failure of stellar models necessarily needs to include the complete range of estimated stellar parameters for Epsilon CMa to understand if there is a failure of the models themselves, or of the assumptions of Epsilon's parameters used at the time of the EUVE observations.

1.9 This thesis

Understanding the UVB ionizing background that shaped and continues to shape the conditions of a significant fraction of the Universe requires understanding the contribution of star forming galaxies to ionization across cosmic time. Simulations of the ionizing output of SFGs depend on a foundation of individual stellar models which estimate the ionizing outputs of hot stars up to 912 Å. When tested for the first time against EUVE observations of Epsilon CMa, these foundational stellar models appeared to underpredict B-star ionizing fluxes by a factor of up to 20, which, if valid, could significantly impact the understanding of how hot stars in SFGs contribute to the UVB and impact ionization in the Universe. To supplement the EUVE data and more sensitively test the degree to which stellar models underpredict hot star ionizing fluxes in the EUV, it would be of great value to obtain new observations of Epsilon CMa extending into the critically ionizing, never before observed 730-912 Å regime and test them against stellar models generated using a range of modern estimates of the parameters of Epsilon and its sightline.

In this thesis I present, for the first time, direct observations of Epsilon CMa from 700-1150 Å taken with the DEUCE sounding rocket. These observations fill the existing observation gaps in Epsilon's EUV/FUV spectrum and for the first time ever allow for a direct comparison between observations and the stellar model predictions of ionizing outputs in this critical wavelength regime. By comparing these new observations of Epsilon CMa up to the Lyman Limit against stellar models, I test if and how the proposed 20× discrepancy between EUV observations and stellar models remains valid at these critically ionizing wavelengths, and I discuss the implications of this analysis on the role that hot stars are currently proposed to play in generating the UVB and helping to ionize the Universe.

Chapter 2 of this thesis describes the design, construction, testing, and calibration of the DEUCE sounding rocket that generated these new observations. Chapter 3 describes the successful launch of the DEUCE payload and the reduction and calibration of its flight data, ending with the presentation of the new, flux-calibrated spectrum of Epsilon CMa from 700-1150 Å. In Chapter 4, I

utilize χ^2-fitting to compare the new DEUCE EUV observations against a variety of stellar models generated over the range of estimates of its stellar parameters and N(H I) sightline. Chapter 4 ends with a discussion of the implications that the results of this model fitting have on the current understanding of the role hot stars play in contributing to the UVB, along with future work to be considered.

Chapter 2

DEUCE

The *Dual-channel Extreme Ultraviolet Continuum Experiment* (DEUCE) is a rocket-borne, ultraviolet spectrograph that launched in October 2017 and December 2018 as NASA/CU missions 36.311 UG and 36.331 UG out of White Sands Missile Range (WSMR).

The science case, targets, observation challenges, and instrument overview of the mission are introduced in Section 2.1. The payload optics are discussed in Section 2.2, followed by a description of the testing, ground, and vacuum systems that supported the payload development in Section 2.3. The calibration of the payload is described in Section 2.4. Section 2.5 describes major events in the payload life cycle leading up to its launches, which are outlined later in Chapter 3.

2.1 Introduction

2.1.1 Science case

As described in Chapter 1, an important open question in astrophysics is how the ionization fraction of the intergalactic medium (IGM) was established and is maintained in the modern Universe. From the z$\sim$7 epoch of reionization [97] to the present, the universe has remained highly ionized due to the sustained production of energetic photons from a variety of astrophysical sources including star forming galaxies and active galactic nuclei [48]. Despite continued improvements in simulations and observations, the mechanics of this sustained ionization remain only partially understood [103, 58]. This is due to several key knowledge gaps, including the emissivities [114], number, and distribution of the sources producing ionizing photons [102, 92], as well as the fraction

of energetic photons that are able to escape their local environment and ionize the IGM [74].

DEUCE was designed to address the first of these limitations, with a focus on the emissivities of the hot stars driving the ionization outputs of star forming galaxies [111]. Despite the importance of these stars in ionization upkeep, no calibrated stellar flux measurements have been made for an individual O or B-type star in the 730-912 Å region that most effectively ionizes neutral hydrogen. This lack of observations generates uncertainty in the stellar models that form a basis for larger scale simulations used to understand the ionizing outputs of galaxies.

No O stars have sufficiently low N(H I) column densities to allow for their EUV observation at Earth. DEUCE's science goal is to directly address the uncertainty of stellar EUV models by obtaining the first-ever 730-912 Å flux-calibrated spectra of the only two hot, ionizing stars with a low enough N(H I) column to be observed at Earth, B stars Epsilon and Beta CMa. With these new observations, DEUCE will allow for testing and calibration of hot star models, helping to better constrain the role hot stars play in the sustained ionization of the Universe.

2.1.2 Targets

Direct observation of the EUV emission of a distant star requires careful target selection, as the interstellar medium (ISM) surrounding the Sun is replete [30] with neutral hydrogen (H I), an effective absorber of EUV photons below 912 Å. For this reason, most potential targets experience high attenuation of their EUV radiation as viewed from Earth. This includes all highly-ionizing O stars, which would otherwise be ideal targets for the DEUCE mission.

Sparse ($< 5 \times 10^{18}$ cm^{-2}) H I sightlines to massive, ionizing stars in the local ISM are so rare [47] that direct EUV observation is only feasible for the two stars chosen as the DEUCE targets: B stars ϵ and β CMa. The sustained ionizing flux of Epsilon CMa has highly ionized the sightline between it and Earth [46], carving out a Stromgren sphere that includes the Solar neighborhood [69] and permitting direct observation of ϵ and β's EUV fluxes with only partial attenuation. A set of modern estimates of stellar parameters for ϵ and β CMa are shown in Table 2.1. For a full compilation of previous UV observations of Epsilon and values of its stellar parameters, see

Appendices B and C.

	ϵ CMa	β CMa	Ref.
Spectral Type	B1.5 II	B1 II/III	[14]
V (mag)	1.50	1.97	[14]
Temperature (K)	22,500 ± 300	24,700 ± 300	[14]
Distance (pc)	124.2 ± 2.2	151.2 ± 4.9	[118]
Mass (M_{sun})	$13.1^{+1.0}_{-0.9}$	$12.0^{+0.3}_{-0.7}$	[14]
Radius (R_{sun})	$12.0^{+1.7}_{-1.5}$	$7.4^{+0.8}_{-0.9}$	[14]
Log g	3.40 ± .08	3.78 ± .08	[14]
N(H I) (cm^{-2})	$7 \times 10^{17} - 1.2 \times 10^{18}$	$2 - 2.2 \times 10^{18}$	[11, 10]

Table 2.1: Estimates of stellar parameters for ϵ and β CMa

2.1.3 Challenges

Observation of ϵ and β CMa presents multiple challenges that must be taken into account. Even though the two stars' H I sightlines are some of the most tenuous ever observed towards hot stars, sufficient material is present to cause an attenuation of more than 90% across the DEUCE EUV bandpass, increasing towards 912 Å. This attenuation requires observation with high instrument throughput.

ϵ CMa also exhibits an approximately 500× increase in flux moving from the fainter EUV to the brighter FUV, due to photospheric absorption of the <912 Å radiation by hydrogen. This increase creates a dynamic range problem when trying to record the full spectrum in a single observation. If an experiment is optimized for the bright FUV, the faint EUV will be too dim and will never be registered. Similarly, if the faint EUV is optimized, the brighter FUV has the potential to overwhelm the detector with very high count rates. The DEUCE science experiment was previously attempted for ϵ CMa on several occasions [42, 120]. In each case, scattered light from the bright FUV prevented the capture of an accurately flux-calibrated EUV spectrum (Figure 2.1). These previous observations highlight the importance of managing the 912 Å dynamic range issue and its associated scatter risk for any instruments seeking to observe ϵ and β in the EUV and FUV.

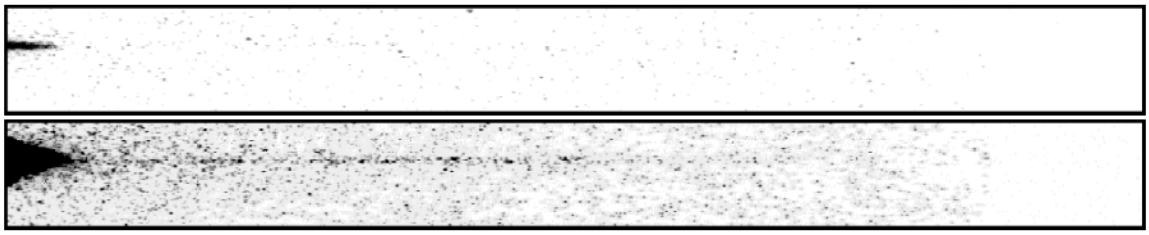

Figure 2.1: Two raw exposures of ϵ CMa's Lyman jump from the UVSTAR mission [42], spanning 935-535 Å across the image from left to right. The 912 Å decrease in flux is visible as the sharp change in brightness at image left. In the top image, the bright >912 Å FUV is correctly exposed, but the fainter <912 Å EUV is not visible with such a short exposure. In the bottom image, the exposure is lengthened to increase the strength of the EUV signal, but the much brighter FUV saturates the detector while also scattering onto the EUV, hindering accurate flux calibration.

2.1.4 Instrument overview

The DEUCE instrument (Figure 2.2) was specifically designed to address the challenges faced by previous missions and to produce the first accurately flux-calibrated spectra of ϵ and β CMa across the Lyman limit from 700-1150 Å.

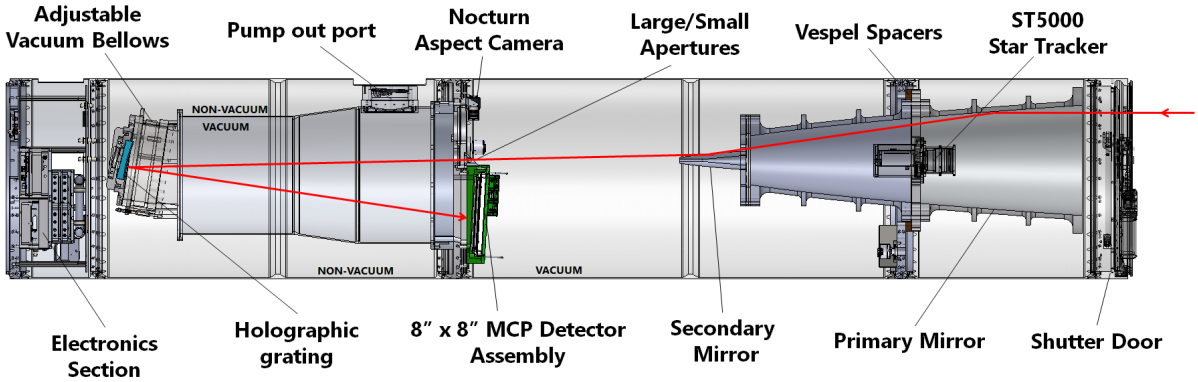

Figure 2.2: The DEUCE payload. Light enters from the right before striking the primary and secondary mirror at grazing incidence and coming to a focus on the dual set of apertures. Light continues to a holographic grating positioned on a 1 m diameter Rowland circle before proceeding to the large format microchannel plate detector. Detector signals are amplified locally and routed to an electronics section for processing.

DEUCE is a UV spectrograph consisting of a grazing-incidence telescope, a holographically-ruled diffraction grating, a large-format microchannel plate detector, and a set of entrance apertures

that generate two channels in the form of spectra offset in the cross dispersion direction. One channel, generated by a larger, low-resolution aperture, covers the 696-895 Å EUV regime with low resolving power (R∼180), while the second channel results from a smaller aperture and covers the 696-1145 Å FUV regime with medium resolving power (R∼1850). The spectral coverage of both channels is constrained by an asymmetric detector mask at higher wavelengths and by shadowing from a detector mounting plate at shorter wavelengths. The telescope focus, entrance apertures, grating, and detector are all positioned on a 1 m diameter Rowland circle.

The DEUCE experiment is housed in a 3 m long, 55.9 cm diameter rocket skin, weighing 227 kg. DEUCE presents a net effective area (including aperture transmission) of 3-5 cm^2 in the EUV and .1-.2 cm^2 in the FUV, with the overall effective area varying complexly across the observed bandpass. Since DEUCE operates in the UV, the payload is sensitive to hydrocarbon contamination, and strict cleanliness guidelines were followed for its entire buildup and operation. DEUCE's design placed a strong emphasis on maximizing throughput while simultaneously minimizing the risks posed by the EUV/FUV dynamic range of ϵ and β CMa. The DEUCE optical components and the steps taken to achieve the stated design focus are presented in the following sections.

2.2 Optics

2.2.1 Telescope

The DEUCE telescope (Figure 2.3) is an f/15, Wolter-II style grazing incidence optic, with a 30 cm diameter aperture and a focal length of 4619 mm. The primary mirror consists of two confocal parabolic segments and is made of 6061-T6 aluminum with a polished electroless nickel overcoat. The outside-illuminated, hyperbolic secondary mirror is also made of 6061-T6 aluminum, but with a 250 Å-thick sputtered SiC overcoating originally deposited for a previous flight in order to minimize reflectance of wavelengths below 136 Å [9]. The telescope surface roughness was estimated [123] as 10-30 Å, and the grazing angle for photons transiting the telescope varies between 3-8 degrees. The overall physical length of the telescope is 1132 mm, with the primary mirrors measuring 959

mm, the secondary mirror measuring 173 mm, and the final focal point at a distance of 574 mm from the last edge of the secondary. The telescope weighs 43 kg, about a fifth of the total payload mass.

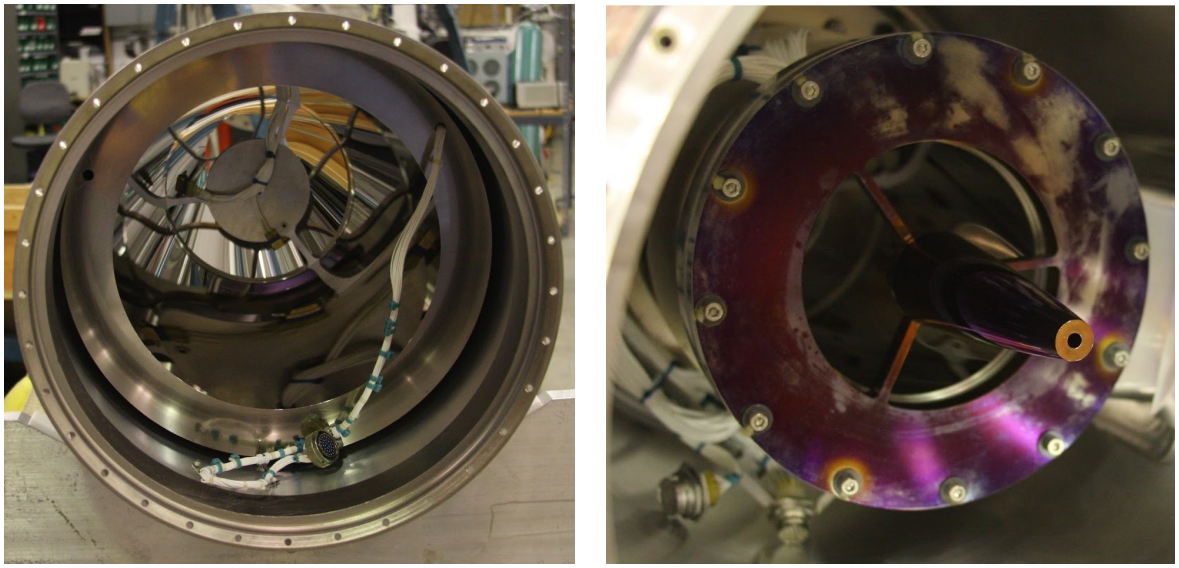

Figure 2.3: The grazing incidence telescope for DEUCE. Left: The nickel-coated primary in its original 43.2 cm skin, viewed from payload fore, showing both mirror segments as well a a temporary metal disk positioned at the central mounting location for the star tracker. Right: The SiC-coated, outside-illuminated secondary mirror, viewed from payload rear.

2.2.1.1 Telescope optics

The telescope's long focal length and significant figure error generate a ∼1 cm focal region of constant spot size that lowers the tolerance with which it must be positioned axially with respect to the payload entrance aperture (Figure 2.6). The Wolter-II design, however, creates poor off-axis pointing performance, with a spot that rapidly degrades in quality more than 10 arcminutes off-axis. Due to the Wolter-II mirror shape and figuring errors, the spot displays significant structure (Figure 2.4). The minimum spot diameter observed on the ground was approximately 3 mm, although the in-flight spot appeared noticeably smaller, potentially indicating imperfect collimation in testing optics. Both of these spot diameters are larger than the ∼1 mm spot described in previous missions utilizing the telescope, suggesting that the primary and secondary mirrors might be mildly

misaligned or mis-spaced, or that the telescope was positioned slightly off of its calculated best focus. The spot nonetheless still fit completely into the DEUCE large aperture. It was thus not harmful to the DEUCE science objectives, and no attempt was made to re-position the telescope or realign its segments. Measurements of the spot in the visible and UV show the spot having a broadly similar shape at both wavelengths [123] (Figure 2.4b).

A two dimensional ray trace of the primary and secondary mirror is shown in Figure 2.5.

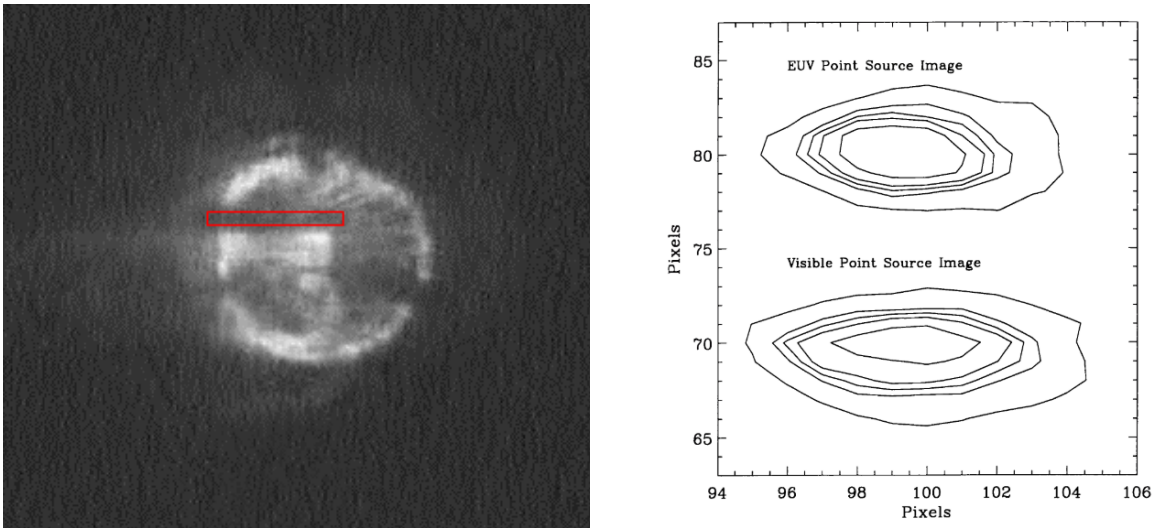

Figure 2.4: Left: A typical spot, ∼2-3 mm diameter, produced by the telescope and imaged through the aspect camera system during the 2018 flight. The red rectangle roughly shows the size of the DEUCE small aperture with respect to the spot. The difficulty in calibrating the small-aperture channel during a flight with slight jitter and spot movement is readily apparent. Right: A comparison of the EUV and visible spot, showing their similar extent and shape, taken from [121].

2.2.1.2 Telescope mounting

The telescope was attached directly to a rocket bulkhead. To prevent its thermal expansion in flight and a subsequent change in focus or alignment, the telescope was thermally isolated from the payload bulkhead by four Vespel spacer rings. To accommodate the footprint of the large MCP detector, the telescope was mounted slightly off-axis and counterbalanced with steel weights mounted to the bulkhead. The telescope was axially positioned so as to keep the spot in its 1

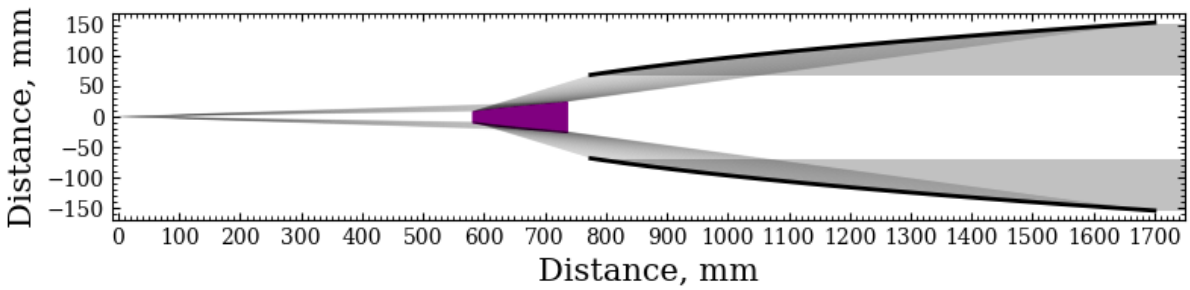

Figure 2.5: A 2D ray trace of Wolter-II telescope generated in Python, showing the primary mirror (black lines) and secondary mirror (purple wedge). Light enters from the right.

cm region of best focus after an expected 7 mm expansion of the telescope section skins due to frictional heating in flight. The payload star tracker (ST5000) was mounted inside the telescope and served to baffle its central axis.

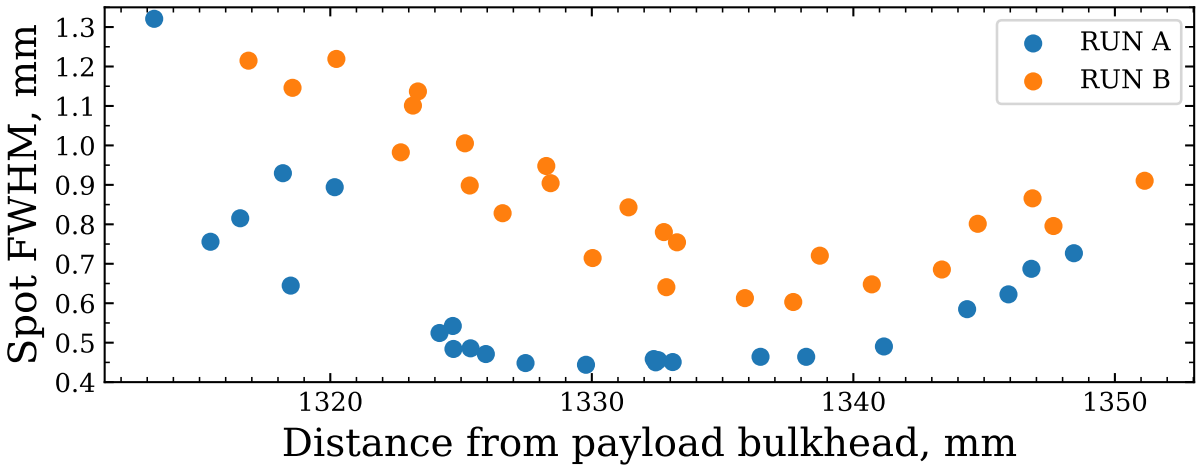

Figure 2.6: The measured focal curve of the telescope, showing the roughly constant spot size it produces across an approximately 1 cm region surrounding best focus.

2.2.1.3 Telescope history and cleaning

The telescope was built in 1987 and has since been used on multiple sounding rocket missions [9, 18, 40, 37, 122, 41, 123, 110, 120]. Additional details on its properties and history can be found in papers describing these flights [9, 123]. Prior to the DEUCE instrument buildup, the telescope

was kept in long-term storage at CU Boulder. Both the primary and secondary were thoroughly cleaned in an isopropyl alcohol rinse and allowed to dry in a clean nitrogen-purged environment immediately prior to installation into the payload.

2.2.2 The entrance apertures

The telescope focuses light onto a mirrored set of entrance apertures (Figure 2.7) manufactured out of AISI 304 stainless steel substrate polished to a reflective finish. There are two apertures; a large 2.83 mm diameter circular aperture subtending 2.1 arcminutes on the sky, and a small 1.5 mm x 17 μm rectangular aperture subtending 1.1 arcminutes x .75 arcseconds. The two apertures were separated by approximately 7 mm or 5.2 arcminutes. In flight, the spot fit cleanly within the large aperture but intentionally overfilled the small aperture in order to suppress the brighter FUV channel.

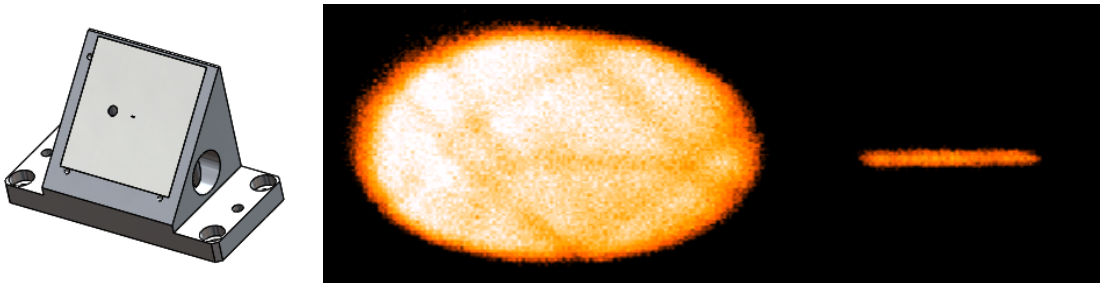

Figure 2.7: Left: a rendering of the aperture holder and the apertures as mounted in the payload. Right: the spots produced by the apertures as imaged on the payload MCP in monochromatic light. The distance between the spots has been reduced for easier viewing. The circular large aperture was projected into an oval shape on the detector due to the 45 degree aperture substrate mount angle.

The large and small apertures feed the same detector and grating, and generate the EUV and FUV portions of the science spectra in low and high-resolution, respectively. Aperture selection is accomplished by the rocket pointing during flight. In flight, the spot fully fit within the large aperture (>99% transmission), while the small aperture allowed between 1 and 5% transmission, depending on spot placement. For the 2018 flight, the large and small apertures had their separation

slightly increased to ensure there was minimal leakage of light into the large aperture when starlight was incident on the small aperture.

The dual-aperture design was motivated by the EUV/FUV dynamic range of ϵ and β. The small aperture was chosen to significantly attenuate the stars' brighter FUV spectra, allowing them to be observed without problematically high count rates. Conversely, the EUV aperture was made large to maximize transmission of the stars' fainter EUV spectra. The accompanying reduction in EUV resolution was not problematic, as resolving individual EUV absorption lines was less important than measuring the unknown EUV continuum flux. To protect against the bright FUV light transmitted by the large aperture, the payload detector was physically masked to block >900 Å light in the low-resolution channel (Section 2.2.7).

2.2.3 Aspect camera

Any light collected by the telescope that did not pass through the apertures was reflected off of the mirrored aperture substrate and imaged by an aspect camera. In this role DEUCE utilized a Nocturn XL CMOS camera by Photonis, which was coupled with an off-the-shelf lens and lens shade and mounted on a custom bracket near the apertures. A small LED was secured behind the aperture substrate, allowing the two apertures to be backlit during testing or flight. The Nocturn field of view was approximately 15 arcminutes on a side, with a platescale of 44 arcseconds/mm, only partially covering the full face of the aperture substrate and centered on the two apertures.

2.2.3.1 Nocturn history and benefits

The 2017 DEUCE flight was the first mission with a Nocturn as the primary aspect camera, and it performed according to expectations, generating and transmitting real-time images of the spot and apertures in flight. Prior to the launch, the camera underwent vibration and optical testing at Wallops Flight Facility, as well as sky testing and heat cycling at CU Boulder. Before the DEUCE flight, the camera was launched as a side-facing test camera on missions 36.323 UG [60] and 36.333 UG [61]. The Nocturn is now flight qualified for future suborbital flights, and has

been used as the primary aspect camera on the SISTINE [28] mission.

The Nocturn was used in place of the Xybion camera system utilized on many previous rocket flights. Its benefits include a lighter weight, smaller size, off-the-shelf availability, analog/digital output, and control over a variety of settings via serial communication. The Nocturn, which is not intensified, has lower sensitivity than the Xybion, but this was not a problem for the bright DEUCE targets.

2.2.4 Grating

The dispersive optic for DEUCE is a 3800 line/mm, holographically-ruled, constant groove density, sinusoidal diffraction grating operating in first order. The 11 x 11 x 1.6 cm grating, manufactured by Horiba JY in December 2015, is made of Corning 7980 fused silica with a radius of curvature of 998.8 mm, focusing its spectrum onto the payload Rowland circle.

The grating was manufactured with a 40 nm gold coating deposited over a chromium adhesion layer but was later re-coated with 38 nm of SiC on top of a 30.5 nm Cr overcoat. The grating is sensitive to hydrocarbon degradation but is not hygroscopic, allowing it to be more easily stored and integrated into the payload. During coating, the grating sustained a corner chip due to differential thermal expansion of the grating and its chamber mount. The damage was deemed to be non-propagating by several optics experts and did not require special treatment. The chip has since remained unchanged through two rocket flights and a litany (>10) of vibration tests.

2.2.4.1 Grating mounting

The grating is held by three titanium struts attached to Invar pads which only contact the glass through epoxy bond faces (Figure 2.8). Each bond was made with Scotch-Weld® 2216 gray A/B epoxy separated into two bond lines for redundancy. As mounted, the angle of the grating normal with respect to incoming light is 14.21 degrees, generated by a 5.54 degree angling of the grating relative to its mount and an additional 8.67 degree angling between the mount and the spectrograph canister.

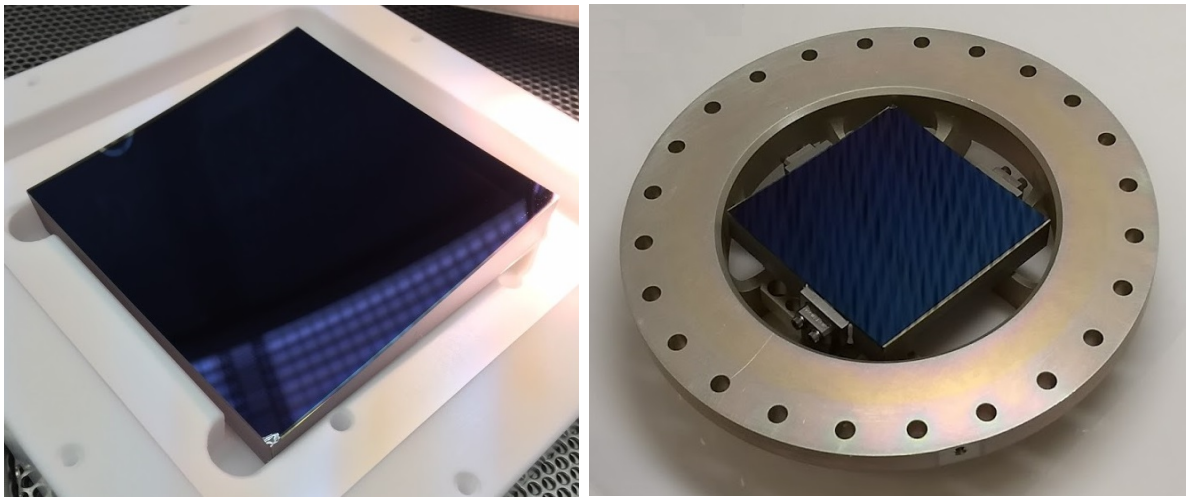

Figure 2.8: Left: The DEUCE grating before mounting, showing the chip in the bottom corner. Right: The grating installed in its flight mount and housing (the 'catcher's mitt'), showing the three contact points via epoxy bond pads.

The bonded grating mount was attached to three 120 degree-spaced turnbuckles with approximately 3 cm of travel, located outside of the vacuum section. Combined with a 20 cm diameter welded bellows, this allowed for orienting and positioning of the grating assembly while maintaining vacuum, which greatly simplified testing and alignment. The spectrograph canister and grating mount can be seen in Figure 2.9.

2.2.4.2 Grating bandpass

Bandpass selection occurred in real time by adjusting the grating tilt via its external turnbuckles while the payload was illuminated with a hollow cathode lamp [91]. The bandpass of the small-aperture FUV channel was set to 696-1145 Å, while the large-aperture EUV channel was set to 696-895 Å. The long wavelength cutoff for both channels is set by the shape of an asymmetric detector mask (Section 2.2.7) which registers the full FUV channel but blocks the EUV channel above 895 Å. While the EUV channel lacks the scientifically interesting 896-912 Å portion of the spectrum, it was chosen to exclude any extremely bright >912 Å FUV from the large-aperture channel; even a single Å of this brighter FUV seen through the large aperture would overwhelm

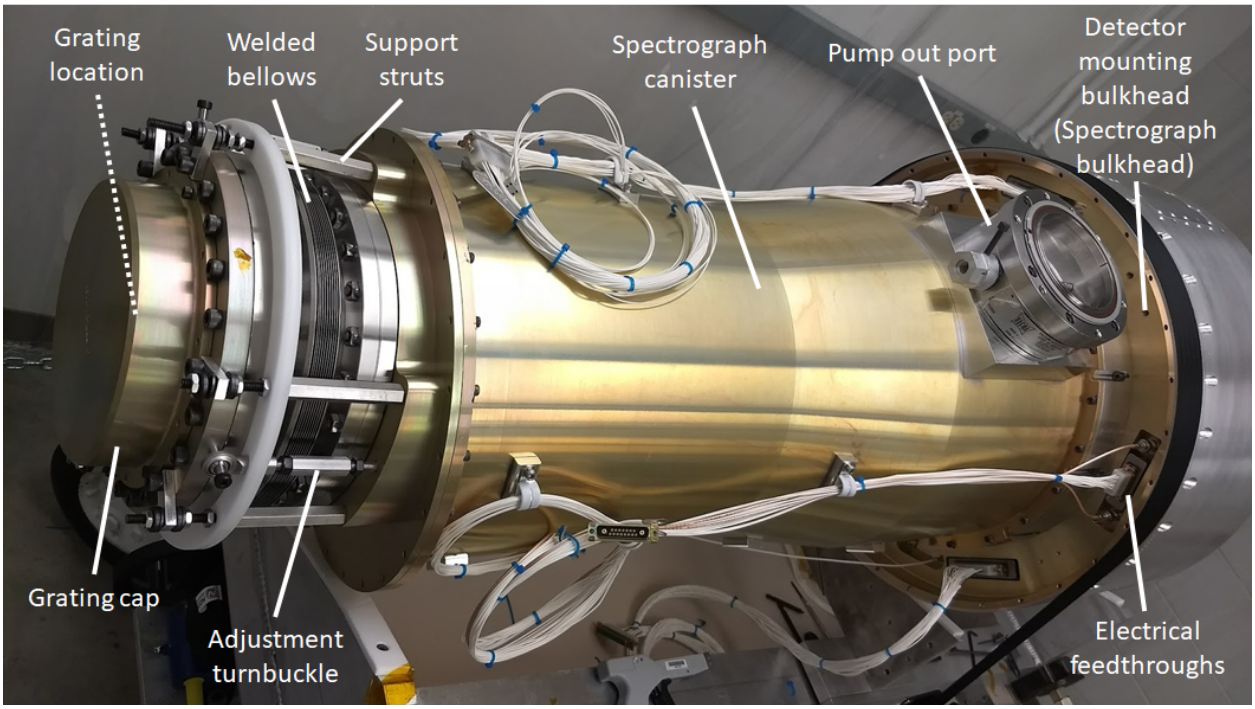

Figure 2.9: A view of the spectrograph canister and grating mount, taken early in the payload buildup. The grating is located inside the 'cap' on image left, and faces towards the right to diffract a spectrum onto the detector, located on the bulkhead on image right. The welded bellows and one of the three turnbuckles allowing grating tilting and adjustment are visible on image left. For context within the full payload, see Figure 2.2.

the detector global count rate limit. The intended short wavelength cutoff for both channels was 650 Å, as set by the asymmetric detector mask; however, upon grating installation a segment of the detector mounting plate was found to shadow the bottom 46 Å of the spectrum, resulting in the final low wavelength cutoff of 696 Å. This shadowing can be seen in the right side of Figure 3.6. Although unplanned, this obstructed bandpass still provided sufficient overlap between the EUV channel and EUVE [10] satellite observations extending up to 730 Å and did not impede the DEUCE science objectives.

2.2.4.3 Grating scatter and baffling

A holographic grating was chosen for DEUCE due to its improved scatter performance compared to a traditional ruled grating [67]. While holographic gratings are less efficient than ruled

gratings, the significant problems created by scattered light during previous observation attempts required minimization of ghosting and scattered light as a first priority. The DEUCE grating was specified to to exhibit $< 10^{-5}$ strength scatter 10 Å away from a monochromatic line and likely exceeded this parameter, as no detectable in-band scatter was ever observed in testing. To further reduce scatter, as well as leakage by out-of-bandpass FUV and 0th order rays, multiple layers of baffling were placed in the spectrograph canister between the grating and the detector.

2.2.5 Detector

2.2.5.1 Microchannel plate detectors

DEUCE utilized an imaging microchannel plate (MCP) detector. An MCP consists of three major components; a photocathode that converts incident photons into electrons, an array of millions of coated glass capillaries under an applied high voltage that serve to channel and greatly multiply the number of photoelectrons, and a two-dimensional readout anode that collects the multiplied photoelectrons and interprets them to form an image.

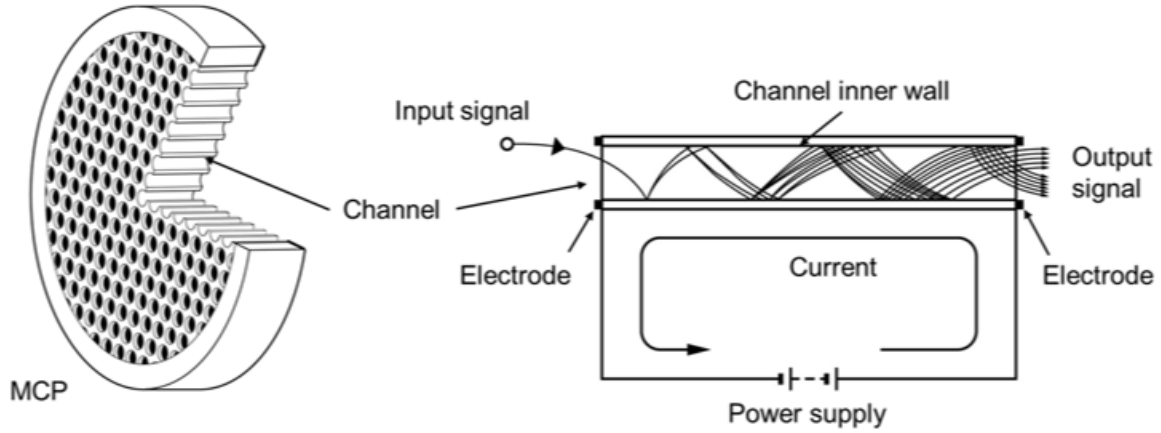

Figure 2.10: MCP diagram taken from Hamamatsu Photonics [51] showing a microchannel plate made of a multitude of individual channels or pores, as well as charge generation and multiplication in a single channel.

An image of a typical microchannel plate is shown in Figure 2.10. A single incident photon

impinges upon a particular MCP pore that is slightly angled with respect to the incident light and is converted into a photoelectron via the photocathode coating near the entrance to the pore. The high voltage difference across the plate then draws the photoelectron further into the pore, where it strikes the pore wall and generates an additional photoelectron. This process repeats until a large cloud of electrons exit the opposite side of the channel, having undergone high gain ($\sim 10^6$ for the two-plate DEUCE MCP). Modern MCPs often incorporate multiple MCP plates to increase gain and prevent ion feedback, in which trace gas in the pores is struck by the multiplying electrons and produces positive ions, which move back towards the photocathode and potentially produce new electrons in an exponentially increasing cascade. Some MCPs may also incorporate a QE enhancing ion repeller grid, which is a wire grid sitting above the MCP and charged at a negative voltage compared to the MCP plate, thus directing photoelectrons generated with velocities aiming away from the pores back down into the MCP. The DEUCE detector does not incorporate a QE grid due to its large size.

Once the multiplied electrons leave the rear end of the MCP pores, they proceed to a collection anode, which may take multiple forms, including single anodes, cross strip, and cross delay line anodes. In a cross delay line anode, as used in the DEUCE MCP, two metal strips are orthogonally wound in a serpentine fashion on top of a ceramic substrate as in Figure 2.11. When the cloud of electrons impinges on the anode, the charge travels down each strip to its ends, where it is delayed on one end and then read out by the MCP electronics. The position of the cloud in both x and y is calculated using the difference in arrival time of the charge at each anode end, along with knowledge of the anode length. Each individual photon is registered with a position, arrival time, and pulse height, which is essentially a measure of the total charge recorded and can be used for diagnostic and calibration purposes.

MCP advantages for UV astronomy include high QE compared to solid state detectors (e.g. CCDs), photon counting properties, low noise, high spatial and temporal resolution, solar blindness, lack of cryogenics, curvable focal planes, and large formats [106].

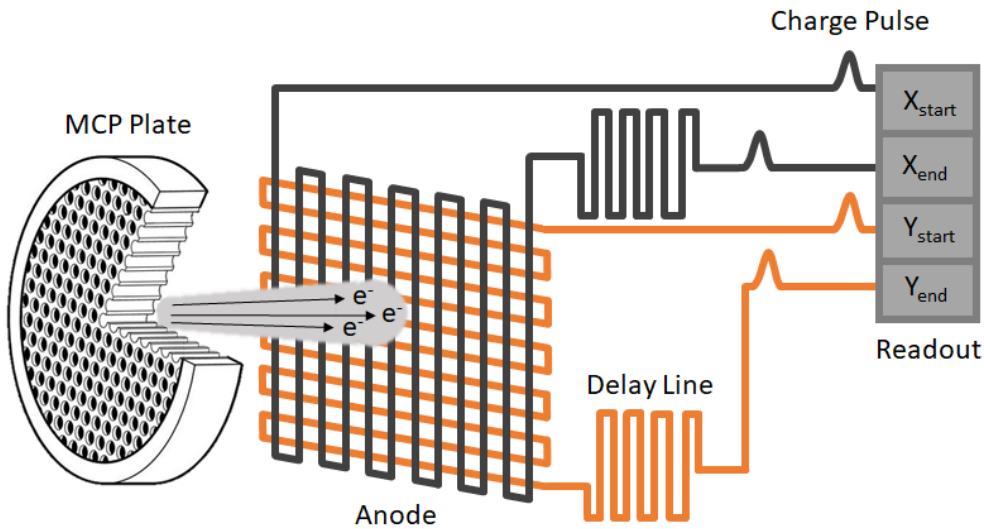

Figure 2.11: The MCP cross delay line anode. A multiplied charge cloud impinges upon crossed wires wound in a serpentine fashion. The charge moves through each wire towards its ends, with one direction of travel being delayed by a length of extra wire (the 'delay line') to ensure correct signal processing. The position of the charge cloud in both x and y is determined using the difference in arrival time of the charge cloud at each wire end.

2.2.6 The DEUCE detector

The 200 mm × 200 mm DEUCE detector is the largest single microchannel plate form factor currently being tested and operated in space. The MCP detector is a two-layer chevron-style stack with 20 μm pore size and 75% open area ratio, and was produced by Sensor Sciences. The total voltage across the detector was 2105 V, with a resolution of ∼100 μm in the X-direction and ∼ 150 μm in the Y-direction.

The front plate of the detector was coated in 1000 nm of Potassium Bromide (KBr). Cesium Iodide (CsI), was also considered as a photocathode, as it has a higher total efficiency summed across the 700-1150 Å bandpass. However, KBr outperforms CsI from 750-912 Å, giving more QE in the EUV at the expense of FUV sensitivity. As the EUV was both the main science goal of DEUCE and much fainter than the FUV, KBr was chosen as the flight photocathode.

The large size of the detector directly supported the technology development goals of the

DEUCE payload by testing a large-format MCP for future large-scale UV missions [29]. The detector performed as expected and survived over ten vibration tests and two launch campaigns. For a more detailed description of the detector and its performance, see [39].

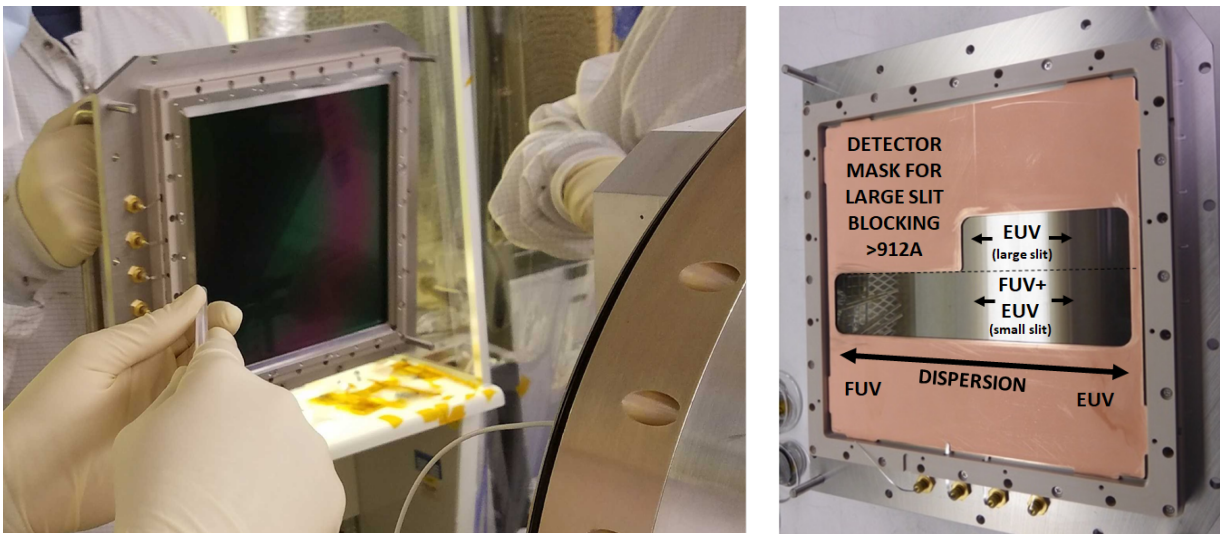

Figure 2.12: The MCP detector. Left: Installation of the detector into the payload. Right: The detector with the top MCP plate removed, exposing the detector mask resting above the bottom MCP plate. The EUV (large-aperture) and FUV/EUV (small-aperture) regions are labelled. For a better understanding of how the flight spectra fell relative to the mask, see the flight images (Figures 3.4-3.6)

2.2.7 Detector masking

The detector incorporated a physical L-shaped mask made of copper-coated FR4 glass epoxy laminate and designed to block the FUV portion of the spectrum transmitted by the large aperture. This mask was sandwiched in between the two detector MCP plates and functioned by preventing electrons generated by the top plate outside the masked region from reaching the bottom plate and anode. With the mask in place, the small-aperture channel registered a complete 696-1145 Å spectrum, while the large-aperture channel only registered the 696-895 Å portion, blocking higher wavelengths. Although no <912 Å light was observed by the small-aperture channel during flight (Figure 3.5), this was due to the combination of low aperture transmission and the inherent faintness

of the stellar spectrum below 912 Å, not obscuration by the detector mask. A labelled photograph of the mask outlining the positioning of the spectra on the detector can be seen in Figure 2.12b.

2.2.8 Detector electronics

The detector was paired with a cross delay line anode (Figure 2.13a) with coiled (X/Y) delay lines of (30.8/20.6 m) for a differential delay of approximately 144 ns in X and 96 ns in Y. This delay line fed into an adjacent amplifier, which boosted the signals before processing by a time-to-digital converter box, after which the signals traveled upstream to the payload electronics for processing and passing to the NASA payload section. The payload electronics section was designed in a modular fashion, with individual boxes containing components like the detector HV power supply or the telemetry interface (Figure 2.13b).

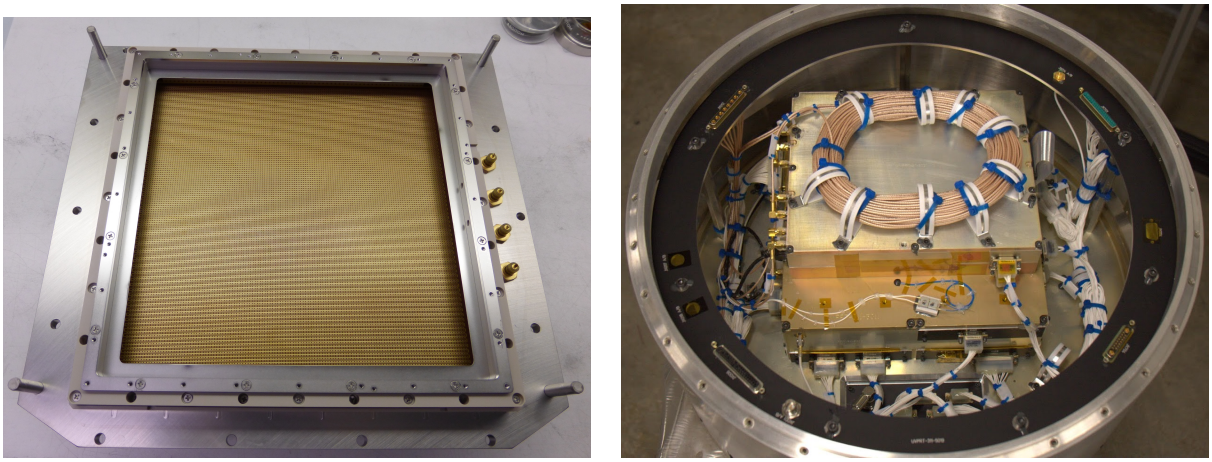

Figure 2.13: Left: The detector with microchannel plates removed, exposing the cross delay line anode. Right: The payload electronics section, showing its compact design, with the coiled detector delay lines prominent.

The detector's global count limit was ∼250k ct/s, limited by the length of the anode. Even within this global limit, however, intense local count rates could produce gain sag and detector non-linearity and had to be avoided. Neither Epsilon nor Beta CMa's spectrum posed a risk of violating these local limits when diffracted across the DEUCE bandpass. The MCP operating voltage of 2105 V was set by optimizing the pulse-height distribution to produce sufficiently high

gain while rejecting spurious counts. Maintaining this ideal pulse height required small adjustments over time and between flights. To protect against arcing, the detector was typically operated at pressures below 9×10^{-6} Torr.

2.3 Testing, support, and vacuum systems

The payload was tested in the UV vacuum facility at CU Boulder. This facility [125] includes the square tank and the longtank, along with a variety of other vacuum testing and support hardware.

2.3.1 The square tank

The square tank is a large, $1.8 \times 1.2 \times .57$ m vacuum tank typically used for calibration and testing of individual rocket components, like detectors and gratings. The tank is fed by a collimated beam generated by an off-axis parabola, which is in turn fed by a VM-502 McPherson UV monochromator. Light is generated by a hollow cathode arc lamp, using a number of different gases. The tank can attain pressures in the low 10^{-6} Torr range and pumps down within an hour. The tank houses a rotatable stage with a variety of attachments, including a goniometer and vertical/horizontal stages for positioning. A separate rotating arm houses a microchannel plate detector and pivots to allow both direct beam measurements and reflectivities to be measured. The square tank was used for all DEUCE grating testing.

2.3.2 The longtank

The longtank is a rocket-payload sized cylindrical vacuum chamber used for end-to-end testing of payloads prior to launch. The tank is a Newtonian telescope used in reverse to generate collimated UV light simulating a stellar UV source, with a hollow cathode lamp illuminating a pinhole at the focus of the telescope system. Focus is controlled by physically moving the light source and pinhole in 3D space. No monochromator is included in the system, so the light generated is polychromatic. The longtank was used for all DEUCE alignment testing, as well as calibration imaging. Due

to the height of the support rails for the payload inside the longtank, the DEUCE telescope was underfilled by the longtank collimated beam. As mentioned in section 2.2.1.1, the DEUCE payload produced a larger spot than expected (or of the size seen in flight) while imaging the longtank beam, potentially indicating insufficient collimation of the longtank.

2.3.3 Portable lamp

For quick verification of payload health and optical alignment, a portable UV lamp was built. This lamp consisted of a hollow cathode lamp, a pinhole, and a small rough pump that could be connected in series with a guillotine gate vale to a custom port drilled into the shutter door. While this lamp did not simulate collimated star light like the long tank, it was used to quickly determine if any shifts had occurred during shipments and vibration tests, as well as to ensure that the detector was functioning properly in the field and prior to launch.

2.3.4 GSE and GUI

Day to day interfacing with the DEUCE payload occurred through a purpose-built GSE unit that provided the payload with power and read out payload housekeeping (e.g. thermistor values, detector voltage) and detector data. Detector data collection occurred through a custom graphical user interface program developed by Nicholas Nell.

2.3.5 Vacuum systems

Payload vacuum was achieved through the use of a two-stage vacuum system. Rough pumping was provided by a 500 l/m Agilent Tri-Scroll 600 oil-less rough pump. High vacuum was achieved using a 550 l/s Agilent v551 Navigator turbopump, turned on after the payload reached rough vacuum ($< 1e^{-1}$ Torr). The rough pump was routed through the turbopump, meaning that when the turbopump was in operation, the rough pump served as its foreline pump. At high vacuum, the payload vacuum section could be isolated by closing a butterfly-style valve at the pump out port. Pumping between the telescope section and spectrograph canister was facilitated by two holes cut

into the spectrograph bulkhead and covered with charged mesh to prevent ions from reaching the detector. The initial DEUCE design used a guillotine gate valve and actuator motors to create a seal between the telescope and spectrograph sections, minimizing the detector's exposure to air or weaker vacuum while on the launch pad. This valve was to be opened by command in flight. This design added complexity, weight, and no small risk if the valve failed to open in flight; it was ultimately not used.

The DEUCE payload regularly achieved vacuum pressures in the low 10^{-6} Torr, with pump-down times to $< 1e^{-5}$ Torr (detector operation) of approximately 90 minutes. This was an unusually fast pumpdown time for a rocket payload, and was caused by the comparatively low surface area and bare metal interior of the payload, coupled with strong pumps and few constricted areas or choke points in the vacuum sections.

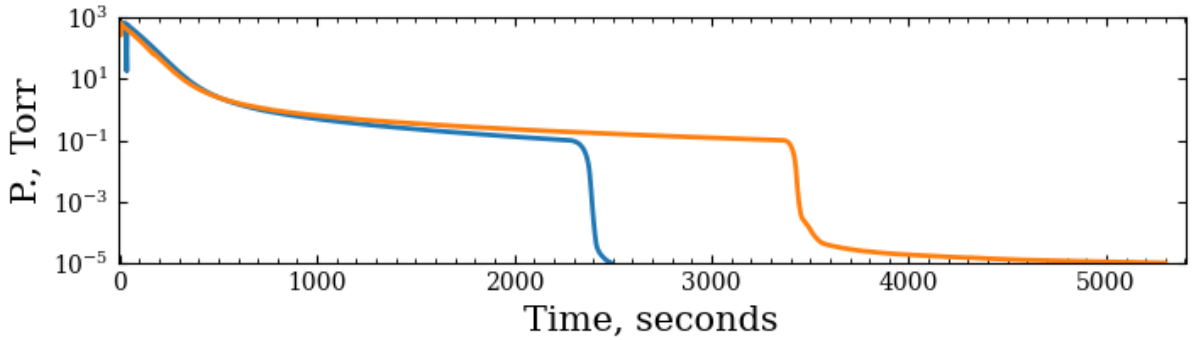

Figure 2.14: Typical pumpdown times for the payload, showing a pressure dip as the rough pump is turned on and a sharp drop-off once the turbomolecular pump is initiated. The blue curve shows a pumpdown where the payload had been kept under a nitrogen purge with few components open to the air. The orange curve shows a pumpdown where the telescope section was opened for a significant amount of time, albeit also with a nitrogen purge. An average pumpdown would take under 1.5 hrs from rough pump turn-on to $< 10^{-5}$ Torr.

2.4 Calibration

The DEUCE payload was calibrated at a component level in a series of measurements taken between 2017 and 2019. These measurements were treated as relative calibrations and scaled to EUVE [10] and IUE [88] satellite observations (Section 2.4.5).

2.4.1 Telescope effective area

The telescope effective area had already been determined [123] during its use in earlier sounding rocket payloads. This previous calibration was performed by illuminating the telescope with monochromatic pencil beams of various wavelengths and measuring the intensity of the incident and reflected beams with an MCP. The telescope reflectivity was sampled at multiple positions along three annuli of different radii on the primary mirrors, keeping both the spot position on the detector and the angle between beam and detector face fixed. This reflectivity was then multiplied by the measured geometric collecting area of the primary mirror (678.5 cm^2) to obtain an effective area. This original measurement's error averaged 2.5% and was a propagation of $\sqrt{N}$ errors, where N was the number of counts registered by the MCP.

As the telescope is made of solid aluminum with robust Ni and SiC overcoats, was safely stored between launches, and was cleaned prior to use in the DEUCE mission, its effective area was assumed to have remained unchanged with respect to previous launches. Since the previous measurements only extended up to 1048 Å, the slope of the graph and associated error were linearly extrapolated to the 1150 Å edge of the DEUCE bandpass. A linear extrapolation was chosen for simplicity and because the telescope reflectivity is not expected to exhibit small-scale structure across the instrument bandpass. The telescope effective area is shown in Figure 2.15.

2.4.2 Entrance aperture transmission

The entrance aperture transmission for the EUV channel was assumed to be 100%, as the flight spot fully fit into the large aperture. The aperture transmission for the FUV channel proved difficult to obtain due to the complex shape of the telescope spot coupled with the motion of the spot across the aperture in flight due to pointing jitter (Figure 2.4). Laboratory testing of aperture transmission as a function of spot placement, coupled with analysis of the average spot position in flight, led to a small-aperture transmission estimate of approximately 1-5% during the 2018 flight. While an average of this transmission (3.5%) is used to generate the final payload A_{eff} plot in

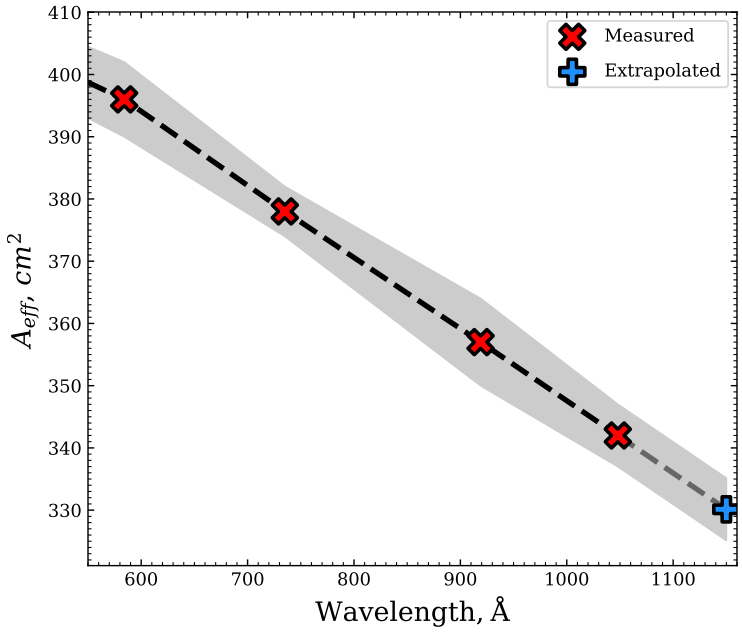

Figure 2.15: The telescope effective area as measured by [123]. The 1048-1150 Å region was linearly extrapolated from the slope and error at 1048Å. Error is represented by the grey fill and is $\sqrt{N}$ in nature. Both the effective area values and the error are linearly interpolated between data points.

Figure 2.18, this value was never treated as definitive; instead, the FUV channel was scaled to IUE satellite observations (Section 2.4.5).

2.4.3 Grating efficiency

The grating efficiency was measured in May 2019, after the second DEUCE flight.

In this measurement, the flight-mounted grating was attached to a translation/rotation stage in the square tank and placed in its flight orientation with respect to an incident monochromatic pencil beam produced by a hollow-cathode discharge lamp fed by neon or hydrogen/argon gases. Reflected measurements were taken by measuring the grating's 1st order diffracted intensity by means of a MCP detector. The incident beam strength was measured by translating the grating out of the beam path and directly sampling the beam with the same MCP. This basic process was repeated for as many wavelengths as possible, covering the DEUCE bandpass.

On each run, care was taken to fix the detector face at the same angle to the incident beam

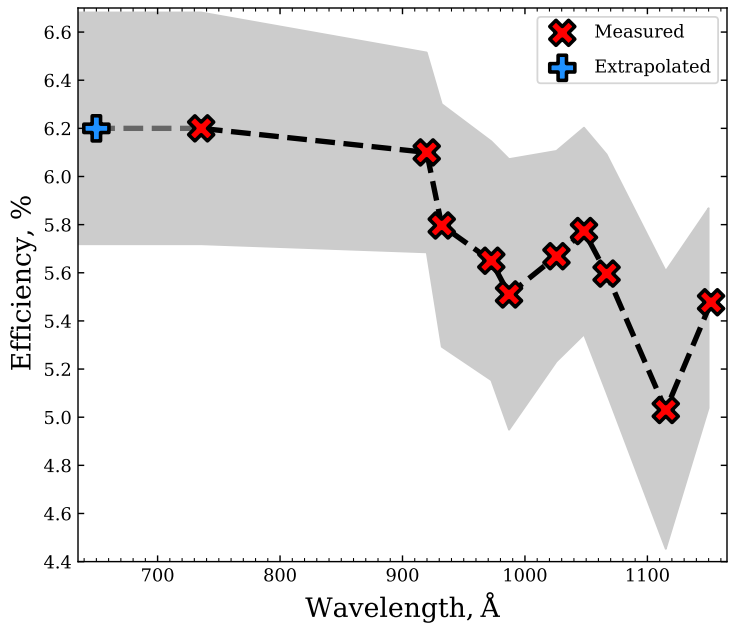

Figure 2.16: The grating absolute efficiency including the reflectivity of the SiC coating, as measured in May 2019. Error is represented by the grey fill and is a propagation of $\sqrt{N}$ errors. Both the efficiency values and the error are linearly interpolated between data points.

and illuminate the same region on the detector to ensure uniformity between measurements. Dark exposures were taken surrounding every measurement, and an incident measurement was repeated at the start and end of each wavelength run to account for any light source variability. Error was calculated by determining and propagating the $\sqrt{N}$ errors of each measurement, where N is the number of counts detected. The general grating efficiency was calculated by linearly extrapolating the data between the measured datapoints across the DEUCE bandpass. For the 696-737 Å region of DEUCE bandpass where the hollow cathode lamp could not produce sufficiently strong beams, the grating efficiency was linearly extrapolated by assuming a constant efficiency and error from 737 Å down to the 696 Å cutoff. Linear interpolations were utilized because modelling of the grating predicts a smooth variation in grating efficiency across the DEUCE bandpass. While the origin of the small-scale changes in efficiency measured above 900 Å is not understood, given the model-data discrepancy there was no basis for assuming any particular shape to the grating efficiency curve. A simple linear interpolation was therefore the fit requiring the fewest assumptions. The grating

absolute efficiency is shown in Figure 2.16.

2.4.4 Detector quantum efficiency

The MCP detector quantum efficiency was measured both in early 2017, prior to the first flight, and in April 2019, after the second flight. The measurement was performed at a Sensor Sciences lab utilizing a NIST-calibrated photodiode.

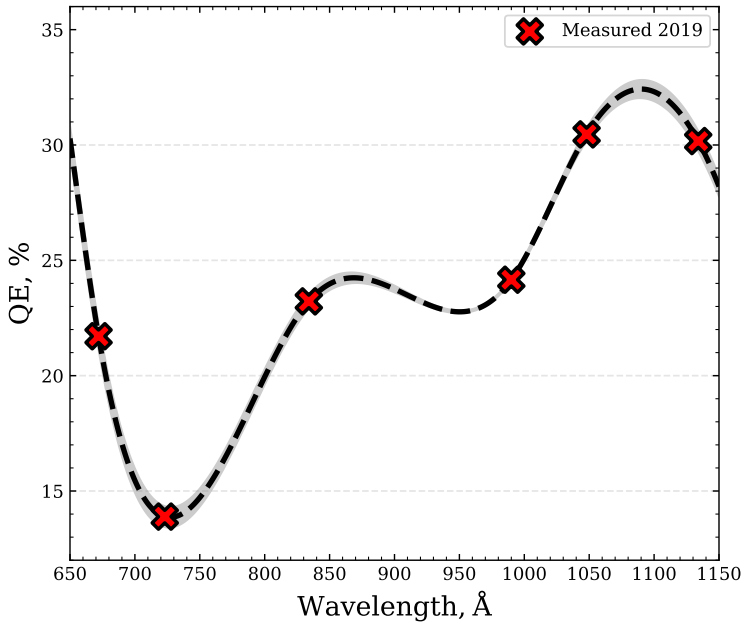

Figure 2.17: The detector quantum efficiency, as measured by Sensor Sciences on April 2019. Error is represented by the grey fill and is a propagation of $\sqrt{N}$ errors, where N is the number of counts detected in each measurement. Both the QE values and the error are interpolated between data points using a spline fit which better describes the typical behavior of KBr photocathodes compared to a linear fit.

A monochromatic pencil-beam of a single wavelength was shone directly onto the flight detector, generating a MCP count rate. A NIST-calibrated photodiode was then immediately rotated into position so that the same incident beam fit completely onto its active area, tying the previously measured MCP count rate to a calibrated flux at a single wavelength. This process was repeated for as many wavelengths as possible over the DEUCE bandpass. Due to the dynamic range issues inherent between the MCP and the less sensitive diode, a mesh with a known geometric transmis-

sion was placed in front of the detector (but not the diode) for some of the line measurements. This known attenuation was then removed from the data post-testing.

The general detector efficiency was calculated by interpolating the data between the measured data points according to a spline fit. A spline fit was chosen over a simple linear fit because of previous knowledge of the QE behavior of similar KBr-coated MCP detectors measured at a finer wavelength scale than the DEUCE MCP. A spline interpolation ultimately provided a better fit to these data, including the <650 Å rise, the relative flatness from 850-1000 Å, and the rise between 1050 and 1140 Å. The stated uncertainties on the detector efficiency were purely statistical, and do not reflect the many systematic uncertainties potentially present in the setup and measurement. Between the 2017 and 2019 calibrations, some QE degradation was observed outside of the DEUCE bandpass above 1150 Å. Since only the 2018 launch produced science results, this degradation did not affect the instrument science calibration, which utilized the 2019 test results for the detector QE. The detector quantum efficiency is shown in Figure 2.17.

2.4.5 Final instrument $\mathbf{A}_{eff}$ and scaling

The calculated effective area (A_{eff}) of the DEUCE instrument as a whole is presented in Figure 2.18. This A_{eff} is defined as the "net" effective area, and is a combination of the full effective area (found by multiplying the measured telescope A_{eff}, grating efficiency, and detector QE) and aperture transmission, which was taken as 100% for the large-aperture channel and 3.5% for the small-aperture channel. The presented error is similarly a propagation of the individual errors of each component.

It is important to note that while care was taken in the overall calibration and associated error calculation, the flux-calibrated spectrum of ϵ CMa produced by the instrument when utilizing the measured A_{eff} did not fully match existing EUVE and IUE observations of the star from 700-730 Å and at 1150 Å. As the satellite calibration procedures were deemed to be more thorough, the DEUCE calibration was treated as a relative calibration rather than an absolute calibration, and the EUV and FUV channels were scaled to match the EUVE and IUE measurements where

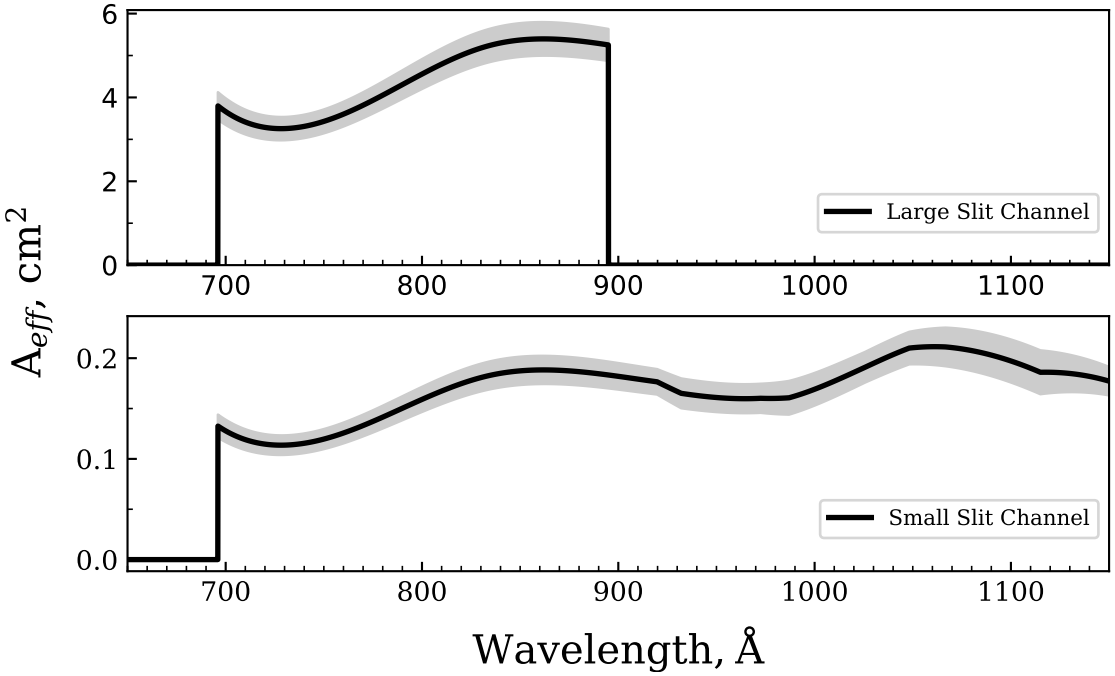

Figure 2.18: The measured net effective area of the DEUCE instrument for both channels. **Top:** The measured net effective area for the large-aperture channel, with 100% aperture transmission from 696-895 Å. Above 895 Å, the detector mask cuts off the spectrum to prevent extremely bright flux from reaching the detector. **Bottom:** The measured net effective area for the small-aperture channel, shown here with an assumed 3.5% aperture transmission throughout. Small aperture transmission was only roughly known and varied between 1-5%. In flight, no flux was seen in the small-aperture channel below 912 Å due to the combination of small aperture and weaker stellar flux in this region. In both channels, the payload bulkhead cuts off the spectrum below 696 Å.

the bandpasses overlapped. This was expected for the small-aperture FUV channel, where the unknown aperture transmission naturally resulted in a relative calibration, but it is unclear what caused the discrepancy in the large-aperture EUV channel, for which the EUVE observations fall slightly outside the 1σ error bars of the ground calibration.

The final scalings required multiplying the DEUCE fluxes by 1.33 in the EUV and by 6.82 in the more uncertain FUV. The EUV scaling was calculated by minimizing the χ^2 difference between the DEUCE and EUVE spectra of ϵ CMa in the 700-730 Å overlap region, accounting for error and allowing scaling to vary as a free parameter. The FUV scaling was performed by finding the scaling factor that provided the smoothest continuation between the DEUCE spectrum from 1100-1143 Å

and the IUE spectrum beginning at 1150 Å. Both scaling processes are fully described in Section 3.3.1. The final fluxes scaled by these factors were those used in scientific analysis of the data.

2.4.6 Wavelength calibration

To wavelength calibrate the payload, deep (10-30 min) spectra of neon, hydrogen-argon, and room air were taken on the high-resolution, small-aperture channel using the long tank. Multiple exposures taken with each gas over the course of the mission were linearly shifted to match images taken immediately before and after launch in 2018, after which they were co-added, stacked, and vertically summed to produce master spectra for each gas, which were combined into a final calibration spectrum (Figure 2.19). Major lines were identified manually utilizing the NIST spectral line database [59], and their centers were determined via Gaussian distribution fitting. A fifth degree polynomial was fit to the resultant (wavelength, pixel) pairs and used to generate a dispersion relation for the entire spectrum. Based on this first iteration, further lines were manually identified and added to the solution, while any obvious outliers with high dispersion were excluded. This process was repeated until no more new lines could be identified with confidence. The final solution was corrected for both the Earth's rotation and orbital velocity using the PyAstronomy [19] helcorr routine. The dispersion between best-fit and true wavelength on the final wavelength calibration was less than .2 Å for all identified lines. However, the DEUCE data required a 2 Å negative shift to match EUVE data of Epsilon CMa from the MAST archive. As such, the final absolute calibration is considered to be accurate to within 4 Å. This level of wavelength calibration was adequate for identifying the broad EUV output of Epsilon CMa.

Calibration spectra were typically taken in sequence, with some flushing and vacuum cycling of the lamp with GN2 in between calibration runs. Nonetheless, it was difficult to completely purge the gas inlet hose of the lamp between runs; thus, spectra often had residual and even quite strong lines of other gases– a 1025.7 Å hydrogen-argon line might be present in a neon spectrum taken immediately afterwards. No in-flight wavelength calibration occurred, but laboratory calibrations were taken both before and after each flight to account for any shifting during launch, which was

found to be minimal on the 2017 flight and approximately 1 Å on the 2018 flight.

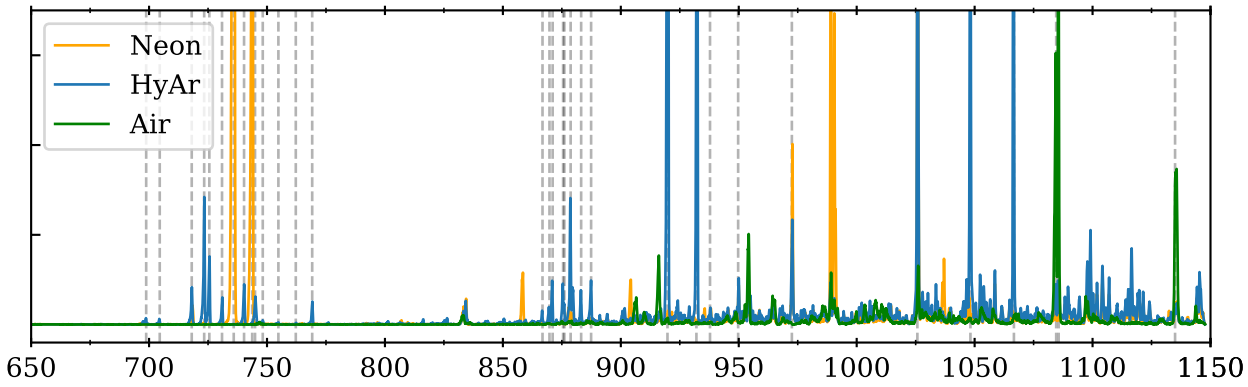

Figure 2.19: The identified hydrogen-argon, neon, and air lines used for wavelength calibration. Identified lines are shown by vertical dashed lines. The strongest, most readily identified lines that formed the foundation of the calibration are H I (949.7 Å, 972.5 Å, 1025.7 Å), Ar I (1048.2 Å, 1066.7 Å), Ar II (919.8 Å, 932.0 Å), and Ne I (735.9 Å, 743.7 Å).

2.4.7 Spectral resolution determination

The DEUCE spectral resolution was determined by measuring the width of unblended lines present in a variety of laboratory calibration spectra of different source gases produced by both the high and low-resolution channels. Lines used to determine resolution were visually inspected to ensure no obvious line blending and then fit with a Gaussian distribution to determine their line width at FWHM. An average line width was then determined for each channel. The low-resolution channel utilized Neon lines below 900 Å at 717, 735, and 743 Å, while the high-resolution channel utilized lines above 900 Å: 919, 932, 1025, 1048, and 1067 Å. The final resolving powers were determined to be approximately 180 in the low-resolution channel and between 1500 and 2000 for the high-resolution channel.

2.5 Major operations and phases

Select major stages and events of the rocket life cycle are described in the following sections. A full list of major events for the payload and their dates is presented in Appendix A.

2.5.1 Build up

The DEUCE payload was built up between May and August of 2017. The first phase of payload construction consisted of the logistical effort of identifying, ordering, and assembling all rocket components. Parts were identified from a CAD rendering of the payload, including supporting components such as screws, etc. All skins and bulkheads, as well as the spectrograph canister and shutter door, were provided by NSROC machine shops, while local machinists were contracted for all other major components. Required electrical components and their specifications were identified from an electrical blueprint book, "Patchy", created by Nicholas Nell, and ordered from a variety of online suppliers.

The logistical effort of build up consisted of fluidly keeping track of which components were required, ordered, and obtained, and storing them to facilitate as efficient a payload assembly as possible. Regular meetings ensured no aspects of the payload development were neglected. All electrical and mechanical parts were logged in an online tracking system showing what parts were required, whether they had been ordered, and if they had been received. Newly arrived parts were cataloged, checked for defects/accuracy, and sent for anodizing or iriditing if required. Interlocking parts were immediately fit checked; on multiple occasions, parts were mis-machined and had to be immediately sent back for minor or major re-machining. Accepted metal parts were cleaned thoroughly either by hand or in ultrasonic cleaners with sequential simple green, water, and isopropanol baths, had helicoils installed, and were stored in labeled bagging in a clean room. Black oxide screws were ultrasonically cleaned with sequential mineral spirits, acetone, and isopropanol baths and similarly labeled and stored. Electrical components were cleaned and stored in clean, labeled containers. All minor hardware or electrical components had a plurality of spares available;

if a single screw was needed for an application, typically at least five were cleaned and stored.

As skins and bulkheads arrived, they were assembled as soon as possible, with the initial goal of leak checking, verifying fits, and pumping down. This initial pump down of the payload vacuum cavity was an important milestone, as all skins and bulkhead had long lead times that could cause major delays if re-machining was needed. As major components like the grating and detector arrived, they were individually tested, mounted, and integrated into the payload. The telescope was installed early on, as it did not need to be stored at vacuum, while the detector was installed as the last component immediately prior to fully assembled payload pump down in order to protect its coatings from unnecessary exposure to water vapor.

Figure 2.20: Two photos (out of many) of the payload build up. Left: Newly arrived parts are inspected after having been iridited. Right: Adjustments to the spectrograph bulkhead are calculated after a machining error resulted in an O-ring groove design not functioning in the assembled payload.

The payload electronics were initially tested while dirty to enable easier changes and replacements. Once the electronics section passed testing, all boards, cables, and electronics boxes were cleaned and reassembled, while the cables' heads were potted with epoxy to protect them from launch vibrations and high-vacuum shorting. A significant amount of effort was expended identifying how to best lay cables both in the electronics section and in the payload itself, for which zero-outgassing cable clamps/zip ties and epoxied metal mounting tabs were utilized. Once the

payload optics and electronics were again tested and verified in situ, all structural and adjustment screws and cable clamps were installed and staked into place. Staking had to be carefully scheduled, as the staking epoxy took 5-7 days to fully outgas and cure, during which the payload was kept under a clean GN2 purge with a focus on the region near the detector face. Once the payload was fully assembled, aligned, and staked, it was tested one final time in the long tank and then moved to a custom wooden shipping container for transport to integration or launch.

2.5.2 Grating bonding and installation

The grating was bonded into its flight mount in July of 2017 at CU Boulder. The bonding took place in a custom bonding jig that secured the grating in a precise (X-Y-Z) location with respect to its mount through the use of height adjustment screws (Z) and positioning posts (X-Y). All pieces of the jig that directly touched the grating were either covered with Kapton or nylon-tipped. The bonding jig, along with the grating mount, are shown in Figure 2.21.

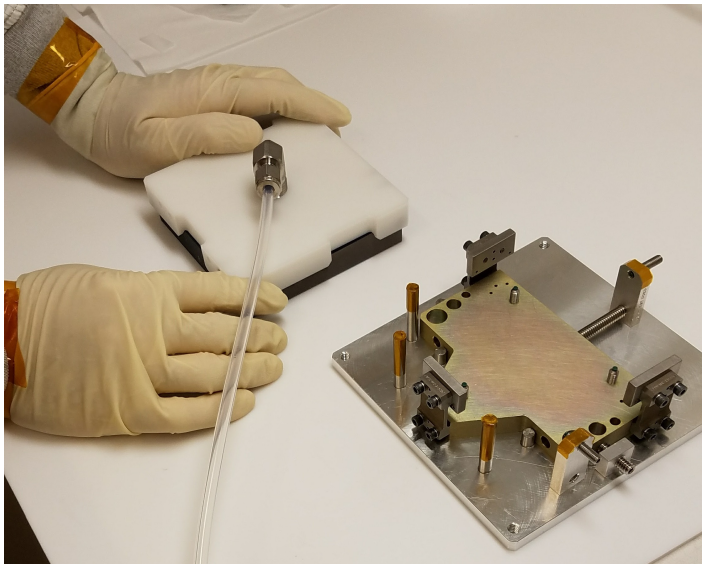

Figure 2.21: The grating and the jig immediately prior to bonding. Visible are the three cylindrical, vertical posts and two 'tombstone' adjustment screw mounts used to hold the grating precisely in the X-Y plane, as well as 2 (1 obscured) vertical screws controlling the Z height. Also visible are the 3 rectangular pads to which the grating was ultimately bonded. All metal components near or touching the grating glass were either nylon-tipped or covered in Kapton tape.

The grating mount itself consisted of a weight-relieved base which secured three vertical titanium struts. These struts in turn each held an Invar mounting pad to which the grating was bonded. Although I ultimately questioned their necessity, pins were pressed into both the base and the Invar pads so as to constrain their orientation and remove any slop in the mount. The weight-relieved base had holes drilled into it through which three small adjustment screws of the bonding jig could pass and set the grating height during the bonding process.

Bonding was practiced multiple times prior to the final run, both with simple plastic test fixtures over which a single bond line could be made, and with a mass model of the grating in the full grating jig. The final bonding procedure was as follows:

- The grating bonding jig and grating mount were cleaned. Kapton was placed on all metal surfaces that would be in contact or close proximity with the grating glass during bonding.
- The Invar pads that adhere to one side of the bond were cleaned and prepared for bonding with an intensive process first created by Ann Shipley for the FUSE mission [85].
- The grating mount was fully assembled, torqued, and placed in the bonding jig. The height adjustment screws were adjusted to hold the grating at the desired height above the jig.
- Thin Teflon sheets were draped over the Invar pads and all exposed metal surfaces to ensure no metal-glass contact. The grating was lowered into the mount, resting on the height adjustment screws, and the Teflon sheets were removed.
- The grating orientation was verified by shining a purple laser (which had diffraction solutions for the grating) onto its surface and ensuring that the diffracted orders fell in the correct axis with respect to the mount (Figure 2.22a).
- A Delrin grating cover was placed over the grating and clamped in place with Delrin clamps. It had a threaded top through which a clean nitrogen purge could be created directly over the grating, protecting it from the fumes of the bonding epoxy as it cured.

- The grating was gently secured against the posts that positioned it horizontally using nylon-tipped screws. Three small strips of Teflon shim were placed between the grating glass and Invar pads on the left, right, and middle of each pad to ensure an even bond line (Figure 2.22b). The required thickness of the shims was determined by trial and error, and required a wide variety of shim thicknesses to stack and test. The final grating positioned occurred when all 9 Teflon strips had a simultaneous snug fit, indicating an equally distant and even bond line across all 3 pads. The final bond thickness required was .025 mm, produced by one shim of that thickness.

- The grating purge was turned on in preparation for bonding. Hysol damming epoxy was mixed, agitated under vacuum to remove air pockets, and applied in a perimeter line around the bottom and sides of each Invar pad. The purpose of this epoxy was to create a dam that contained the structural bonding epoxy (applied later) and prevent it from simply oozing out around the open edges of the Invar pad. The outermost (left and right) Teflon shims of each pad helped prevent the Hysol from being wicked into the grating-pad gap at the pad edges. The Hysol damming epoxy was allowed to cure overnight, with the grating under direct, active purge via its cover.

- The next day, the left and right Teflon shims were removed from each bond pad, leaving two cavities between the grating and the pad, divided by the center Teflon strip and bordered by the Hysol epoxy on the outside edges (Figure 2.23a). 2216 A/B epoxy was mixed, agitated/degassed, and inserted with a syringe through preexisting holes in the Invar pad, filling the left and right cavities in each bond face. Epoxy was inserted until it had just barely begun to exit the enclosure through the gap at the top of the bond pad. (Figure 2.23b). Once the epoxy had largely set but not solidified completely, the central Teflon strip was removed. The epoxy was then allowed to cure for seven days, after which the bonding jig was removed.

The end result of the process was a grating held in its mount by six different bond faces in

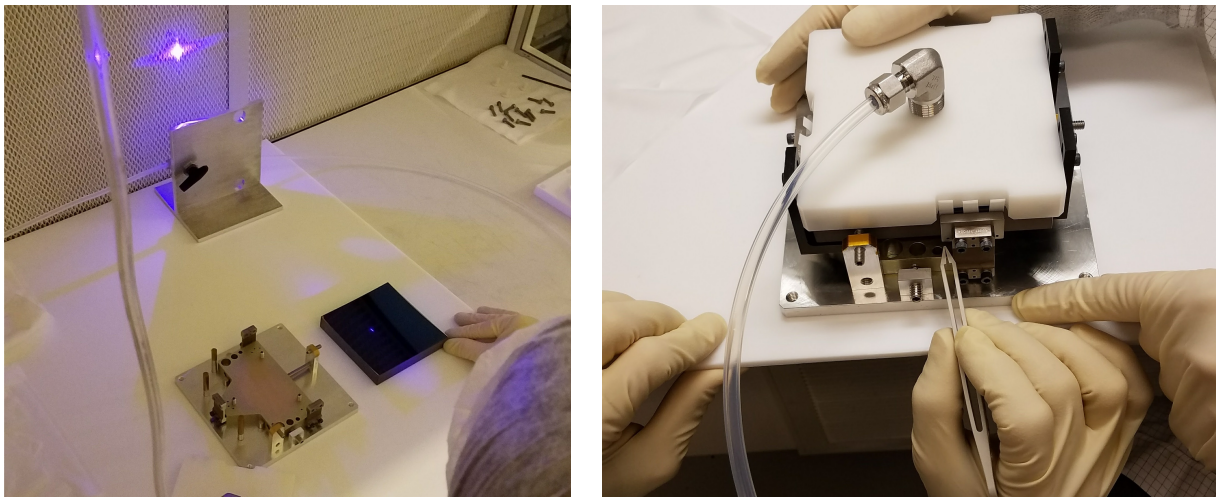

Figure 2.22: Left: A purple laser being shown on the grating to determine groove orientation prior to bonding. Right: Adjustment of three of the nine Teflon spacing shims used to ensure an even bond line for the grating bonding.

three pairs. These bond faces and the grating cover were the only materials physically contacting the grating for the remainder of its use in the payload. The mounted grating was finally placed inside the "catcher's mitt" flight housing (Figure 2.8) and integrated into the spectrograph section.

2.5.3 Detector acquisition, installation and removal

In April 2016, the detector was acquired and transported from Sensor Sciences in a transport container that allowed it to be placed under vacuum and backfilled with clean GN2 (Figure 2.24a). The detector was installed into the payload in late July of 2017. Installation consisted of backfilling the transport box up to atmospheric pressure, removing the detector, installing it into the payload, and pumping down the payload as soon as possible. The detector had four metal guide posts, one on each corner, that fit into holes on the spectrograph bulkhead detector mount. During installation, it was discovered that the tolerances on these holes were very tight, and the guide posts jammed, leaving the detector only partially installed, with a gap between its metal face and the mount O-ring (Figure 2.24b). The detector was gently tapped into position until its mounting screws could engage the threads of the bulkhead mount, upon which they were sequentially tightened to draw

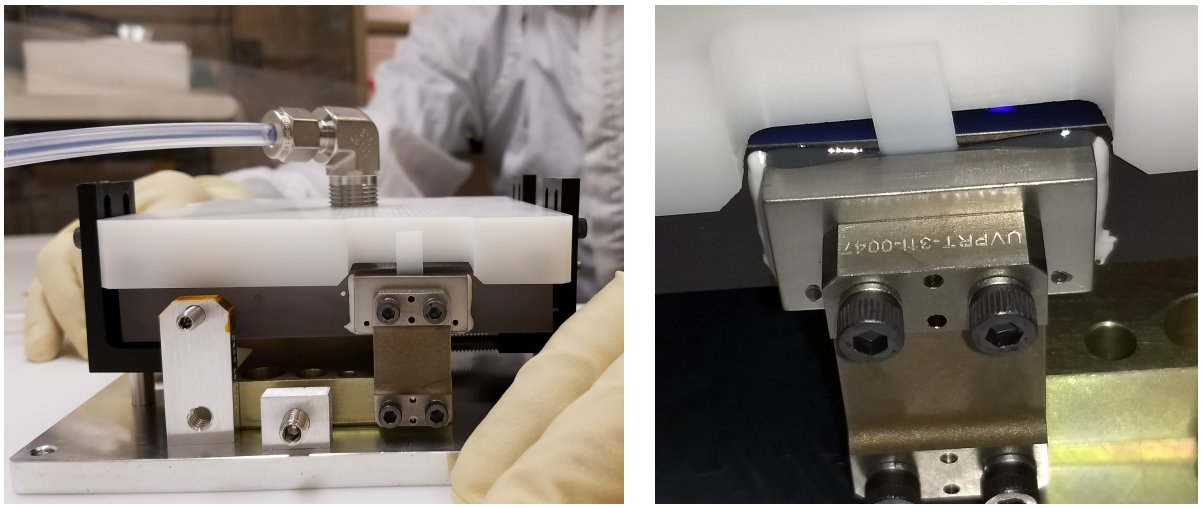

Figure 2.23: Left: The grating with damming epoxy in place and cured, and the remaining central divider strip still in place, ready for 2216 structural epoxy injection. Right: A grating flexure after 2216 injection, prior to removal of the central Teflon strip.

the detector fully onto the mount.

The detector was removed from its mount in February of 2019, in preparation for post-flight QE testing at Sensor Sciences. Given the tight tolerances of the guide posts, a custom removal jig was designed (Figure 2.25a). Two metal bars were machined to mount to the handle screw holes on the detector back, while a slanted base was created to allow the detector to be purged during removal and to counteract the slant of the detector spectrograph mount so that even pressure could be applied perpendicular to the axis of the mounting posts. The detector and its spectrograph mount were removed from the payload and immediately mounted onto the slanted baseplate, which was then clamped to a optic bench and purged with GN2. All of the screws holding the detector to the spectrograph mount were removed, and the metal bars were attached to the detector back in the locations normally used to attach handles. The screws at each end of the bars were tightened in unison until the detector lifted free of the spectrograph mount (Figure 2.25b), upon which it was immediately transferred to its transport container, pumped down, and backfilled to partial pressure with GN2.

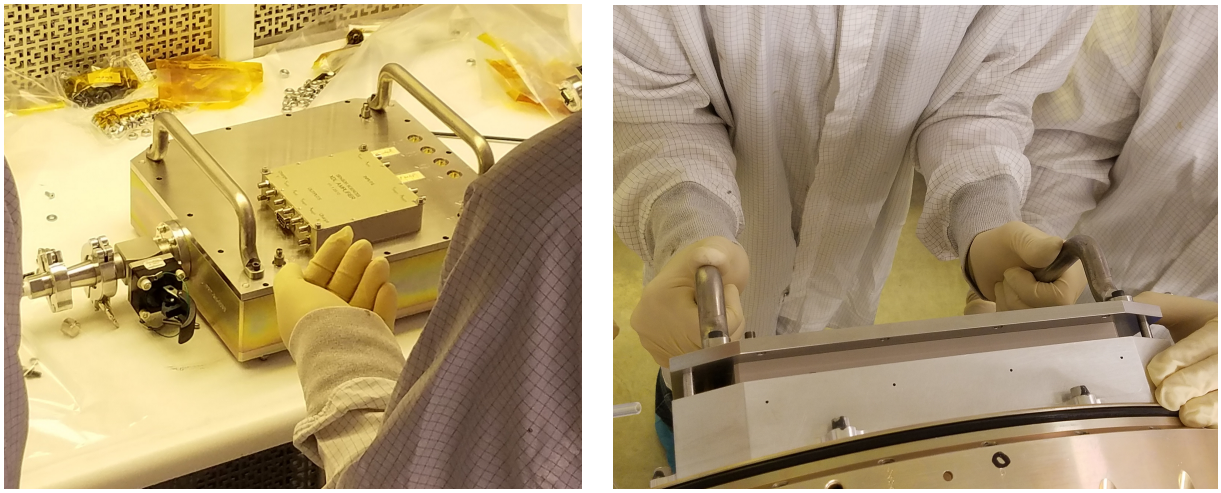

Figure 2.24: Left: The detector transport case, which allowed for pump down and GN2 partial pressure storage of the detector during transit. Right: The detector being installed (immediately after Figure 2.12a) and jamming due to the tight tolerancing of the four guide posts.

2.5.4 End-to-end calibration attempts and failure

An end-to-end calibration of the payload was attempted between February and July 2018, between the two launches. A VM-234/302 model monochromator was acquired and attached to an off-axis parabola (OAP) and a hollow cathode lamp. Careful positioning and alignment of the OAP downstream of the diverging light produced by the monochromator exit slit generated roughly collimated light, which was fed directly into the payload and measured on the payload MCP detector. A NIST-calibrated photodiode was then positioned in such a way that it could be inserted in and out of the beampath, which it completely sampled.

The concept behind the measurement was very similar to the detector calibration described in Section 2.4.4. The monochromator would be used to generate a series of collimated beams at a variety of different wavelengths across the DEUCE bandpass and direct them into the payload. The DEUCE detector would be used to make a measurement of the beam after interaction with all payload elements (telescope, entrance aperture, grating, detector). The same beam would then be immediately sampled by the chamber photodiode, which would tie the count rate on the payload detector to a calibrated flux. In this way, an end-to-end absolute flux calibration of the payload

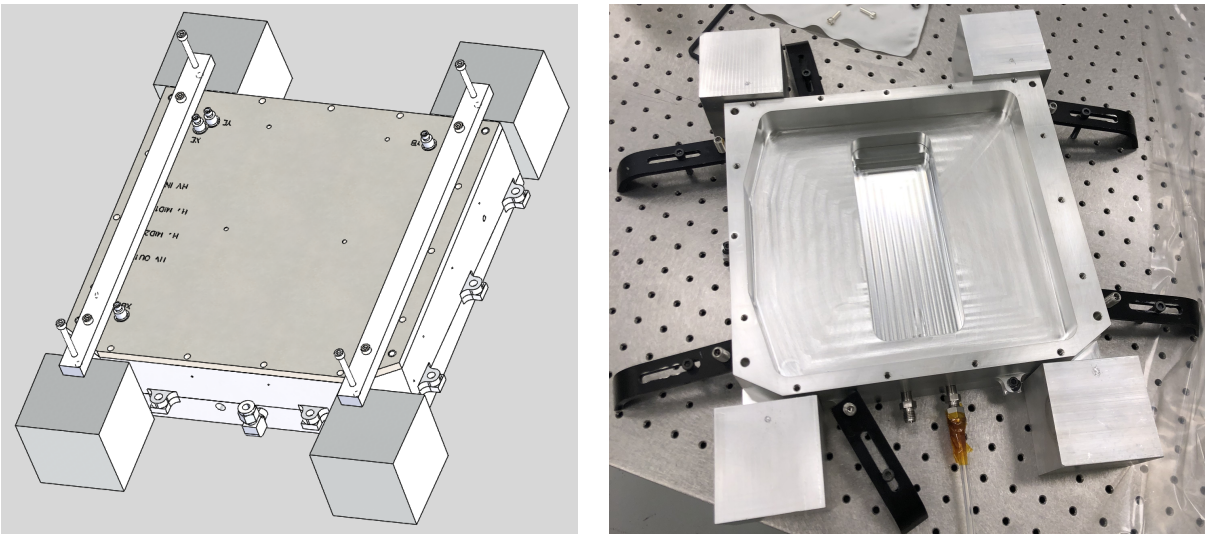

Figure 2.25: Left: The detector removal jig imaged in CAD, showing the removal bars attached to the detector handle screw holes. All screws holding the detector to its housing were removed and the four screws on blocks were tightened in unison against the blocks to raise the handles and part the detector from its mounting plate. Right: The detector mount in the lab post detector removal. Imprints of the raising screws can be seen in the four spacer blocks.

would be obtained on the ground prior to launch.

This effort ultimately failed, largely due to difficulty achieving sufficient collimation while maintaining high enough throughput for detection by the NIST photodiode. Off-axis-parabolas are in theory capable of perfectly collimating a point source at their focus. However, any real beam from a real source has physical size and results in imperfect collimation. There was thus an inverse relationship between the size of the exit slit on the monochromator (and thus the source image for the OAP) and the collimation of the beam produced by the OAP. To obtain a beam that retained tight collimation over the optical path of the payload, the slit needed to be as small as possible. Collimation was attempted with both the OAP and a set of double pinholes; in each case, tight collimation required extremely small slits or pinholes and therefore produced an extremely faint image. While this was not necessarily problematic for the highly sensitive photon counting DEUCE MCP, the NIST photodiode required significant flux and struggled to measure the faint levels output by the dim collimated beams. If the slit size was increased to increase throughput,

the beam could overfill the photodiode or drastically lose its shape while transiting the payload towards the detector. In the end, no suitable combination of collimation and brightness was found that allowed for an end to end measurement outside of the long tank, and the schedule did not permit a second attempt at end to end calibration inside the long tank.

2.5.5 Integration

The DEUCE payload integrated at Wallops Flight Facility in September 2017 and in White Sands Missile Range in November 2018 in preparation for flights in October 2017 and December 2018. Integration consisted of connecting the NSROC and CU sections of the payload and ensuring they communicated as intended, vibration tests (Figure 2.26), two-axis spin testing and moment of inertia determination, bend testing, and weighing. A timeline of the events constituting integration can be found in Appendix A.

Figure 2.26: The payload nose-cone undergoing vibration testing at Wallops Flight Facility in September 2017

2.5.6 Pre-launch preparations

Once the payload was shipped to WSMR, a variety of procedures paved the way towards launch night. The payload first re-integrated with the NSROC sections and tested communications. The flight star tracker was installed and a 'digital shim' was programmed into the software to account for the difference in alignment between the star tracker and payload telescope. The flight parachute and separation springs were installed in the nosecone. A 'horizontal' launch sequence was practiced, simulating all of the events of launch, including pulling umbilical cords to trigger moving to internal power and timed events, accelerometer and gas jet checks, control over radio, and experiment functionality and data passing. Since the horizontal test required verification of shutter door performance as well as detector performance, the test occurred twice; once at vacuum with a simulated shutter door opening, and once at air with the actual shutter door opening and a simulated detector turn on. After the horizontal, pyrotechnical cutters that trigger payload separation in flight were installed, and the payload was moved to the launch rail and rigged to the umbilical power and data cords present there. A vertical test, similar to the horizontal test but vertically raised on the rail and communicating over RF, was performed, after which the payload was pumped down for 2-3 days. On launch night, a horizontal test was repeated on the rail, after which the vacuum pump was removed and the rocket sealed. The rocket was elevated, and a vertical test was again performed, followed by the hot count, ending in launch. Two images of pre-launch operations are shown in Figure 2.27, and a calendar of the events leading up to launch operations can be found in Appendix A.

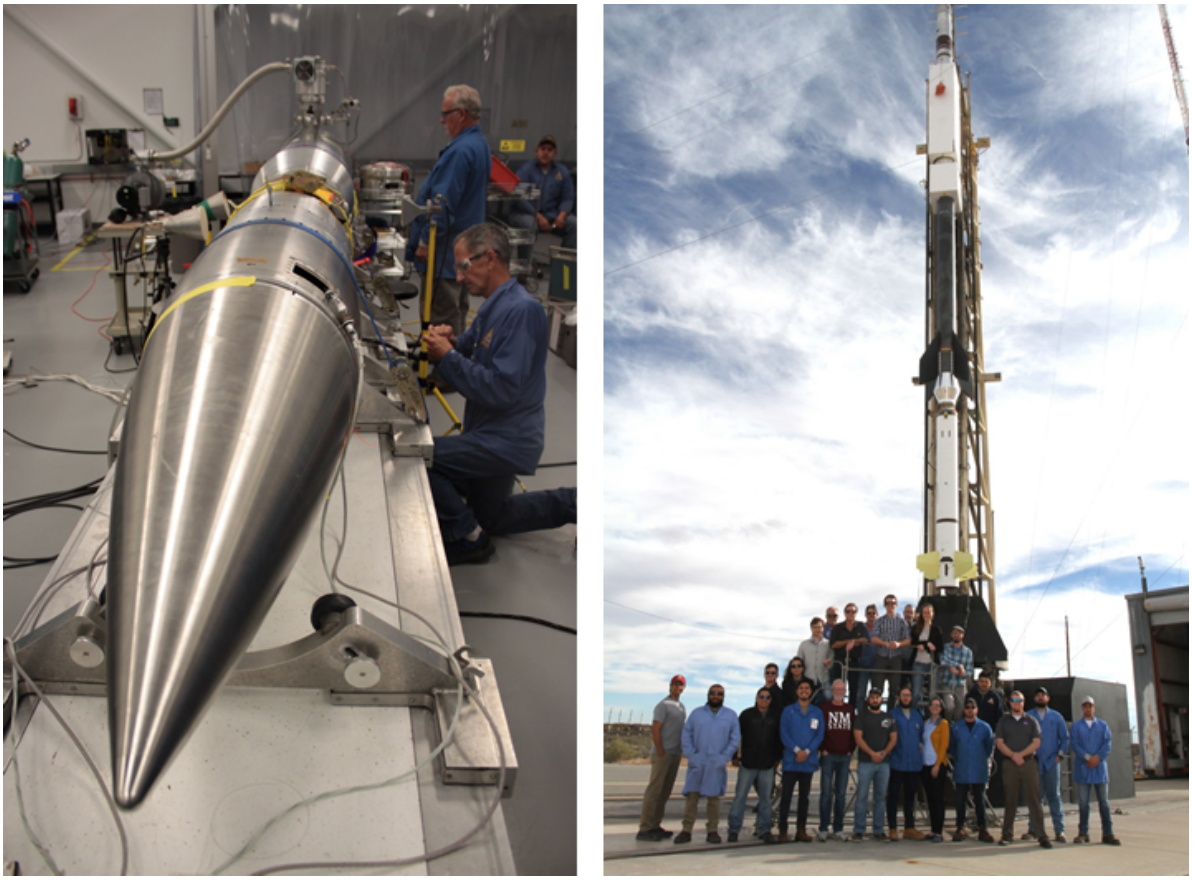

Figure 2.27: Left: NSROC technicians preparing the rocket for a horizontal test at WSMR in 2017. Right: The rocket on the launch pad in 2018.

Chapter 3

The DEUCE Launches, Data Reduction, and Flux Calibration

The DEUCE flights are described and the raw flight data for the DEUCE observation of Epsilon CMa is presented in Section 3.1. The reduction of the raw detector data into an uncalibrated spectrum is outlined in Section 3.2. The process of flux-calibrating the spectrum is discussed in Section 3.3, and the final, flux-calibrated science spectrum is presented in Section 3.4.

3.1 Flights of DEUCE

The DEUCE instrument was launched in October 2017 and December 2018, targeting Beta and Epsilon CMa, respectively. Extensive photographs of the flights and recoveries, alongside a public-facing description of the payload are stored online [22]. A timeline of the events leading up to launch can be found in Appendix A.

3.1.0.1 Flight plans

The DEUCE flight plans were identical for both the 2017 and 2018 flights. Once the attitude control system had locked on and was nominally on-target, the live aspect camera feed was consulted and a slew command would be sent, if necessary, to more precisely center the target star on the high-resolution small aperture sampling the bright FUV. High-resolution data would be collected for a minimum of 10 seconds to acquire a >100,000 raw counts FUV spectrum of the star. The target would then be slewed into the low-resolution large aperture, where it would remain for the rest of the flight (∼300 s) to maximize the fainter, more scientifically-critical EUV spectrum.

Spectra would be obtained and transmitted to the ground for viewing in real time, as would the aspect camera video of the apertures and target.

The timing and altitude of flight events for the 2019 flight are shown in Table 3.1.

3.1.0.2 Flight launch windows

The flight date and launch window were chosen to maximize the elevation of the target at White Sands Missile Range, allowing space for potential launch delays. For each launch, the target was required to be 90 degrees away from the Sun and 45 degrees away from the Moon, with the Sun more than 30 degrees below the horizon. The launch windows were calculated using the ASTROOBS package in IDL and checked using the public software Stellarium [83]. The calculated launch window for the 2018 flight targeting Epsilon CMa is shown in Figure 3.1.

3.1.0.3 Flight 1- Beta CMa

The first flight of the DEUCE payload targeted β CMa and occurred on October 30th, 2017, at 4:00 a.m. local time from White Sands Missile Range. During launch, a NASA gyroscope suffered a reset, leading to a loss of orientation of the rocket, which settled into a final pointing 52 degrees off-target (Figure 3.2). Contingency slew patterns were utilized in an attempt to search for the target, however the offset error was too large for recovery. During contingency slews, no bright star ever crossed the aspect camera field of view or entered either of the apertures, although a small number of extremely faint stars were visible as they passed through the feed. The launch was officially classified as a NASA payload support systems failure, and no science data was acquired. The payload recovered well, with very minimal damage and all components functioning.

3.1.0.4 Flight 2- Epsilon CMa

The second flight of the DEUCE payload targeted ϵ CMa and occurred on December 18th, 2018, at 12:46 a.m. local time from White Sands Missile Range. The launch was a comprehensive success, with over 345 seconds of science data obtained; 23.3 s on the small aperture and 323 s on

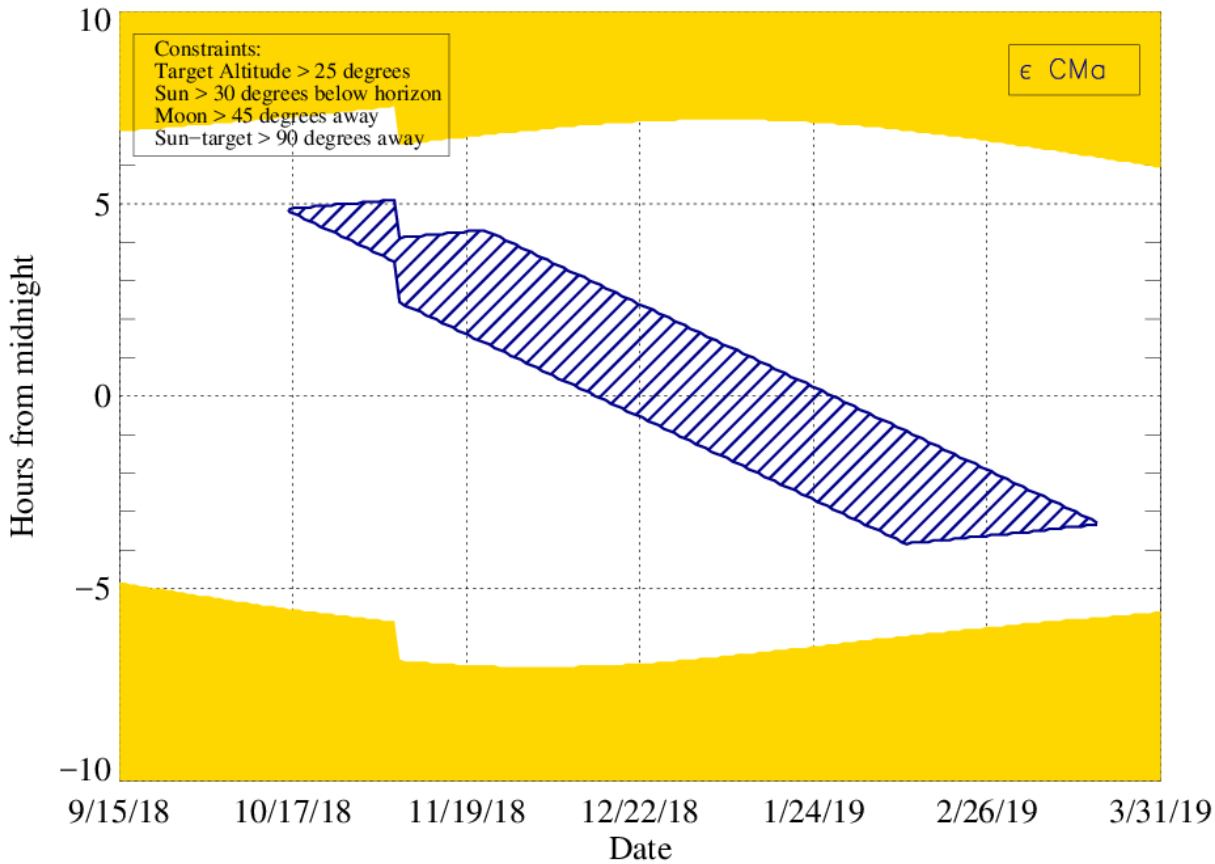

Figure 3.1: The launch window for the 2018 DEUCE flight targeting Epsilon CMa. For each launch, the target was required to be 90 degrees away from the Sun and 45 degrees away from the Moon, with the Sun more than 30 degrees below the horizon.

the large aperture. The payload once again recovered with minimal damage and all components functioning.

3.1.1 Raw flight data for the 2017 and 2018 flights

The raw flight images for both of the DEUCE flights are presented in Figures 3.4-3.6. Figure 3.4 shows the raw detector image for the 2017 flight targeting Beta CMa. As this flight never acquired the star, no flight spectrum is visible; however, scattered light is present. Figure 3.5 shows the small aperture spectrum for the 2018 flight. This image contains 262,302 counts total, with ∼252,000 in the aperture area. Figure 3.6 shows the large aperture spectrum for the 2018 flight,

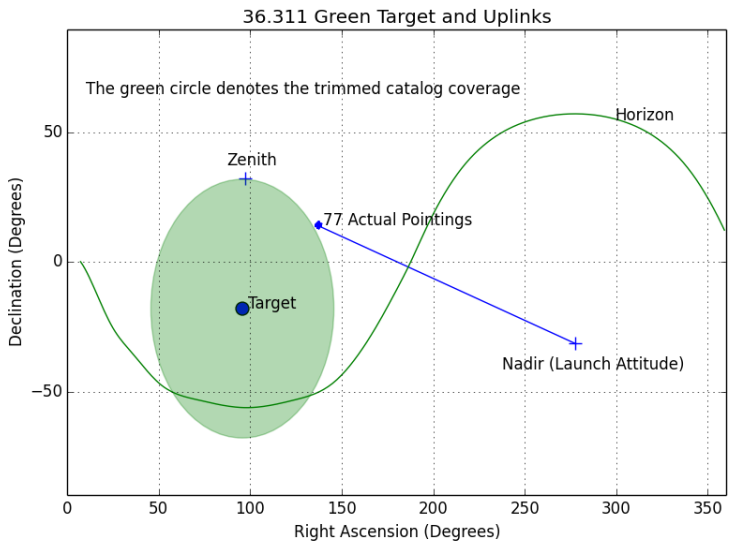

Figure 3.2: The logged ST5000 star tracker pointings from the first flight, taken from [94]. The payload started at the launch altitude and gas jets moved it to a final 'settled' ACS state, around which 77 searching pointings (barely visible at this scale) were performed. The settled location fell 52 degrees away from the target, just barely outside the 50 degree radius sky segment loaded into the ST5000 star tracker computer (green circle).

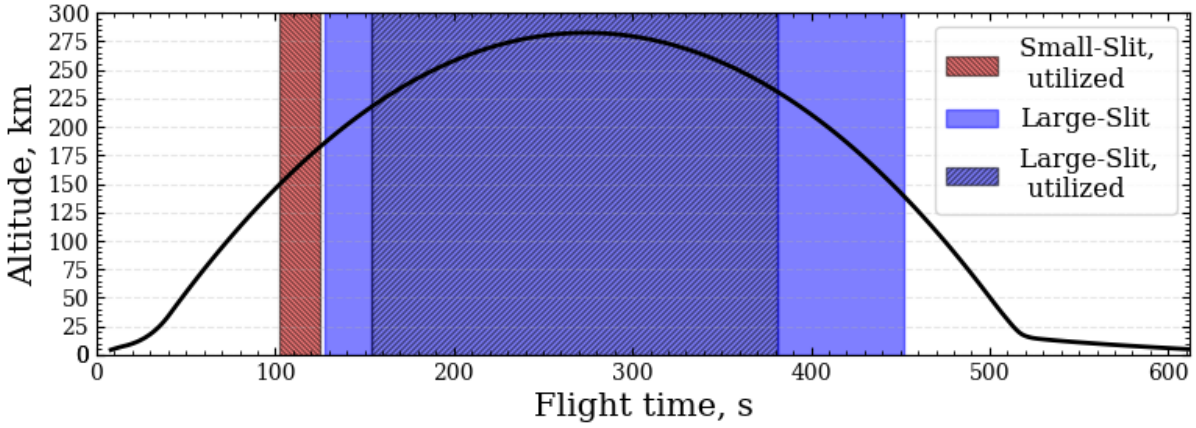

Figure 3.3: The altitude of the payload during the 2018 flight observing Epsilon CMa as a function of time. The portions of the flight in which observations were taken on the small and large aperture are indicated, along with the trimmed section of large aperture data ultimately used for scientific analysis.

which contains 1,507,755 counts total, with ∼195,000 in the aperture area.

Event	Flight Time (sec)	Altitude (km)
Rail Exit	0.6	1.2
Terrier Burnout	6.2	3.0
Black Brant Ignition	16.0	7.7
S19 Canard Decouple	20.0	9.6
Black Brant Burnout	43.5	40.0
Experiment BUS ON	46.0	45.1
Nocturn Camera ON (Back up)	46.0	45.1
De-spin to 0 Hz	62.0	77.5
Payload Separation	65.0	83.3
ACS Control Start	65.0	83.3
ACS Control Start (Back up)	66.0	85.2
ACS Cage GLN-MAC	67.0	87.1
Nose Tip Eject	68.0	89.0
Shutter Door OPEN	75.0	102.0
LED ON	80.0	111.0
LED OFF	82.0	114.5
ACS Arrive on ϵ CMa, small aperture	95.7	137.8
Detector HV ON	102.0	147.7
150 km Upleg (Nominal)	104.4	151.3
Slew to large aperture	125	181.1
Apogee (Nominal)	271.7	282.1
150 km Downleg (Nominal)	439.0	158.9
Detector HV OFF	452.0	138.7
Shutter Door CLOSE	460.0	125.5
Nocturn Camera OFF	461.0	123.8
ACS Spin Up	465.0	116.9
Experiment Power OFF	470.0	108.1
ACS Vent	505.0	28.6
ACS Valves OFF	545.0	11.0
Parachute Deploy (Nominal)	622.4	4.6
Payload Impact (Nominal)	908.5	1.2
ACS Off (Nominal)	950.0	1.2

Table 3.1: The timings and altitudes for various events in the 2018 flight.

3.2 Data reduction of the 2018 observations of Epsilon CMa

After undergoing data reduction, the small and large-aperture images acquired on the 2018 flight formed the basis for the scientific analysis of this thesis. This reduction process broadly consisted of:

- An initial multi-parameter filtering of the data to select only valid counts from the small

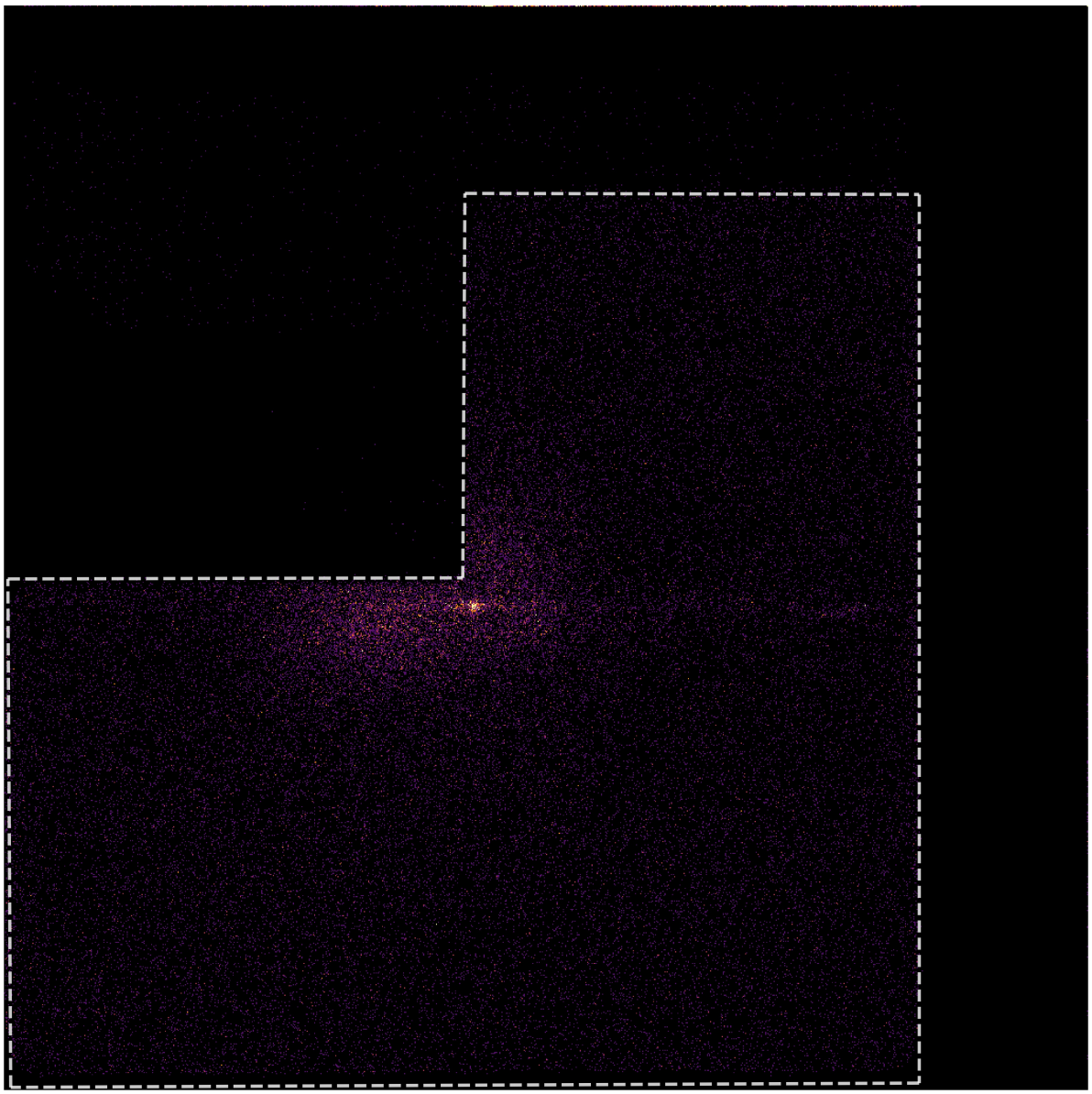

Figure 3.4: The full raw detector image for the 2017 flight, which targeted Beta CMa but never acquired the star. The feature in image center is potentially due to weak scattered light or ions. The dashed white lines indicate the extent of the detector active area.

and large aperture segments of the DEUCE observations

- A summing of the images into one-dimensional spectra with units of counts, followed by noise subtraction

- Consideration of the effects of the Earth's atmosphere on the observations

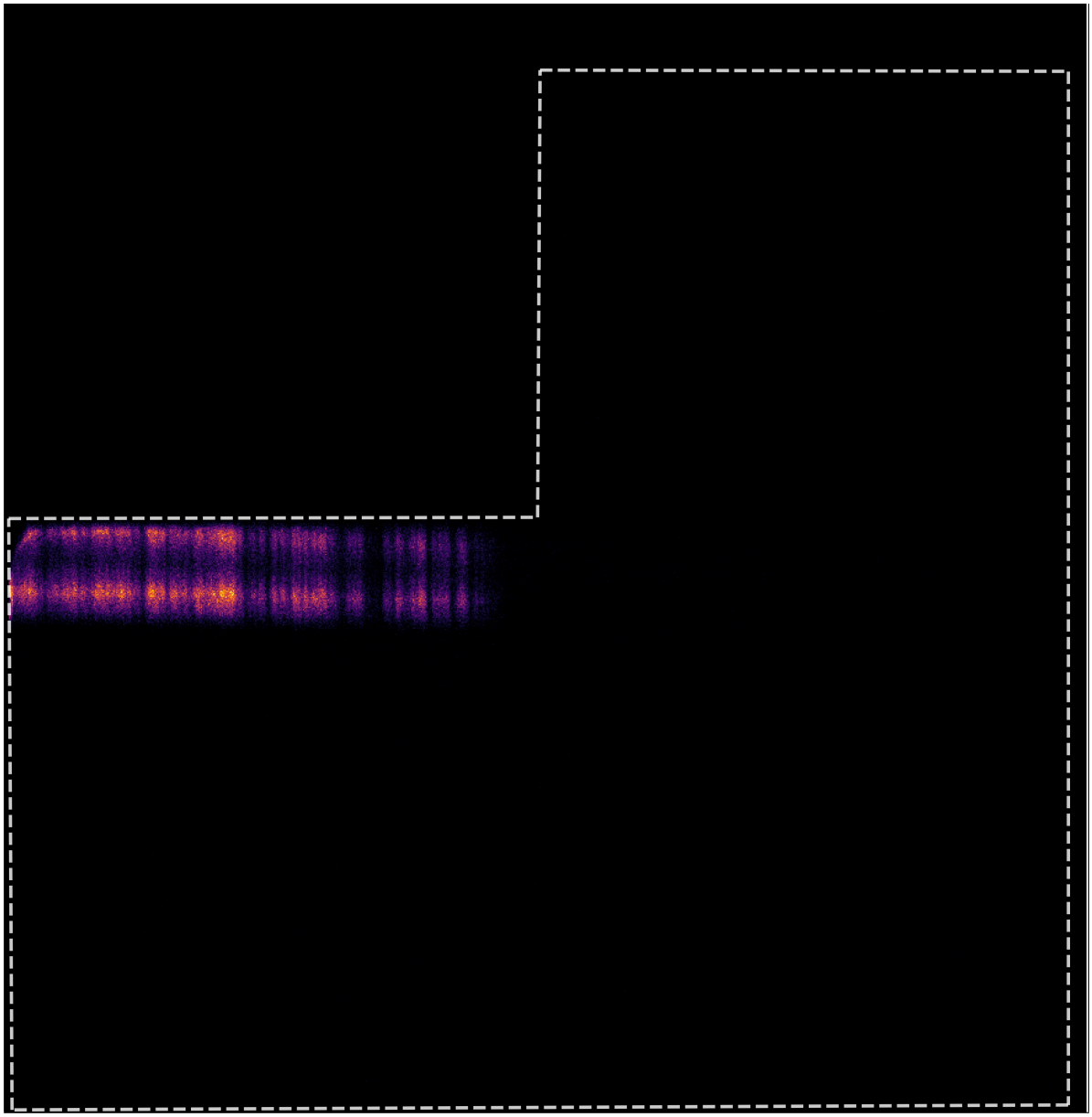

Figure 3.5: The full raw detector image for the 23.3 s small-aperture FUV spectrum, from the 2018 flight. Wavelength decreases from left to right. The dual-lobed nature of the spectrum is due to astigmatism combined with the shape of the complex spot as sampled by the small aperture. The dashed white lines indicate the extent of the detector active area.

- A wavelength and flux-calibration of the spectra into units of ergs/cm^2/s/Å

This overall process is described in the following sections. All image reduction was performed in Python 3.8.3, with both Python and TOPCAT [112] used for quick image inspection.

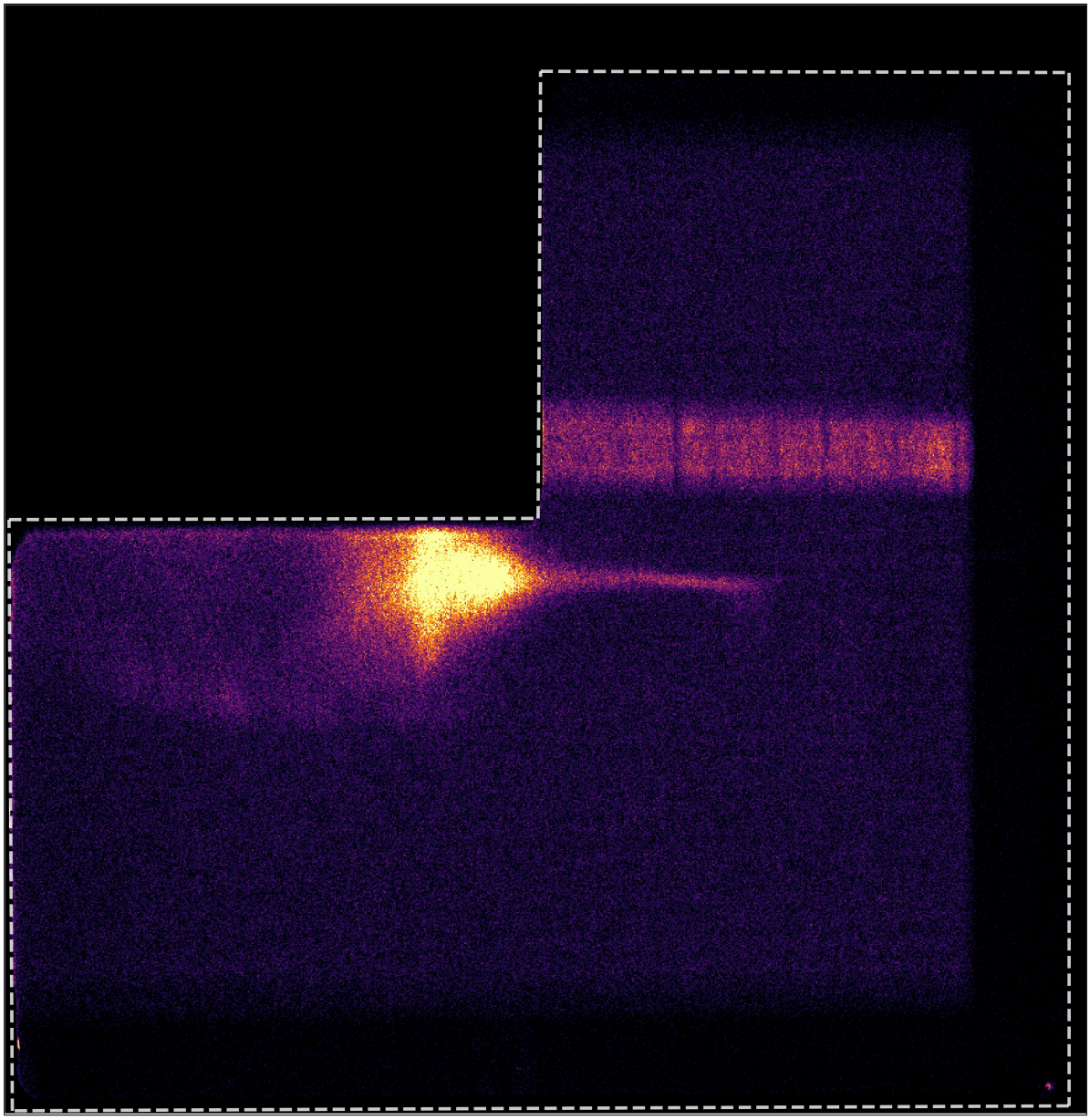

Figure 3.6: The full raw detector image for the 323 s large-aperture EUV spectrum, from the 2018 flight. The science spectrum is the strip of continuum and absorption features just above middle right. Wavelength decreases from left to right. The dashed white lines indicate the extent of the detector active area. The bright feature in detector center is potentially due to scattered light, likely 0th-order stellar continuum, and does not overlap the science spectrum at any point. Hot spots in the MCP may be seen at lower left and lower right. Shadowing of the incoming light by the detector bulkhead is visible on image right.

3.2.1 Filtering

The raw format of the science data returned by the photon-counting MCP detector in flight was a list of 1,777,306 total events consisting of an X coordinate, a Y coordinate, a detector pulse height (roughly equivalent to total charge detected), and a time of detection for each individual detector event. Filtering of the images according to each of these parameters allowed appropriate science spectra to be generated for each DEUCE channel while rejecting spurious or unwanted counts.

3.2.1.1 Pulse height filtering

The pulse height generated by the detector for each registered count was a normalized (0-63) measure of the number of electrons recorded for that event at the detector anode. The distribution of pulse heights (PHD) was useful as a diagnostic tool, as ultraviolet photons tended to produce a distinct pulse height distribution compared to those typically produced by ions and poorly analyzed events.

The flight images were visually examined through a variety of pulse height filters in an attempt to identify and remove these spurious counts (Figure 3.7). Ultimately, counts with pulse heights greater than 49 in the large aperture spectrum and greater than 59 in the small aperture spectrum were visually associated with noise or mis-analyzed events and were filtered out. These filtered counts represented 2% and .59% percent of the total counts in the large and small aperture images, respectively. While the large aperture science spectrum contains two regions of higher intensity (Figure 3.6, spot on top half of spectrum just right of strongest absorption line and bright region on the right end of spectrum), they did not exhibit unusual PHD behavior and I had no reason to question their authenticity.

3.2.1.2 Time filtering

The detector ran throughout the entire flight and collected data continuously, even if the target was not yet centered on the aperture. To identify the exact time period over which each

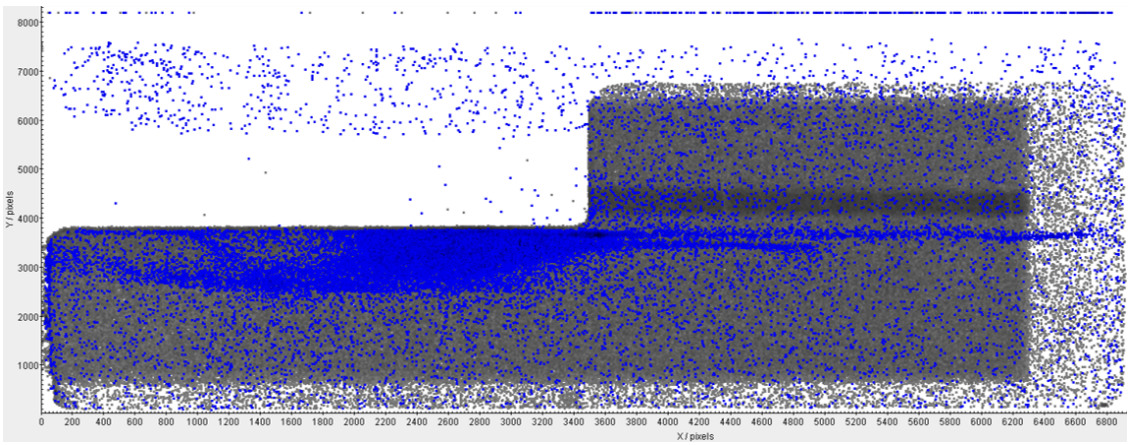

Figure 3.7: A TOPCAT image of the large-aperture exposure, with PHDs 10-19 indicated in grey and 50-63 indicated in blue. The 50-63 PHD counts directly map the feature at detector center and not the flight data, showing the power of pulse height discrimination for removing spurious counts and noise from the data.

spectrum was recorded, the flight images were divided into half second intervals and analyzed according to signal to noise ratio and total count rate across the relevant spectral region on the detector. The final times utilized were 102-125.3 s (∼23.3 s) for the small-aperture channel and 153.8-380.8 s (∼227 s) for the large-aperture channel. The small-aperture time was chosen according to the appearance and disappearance of a stable, constant-flux science spectrum from the small aperture. The start time for the EUV spectrum was similarly determined by the appearance of a stable EUV spectrum, while the end time was set by when the spectrum began to weaken due to atmospheric attenuation (Section 3.2.5). The raw count rates for the small-aperture and large-aperture exposures, as well as the time cutoffs for the filtered data, are shown in Figure 3.8. This time filtering ended up trimming approximately 30% of the large-aperture data and using essentially all of the small-aperture data, leaving 158,971 counts in the large-aperture spectral region and 252,493 counts in the small-aperture spectral region.

3.2.2 Spectrum extraction and background subtraction

To extract a spectrum from the raw images, I first visually determined the vertical extent of both the small and large aperture spectra. In full resolution (8192×8192) this is a vertical

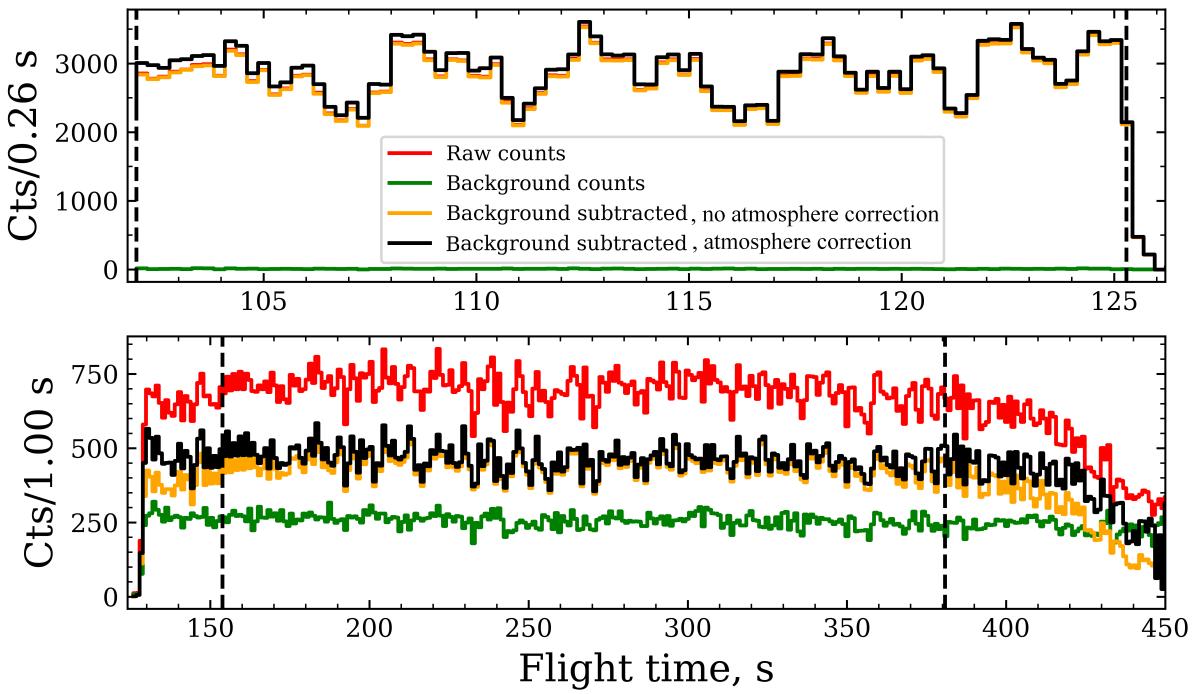

Figure 3.8: Counts vs time as registered on the small (upper) and large (lower) aperture channels. Vertical dashed lines indicate the time-filtered data used in generating the science spectra. Atmospheric absorption strongly affects the EUV and can be seen as the large-aperture spectrum weakens later on in the flight as the rocket altitude decreases.

pixel spread of (3944:4714) for the low resolution spectrum and (3102:3864) for the high resolution spectrum. This vertical region was summed vertically across the entire horizontal extent of the detector, collapsing each science image into a 1D spectrum. An equally-sized region was then extracted either above or below the spectrum, averaged, and subtracted from the spectrum to account for background counts. This subtraction equated to 58,277 counts for the large-aperture spectrum and 942 counts for the small-aperture spectrum, leaving 130,303 and 251,551 counts in the background subtracted large and small-aperture spectra, respectively. The error in each spectrum was calculated by assuming Poissonian $\sqrt{N}$ error in the count space spectrum and combining it in quadrature with the error in the background region as it was subtracted out. Post extraction, the spectra were wavelength-calibrated according to the procedure described in section 2.4.6. No flux was seen in the small-aperture spectrum below 900 Å, and this portion of the spectrum was discarded for all analysis.

3.2.3 Binning

The original resolution of the data is 8192×8192 resolution elements. To increase signal to noise, the extracted spectra were binned by a factor of 8 to 1024×1024 resolution. This binning did not cause a loss of spectral resolution, as DEUCE's limiting resolution was set by the entrance aperture, not by the detector resolution element size, and remained the limiting factor even after this binning.

3.2.4 Final raw/count space spectra

The final wavelength-calibrated, background subtracted, count space spectra of both the small-aperture and large-aperture channel are shown in Figure 3.9.

3.2.5 Atmospheric correction

The Earth's atmosphere readily absorbs UV photons and causes attenuation of variable strength as the rocket passes through different elevations on its flight trajectory (Figure 3.3).

I originally intended to correct for this attenuation in analyzing the DEUCE data, but ultimately decided not to include its effects as I could not trust that it was not introducing time-dependent features into the spectra. The procedure for removing the atmospheric component of the data and my reasons for not including its effects are discussed in the following sections.

3.2.5.1 Establishing a time standard

Before correcting any part of the science exposure for the effects of atmosphere at a particular altitude, I needed to know the rocket's altitude as a function of the time photons were registered on the detector, which involved translating events between multiple temporal frames and establishing a universal time reference frame for the flight.

Three times were involved with the payload launch. The first is the 'detector time' registered by the detector GUI, which was established when the flight data recording was played back to and saved by the GUI post flight. A second is the 'Nocturn time', which was recorded on the aspect

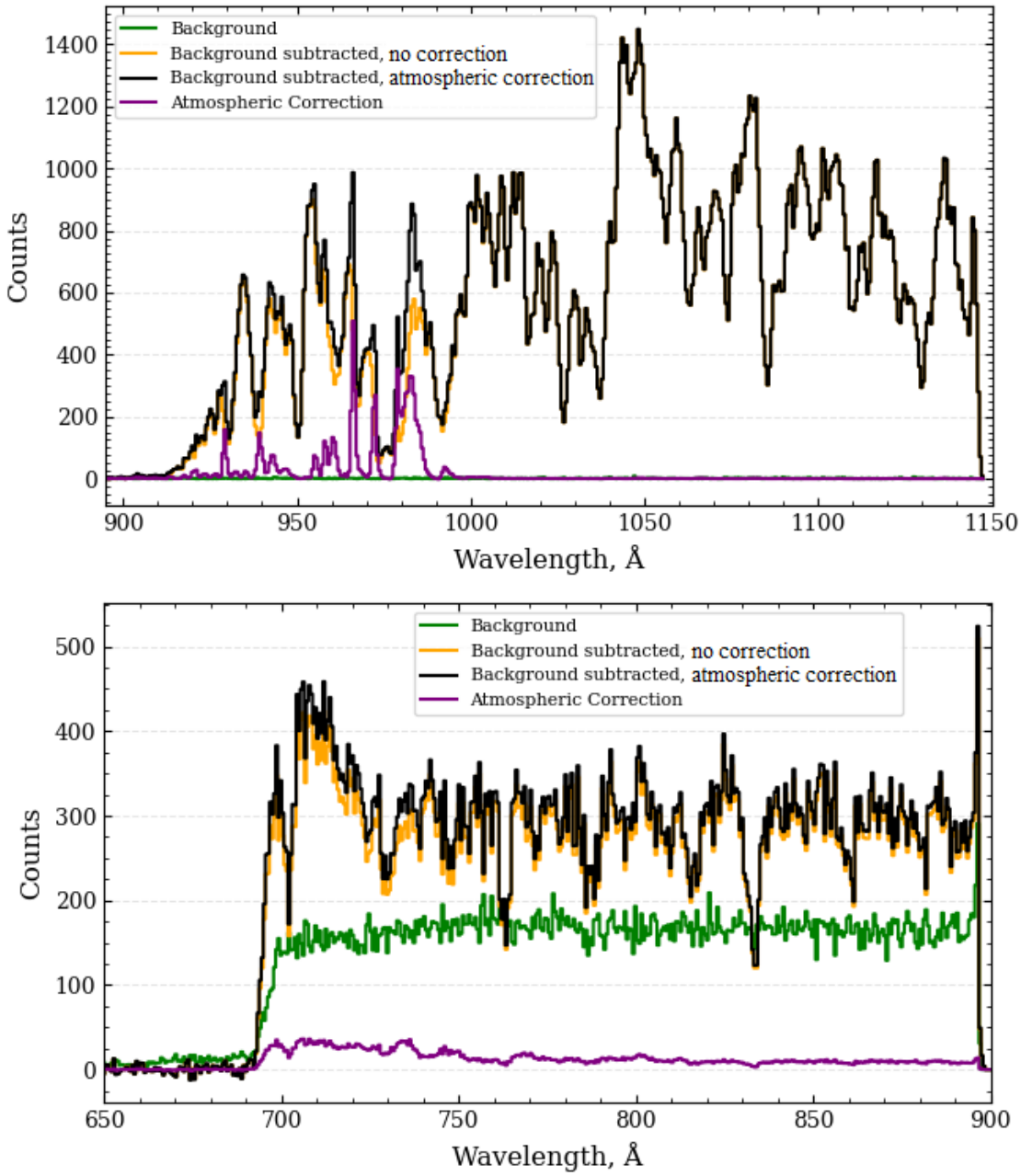

Figure 3.9: The final count-space spectrum of the small-aperture (upper) and large-aperture channels (lower), with the theoretical atmospheric correction included and excluded. The atmospheric corrections were ultimately not used. The error in the spectra (not shown) is a combination of the $\sqrt{N}$ error in the background subtracted spectrum and the $\sqrt{N}$ error in the background itself, added in quadrature.

camera footage provided by NSROC post flight. A third time is 'flight time', which was the pre-set timing programmed into the rocket and controlling events such as the closing of the shutter door

and turning HV on/off, etc.

To establish a standard timescale across all three times, shared events were used. The 'LED-on' command is a scheduled 'flight time' command and can also be seen in the Nocturn video, tying the flight and Nocturn timescales together. Similarly, HV-on is a flight command and corresponds to the first instance of data registered by the detector, tying 'flight time' to 'detector time'. With these connections established, the time of all other flight commands and events can be found in any of the three time reference frames and can be linked to NSROC provided data showing rocket heading, altitude, etc as a function of 'flight time'. This allowed me to determine the rocket altitude as each photon was registered on the detector and estimate the atmospheric absorption at that altitude.

3.2.5.2 Atmospheric models

Models for atmospheric EUV absorption were obtained from Dr. Randy Gladstone [34] at the Southwest Research Institute in Boulder. These models required knowledge of launch date, time, and location, as well as the zenith angle of the target during launch and estimates of recent short and long-term solar activity (10.7 cm solar radio flux on the launch date and during the surrounding 3 months). With these inputs, the models calculated the column density of the main components present in the atmosphere and predicted a wavelength-dependent line of sight attenuation through the atmosphere towards Epsilon CMa as a function of altitude during the launch (Figure 3.10).

I incorporated these models into a basic extraction procedure for the flight data similar to that described in Section 3.2.2. The PHD-filtered data was split into 1 s long segments which were then extracted and background subtracted. The average detector time of each segment was converted into flight time and the altitude was determined from flight logs. Atmospheric models were used to generate an attenuation vs wavelength curve for that particular altitude, which was convolved with the instrumental resolution of either the small or large aperture channel. The extracted spectrum for each time segment was then divided by the predicted attenuation to produce an 'atmosphere-corrected' spectrum. Background counts were not corrected for atmospheric attenuation, as they

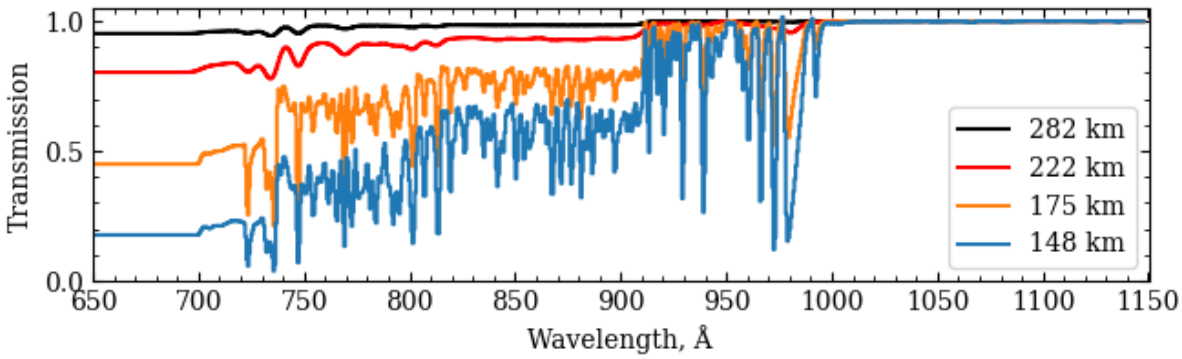

Figure 3.10: Atmospheric model-predicted transmission over the DEUCE bandpass at the altitude of the beginning of the utilized small-aperture exposure (148 km), the end of the utilized small-aperture exposure (175 km), the beginning of the utilized large aperture data (222 km) and apogee (282 km). The two lower altitude transmission curves are shown at the resolution of the small-aperture, while the higher curves are shown at large-aperture resolution.

were likely either detector noise or scattered 0th order light and would not obey the predicted wavelength dependent attenuation. Finally, all of the corrected time segments were summed to produce a final atmosphere corrected flight spectrum for each channel. These atmosphere-corrected count-space spectra can be seen alongside the uncorrected spectra in Figure 3.9.

3.2.5.3 Decision not to use atmospheric correction

While the described atmospheric correction procedure seemed reasonable, I ultimately did not trust its results and did not incorporate it into the flight data reduction process. This decision stemmed from a series of tests of the predictions of the attenuation models against subsets of the data itself in both the small and large-aperture channels.

The first test was based on the assumption that intrinsic flight count rate coming from Epsilon CMa was roughly constant; thus, an accurate atmospheric model would remove the disparate effects of attenuation at various altitudes and correct the observed counts per second to a constant rate over the duration of the flight. As seen in Figure 3.8, even with atmospheric correction, the large-aperture count rate instead drops as the rocket starts to enter lower and lower altitudes and atmospheric correction becomes more and more significant. Although the correction does appear to

extend the duration of a roughly constant count rate an additional 60 s (130-150 s, 380-420 s), the failure of the model to correct the spectrum at times when atmospheric correction was expected to be heavy (t>420 s, altitude <180 km) made me hesitant to trust its predictive power at all other times.

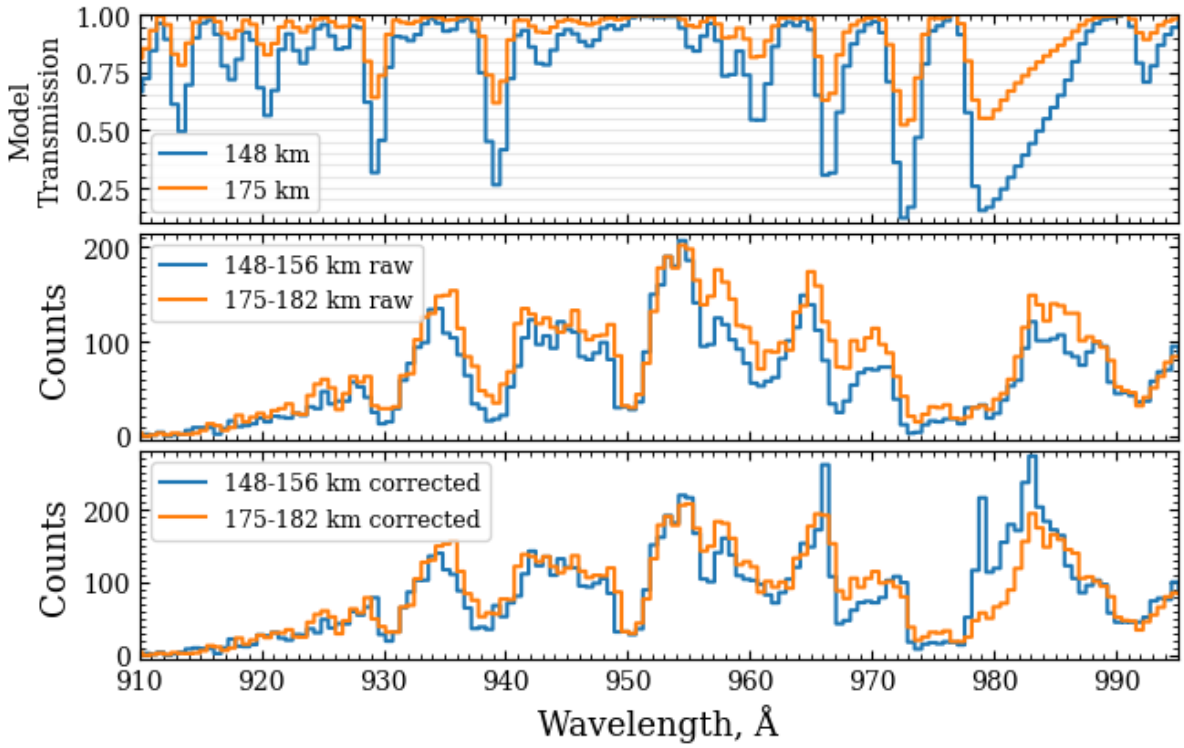

Figure 3.11: Top: Predicted transmission for the highest and lowest altitudes of the small-aperture exposure, showing the large difference in absorption predicted by the atmospheric model over this altitude range. Middle: Raw exposures generated by summing the first and last five seconds of the small-aperture exposure. The first five seconds range from 148-156 km, and the last five seconds from 175-182 km. Differences due to atmospheric absorption are apparent. Bottom: Atmosphere-corrected exposures generated by taking the raw exposures and dividing by the model transmission curves. The model appears to do a good job correcting much of the spectrum, but introduces features at higher wavelengths.

A second test examined the first and last five seconds of small-aperture exposure data. The first five seconds were taken at a lower altitude, 148-156 km, while the last five seconds were taken at a higher 175-182 km, with stronger predicted attenuation. While the model satisfactorily corrected the two segments to a consistent level over much of the spectrum, it also generated emission-line features above 960 Å (Figure 3.11) in the lower altitude data as it corrected for stronger predicted

absorption lines at those lower altitudes. This mismatch in the corrected data at different altitudes was another reason to question the model correction.

For the EUV data, a final quantitative examination of the effect of atmosphere came through splitting the exposure into three time chunks of 40 s each, running from 154-194 s, 254-294 s, and 359-379 s. The first and third such exposure sampled lower parts of the atmosphere than the middle chunk, which was roughly centered on apogee. No difference is seen between the three chunks (Figure 3.12). This implies that atmospheric attenuation was in fact light at these altitudes, precluding the need for atmospheric correction from a model. Based on the behavior of the spectrum as a function of time in Figure 3.8, I would estimate that atmospheric effects only started to be significant for the EUV below 225 km, where they rapidly become important.

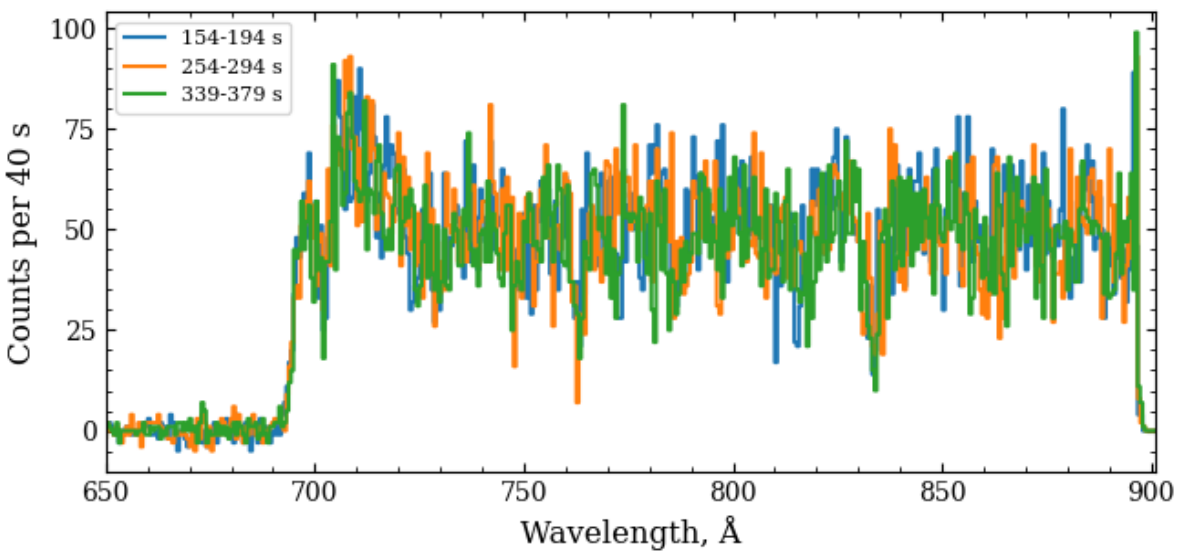

Figure 3.12: Data from three time chunks during the large-aperture exposure, sampling different altitudes. The blue and green data sample lower altitudes (220-260 km), while the orange data samples apogee at >280 km. The datasets are essentially identical, precluding significant atmospheric absorption over the times utilized in the large-aperture science analysis.

3.2.5.4 Implications of not applying atmospheric correction

The results of these tests made me hesitant to embrace the prediction of the model; although the effects of atmospheric correction were clearly present (Figures 3.8, 3.11 middle), I could not

ultimately convince myself that the corrected data was any more scientifically accurate than the uncorrected data, or that atmospheric corrected was even needed for the large-aperture EUV data. I thus did not apply it.

If the models were in fact correct, the decision to not utilize them potentially introduced unquantified error into both the small and large aperture spectra. At the resolution of the large-aperture spectra, ignoring a real atmospheric attenuation at the predicted magnitude would entail underestimating the observed stellar flux, with this effect increasing at shorter wavelengths, as shown in Figure 3.10, where the atmospheric transmission is predicted to increase by 17 % at 750 Å and 6% at 900 Å when moving from 222 to 282 km and by 13%/2%, respectively, when considering a fixed altitude (222/282 km) and looking at the 750 Å vs 900 Å transmission.

These are conservative upper limits to the error, as the payload spent most of the large-aperture observation time near apogee, where overall atmospheric absorption and the difference between 750 Å and 900 Å attenuation is minimized. Furthermore, since both the large and small-aperture spectra were ultimately scaled to satellite observations, only relative flux differences would have any effect on the data. Based on the tests described above, any significant atmospheric effects likely only affected the small-aperture FUV data, taken below 180 km. Since the more important, novel, and scientifically relevant data of the DEUCE experiment is the large-aperture EUV which suffered minimal atmospheric effects, I did not consider my decision to ignore atmospheric effects to be ultimately problematic.

3.3 Flux calibration

The end goal of the payload flux calibration was to convert from the count-space spectra to flux calibrated spectra in units of ergs/cm^2/s/Å that could then be compared to the literature and analyzed scientifically. This process is described sequentially below.

- Prior to flux calibration, the data in each channel took the form of a wavelength-calibrated spectrum and associated error, each with units of [counts/pixel].

- Each count comes from a photon with an energy in units of ergs, associated with its wavelength. I divided each pixel's count by the energy in ergs corresponding to a photon of the wavelength at that pixel. Technically this introduced a small error as the pixels have width, and the wavelength at one end vs the other is slightly different; an 'average' photon energy at that pixel is being used. This error is negligible and was ignored. The units of the spectra then became [ergs/pixel].

- Since pixels are not infinitely small, each pixel does not represent an infinitely small region in wavelength space; rather, each pixel collects photons from a range of wavelengths that all fall into its physical boundary. I thus divided the spectra by the number of angstroms dispersed across each pixel, as calculated by the wavelength calibration. This also introduced error, as the wavelength calibration is not perfect; however, this error is universally ignored by astronomers and was similarly ignored here. The units of the spectra then became [ergs/Å].

- The spectrum was not detected instantaneously; rather, it represents photons detected over the duration of the flight. I thus divided the values by the total length in seconds of the utilized portion of the exposure for each channel (227 s for the large aperture and 23.274 s for the small aperture). This assumes a constant count-rate over the flight, which is a fairly good approximation (Figure 3.9). The time values of the start and end of each exposure are well known and any error introduced by their uncertainty is taken to be negligible. The units of the spectra then became [ergs/s/Å].

- The detected spectrum was acquired using an instrument with a collecting area of a specific size; a larger or a smaller collecting area would have produced a stronger or fainter raw spectrum, respectively. Furthermore, DEUCE presents a different effective collecting area at different wavelengths, making it more or less efficient at collecting photons across the DEUCE bandpass (Figure 2.18). This was accounted for by dividing out the DEUCE effective area from the spectra. This division contained error due to the error in the measurements generating the DEUCE effective area curve, which was propagated into the

calibration. The units of the spectra then became [ergs/cm^2/s/Å]. This is the final, flux-calibrated form of the spectrum.

3.3.1 Scaling of the calibrations

The described flux calibration produced the best estimate of the spectrum of Epsilon CMa in the absence of any other observations. As a check of this calibration, I compared the resultant flux-calibrated small and large aperture spectra to existing satellite observations with which they had overlap or near overlap. For the small-aperture channel, I compared my spectrum from 1100-1143 Å to observations from the IUE satellite which observed above 1150 Å. For the large-aperture channel, I compared my large aperture spectrum from 700-730 Å spectrum to observations from the EUVE satellite, which observed below 730 Å.

In both instances, I found disagreement between the DEUCE flux calibration and the fluxes observed by these satellites. Since I trusted the rigorous calibration procedures for these satellites more than I did my own DEUCE calibration, I decided to treat the DEUCE calibration as a relative measurement and scaled my flux-calibrated spectra to match these satellite observations. This procedure is described below for each of the DEUCE channels.

3.3.1.1 Small-aperture flux scaling

It was not surprising that the flux-calibrated small-aperture spectrum did not match IUE satellite observations, as it was essentially only relatively calibrated due to the uncertain transmission of the spot through the small aperture in flight (Section 2.4.2). Thus, scaling to existing datasets was always a known requirement for accurately flux calibrating the small-aperture data.

Unlike the large-aperture channel, there is no direct overlap between the DEUCE small-aperture channel and other flux-calibrated FUV datasets. The closest matching data is that of IUE, running as low as 1150 Å, almost touching the DEUCE bandpass edge of 1144 Å. The IUE data selected for comparison was observation "SWP54335" [96], which was chosen as it is a high quality, high resolution observation using the large aperture mode of IUE, which has more reliable

calibration than its small aperture mode [77].

Since no overlap exists, the mean values of the edges of each dataset were compared to generate a scale factor, utilizing the 1100-1143 Å region for DEUCE data and the 1150-1170Å region for IUE. The multiplicative difference between the averages of these abutting regions, 6.82, was considered the 'nominal' scale factor used to match the DEUCE FUV to the flux-calibrated IUE data (Figure 3.13). The DEUCE FUV small-aperture data and its associated error were multiplied by this value to produce the final DEUCE small-aperture spectrum (Figure 3.16). After scaling, the DEUCE data matches both UVSTAR and Voyager FUV data to within a factor of 1.5 [42].

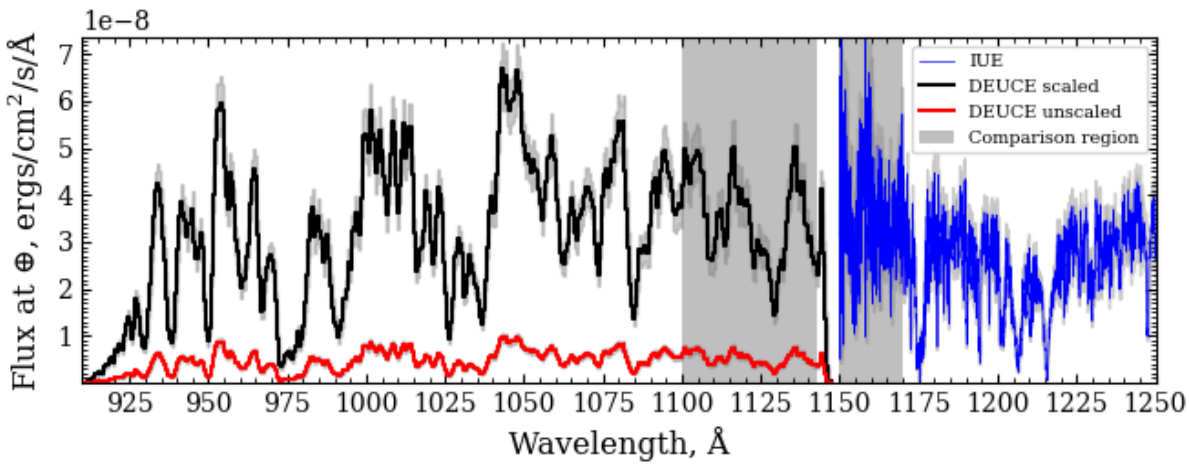

Figure 3.13: The small-aperture data before and after scaling to IUE satellite observations. The region in each spectrum used for scaling is highlighted in grey.

3.3.1.2 Large-aperture flux scaling

In the large aperture channel, overlap existed between the 696-730 Å portion of the DEUCE spectrum and EUVE satellite observations below 730 Å.

While the EUVE satellite operated in bandpass from 70-760 Å, all of the EUVE data products for Epsilon CMa on the MAST archive only extend up to 700 Å. Furthermore, although the originally published EUVE spectrum for Epsilon [10] shows a plot of the spectrum that extends up to 730 Å, it provides no raw data products.

Since the lower end of the DEUCE bandpass begins at 696 Å, it was crucial to obtain the

700+ Å portion of the EUVE spectrum of Epsilon for accurate scaling. This spectrum was obtained via private communication with Dr. John Vallerga, part of the EUVE science team, who provided me with an EUVE observation of Epsilon CMa in units of counts, along with the spacecraft effective area as a function of wavelength. I slightly shifted the wavelength scale of these observations to match the MAST archive and the original published spectrum. From these data, along with the exposure length and bin size in Å, I generated a flux-calibrated EUVE spectrum that closely but not exactly matched the flux of the originally published spectrum while extending its coverage an additional 50 Å upward to 750 Å.

I scaled the DEUCE large-aperture data to this flux-calibrated EUVE spectrum by minimizing the chi-square difference between the EUVE flux and scaled DEUCE datasets across the 700-729 Å region of both spectra (Figure 3.14), accounting for the error in each spectrum and allowing the scaling to vary as a free parameter. The 700 Å lower limit of this region was chosen to be sufficiently far from the edge of the DEUCE spectrum to avoid any edge effects, and the 730 Å upper limit was similarly chosen to avoid a suspect rise in the EUVE data near its edge.

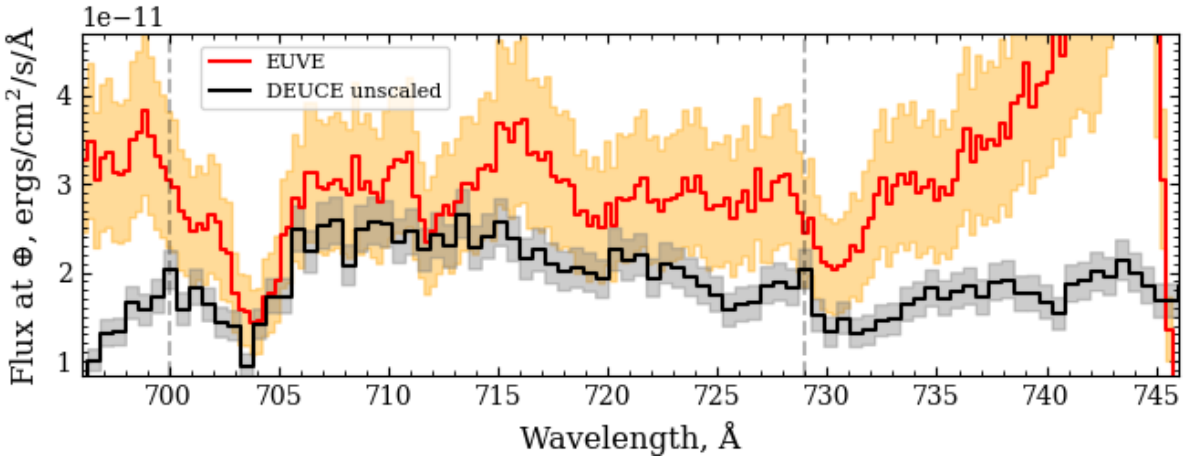

Figure 3.14: The 696-745 Å overlap region between EUVE satellite observations (70-745Å) and the DEUCE large-aperture observation (696-895 Å). Dashed vertical lines indicate the shared region used to scale the DEUCE data to EUVE using least-square minimization. Error in the EUVE and DEUCE data is shown with orange and grey shading, respectively.

The best fit scale factor which used to ultimately scale the data was a multiplicative scaling

of the DEUCE data by 1.33 to match the EUVE flux. The scale factor range allowed by a 1σ variation of the reduced chi-squared of the scaled DEUCE data compared to the EUVE spectrum was .98-1.68. These limits set the range over which the scale factor was allowed to vary when it was used as a free parameter during later stellar model fitting to the data (Section 4.3.3).

At first glance, this 1.33× scaling might be attributed in part to the lack of atmospheric correction I applied to my data; if atmospheric absorption is present, then my uncorrected data would be attenuated, and its true value would be larger than I claim. However, I believe that Figure 3.12 is strong evidence for a lack of atmospheric absorption over the range of times I selected to constitute the large-aperture data. Even if atmospheric attenuation were present, I estimated its maximum contribution at 6-17% across the DEUCE bandpass, which cannot explain the full 33% increase, although it would decrease the discrepancy and bring the datasets' 1σ error bars into agreement. Nonetheless, for the reasons mentioned, I do not believe that atmospheric correction is the cause of the mismatch, which remains unexplained.

The utilized EUVE-DEUCE overlap region and the best-fit scaling for the large-aperture data is shown in Figure 3.15

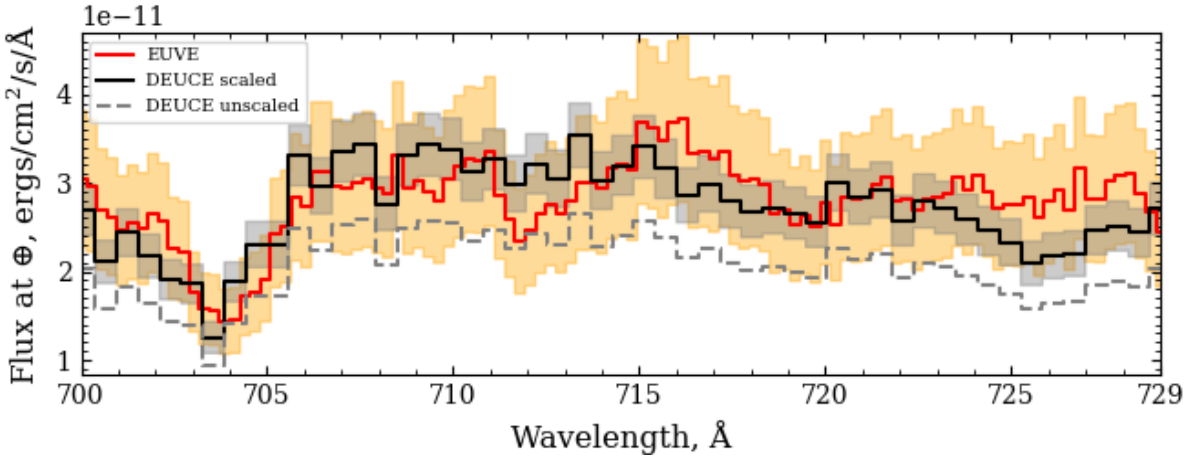

Figure 3.15: The 700-729 Å region of the DEUCE large-aperture observations used to scale to EUVE, both before and after scaling. The unscaled DEUCE large-aperture data is shown with a dashed line. Error in the EUVE and DEUCE data is shown with orange and grey shading, respectively.

3.4 The final flux calibrated spectrum

The final scaled, flux calibrated spectra of Epsilon CMa taken with the small and large-aperture channels, along with data from the IUE and EUVE satellites, are shown in Figure 3.16-3.17, with the observations placed in the context of the IUE and EUVE observations to which they were scaled in Figure 3.18. These spectra are those utilized for scientific analysis in Chapter 4.

A table of the flux-calibrated DEUCE EUV and FUV data is stored and accessible online [22].

3.4.1 Sub-911.7 Å flux in the small-aperture channel

Figures 3.16 and 3.18 appear to show FUV flux below 911.7 Å and roughly matching the expected flux at those wavelengths suggested by Figure 3.17, potentially signifying EUV flux detected through the small aperture (which would increase the EUV coverage of DEUCE up to the Lyman Limit and potentially allow for a separate calibration and estimate of aperture transmission for the small aperture channel).

Upon examination, I do not believe that this flux is legitimate and have ignored it in all my analyses. This is largely due to the fact that the effective area of the FUV channel does not vary by more than a factor of 2 across its bandpass, meaning that the sensitivity of the channel from 900-911 Å is roughly the same as its sensitivity from 800-900 Å. Since the sub 911.7 Å EUV attenuation is strongest at 911.7 Å and decreases at lower wavelengths, this implies that, were the small-aperture channel able to detect EUV flux from 900-911 Å, it would be able to detect it below 900 Å as well. As this is not the case, I declared the flux to be spurious, even though it is tantalizingly and coincidentally close to the level expected if it were real.

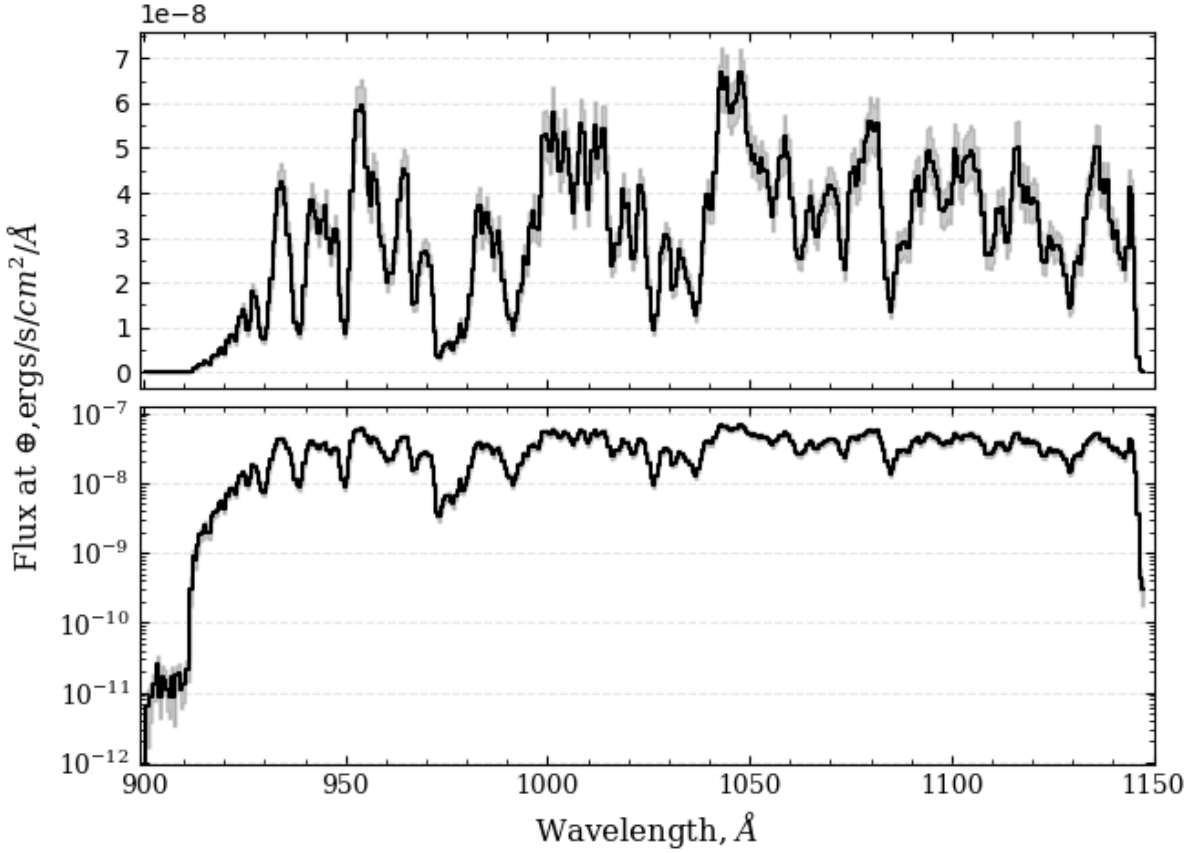

Figure 3.16: The final flux calibrated FUV spectrum of Epsilon CMa produced by the DEUCE instrument in linear (upper) and log (lower) space.

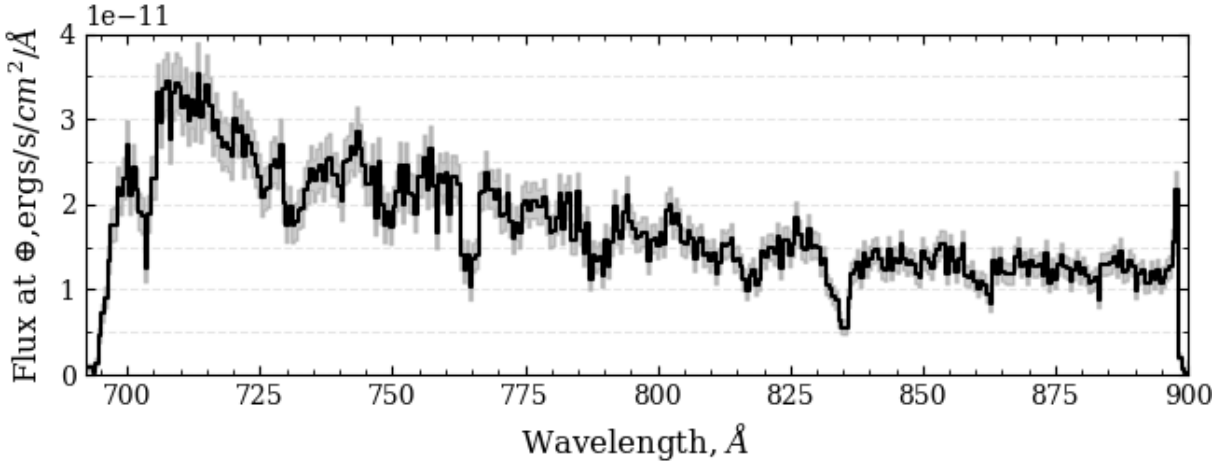

Figure 3.17: The final flux calibrated EUV spectrum of Epsilon CMa produced by the DEUCE instrument.

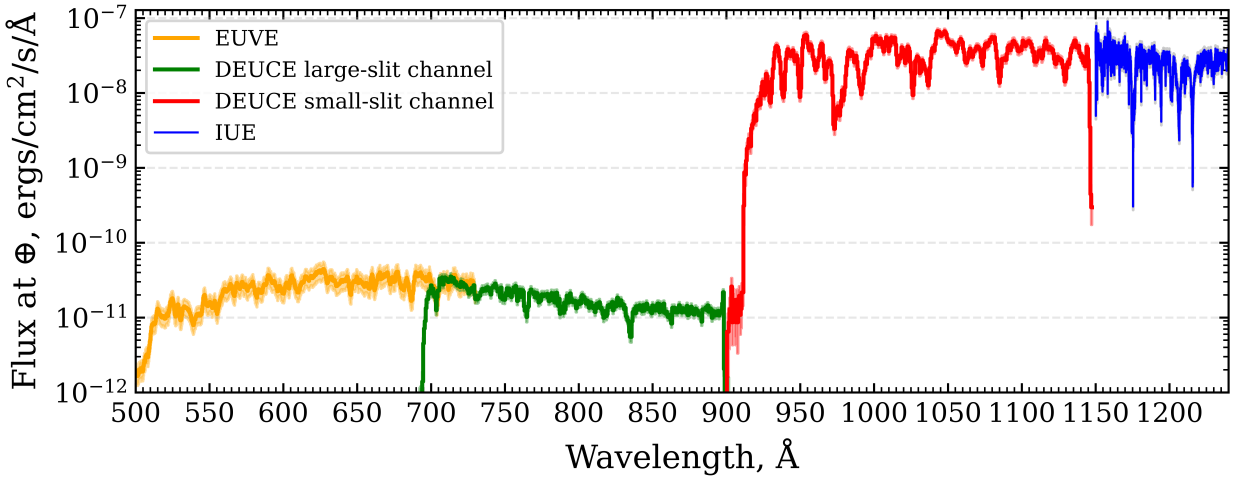

Figure 3.18: The final flux calibrated spectrum of Epsilon CMa produced by the DEUCE instrument, combining data from both the small and large-aperture channels. EUVE observations up to 730 Å and IUE observations above 1150 Å are also shown.

Chapter 4

Model Fitting

In this chapter, I describe model fitting I performed between DEUCE and EUVE observations and multiple stellar models in both the EUV and the FUV. This modelling was performed with the goal of verifying if the situation outlined in Chapter 1 is true: do current stellar models truly underpredict the EUV flux of Epsilon CMa by a large factor? Are these stellar models inaccurate, and are they contributing to a significant underestimation of the ionizing contribution of B stars in the Universe? In light of the potential discrepancies between the models and the observations, does the role that B stars play in helping to generate the UVB need to be reassessed?

To explore these questions, I performed a χ^2 minimization between ATLAS9, TLUSTY, and Aufdenberg stellar models and DEUCE, EUVE, and combined EUVE-DEUCE EUV observations, accounting for the EUV-attenuating effects of N(H I) and the uncertainty in the DEUCE EUV flux-scaling. Further fitting was performed between the models and the DEUCE FUV spectrum, as well as combined EUV and FUV observations. From these minimizations, 1D individual N(H I) and 2D joint (N(H I), T) $\Delta\chi^2$ confidence intervals for the models were generated, along with χ^2_ν values for each of the model-observation fits.

The models utilized for this fitting are described in Section 4.1. The observations and their preparation for fitting are described in Section 4.2. The parameter space of models considered in the fits is described in Section 4.3. The EUV and FUV fitting procedures are described in Section 4.4. The EUV fitting results are presented and discussed in Section 4.5. The FUV and combined EUV-FUV fitting results are presented and discussed in Sections 4.6 and 4.7. A final conclusion,

along with a discussion of future improvements to the fits and observations, is presented in Section 4.8.

4.1 The stellar models

While many models were explored as candidates for comparison with the observations of Epsilon CMa, I ultimately settled on three sets of models that covered the DEUCE/EUVE bandpasses and spanned a temperature, surface gravity, and metallicity range that included the various estimates of these parameters for Epsilon CMa. These specific models were chosen for their widespread use and availability as pre-published grids (ATLAS9, TLUSTY) or specificity to Epsilon CMa (Aufdenberg). The three chosen models are not the only such in existence (e.g. [93], [101]); however, many potential candidates do not fully cover the wavelength or parameter range of the DEUCE and EUVE data and were unsuitable (e.g. MARCS [82], >1300 Å, log_g > 4, CMFGEN [26], >900 Å, POLLUX [89], >3000 Å).

4.1.1 ATLAS9 grids

ATLAS9 [13] is a commonly used 1D plane-parallel LTE atmospheric modelling code predicting fluxes over a wide range of stellar types and parameters. The models I used for fitting consisted of prescribed grids of stellar spectra covering 9 Å-1.6 μm and calculated for various combinations of temperature, surface gravity, metallicity and turbulent velocity. The models are published online [12] in native units of ergs/cm^2/s/hz/sr, and were multiplied by $4\pi c/\lambda^2$ to convert to ergs/cm^2/s/Å and match the units of the DEUCE spectrum. The models as accessed are low resolution (10 Å bin size).

4.1.2 TLUSTY grids

TLUSTY [64] is a nLTE, line blanketed, plane-parallel, hydrostatic model atmosphere code which specifically generates synthetic spectra of early-type stars. I utilized online published grids [65] of computed spectra, run from 44 Å-30 μm in units of ergs/cm^2/s/Å. The models as accessed

are at least as high resolution as the DEUCE FUV data, and their average bin size in the DEUCE EUV bandpass is approximately .4 Å.

4.1.3 Aufdenberg N2 and N7

Aufdenberg et al. created multiple non-LTE, line blanketed models [2] specifically describing Epsilon CMa and attempting to better treat its EUV flux. The predictions of two such models (N2 and N7) in units of ergs/cm^2/s/Å were provided by Dr. Aufdenberg via private communication and utilized in my analysis. These models were not grids; they are two individual models specifically run for Epsilon CMa using its best-known parameters at the time (T=21,750, log g =3.2 (N2) / 3.5 (N7)). In Aufdenberg's original analysis, the N2 model was found to be the best fit to EUVE data of Epsilon, while the N7 model largely mirrored N2 but with slightly stronger EUV flux. Both sets of models are high resolution (R >30,000), with a variable bin size that decreases around spectral features. The models run from 300-1000 Å, and so were unsuitable for comparison with the DEUCE FUV spectrum.

4.2 The observations

4.2.1 EUV observations

I compared three sets of EUV observations to the listed stellar models: the new DEUCE EUV observation, EUVE satellite observations, and a combination of the DEUCE and EUVE EUV observations.

The DEUCE EUV observation was the flux-calibrated spectrum shown in Figure 3.17, taken at a resolving power of R=180. This DEUCE data was trimmed to 700-894 Å to remove edge effects.

The utilized EUVE observation came from private communication with Dr. John Vallerga of the EUVE science team and was the same spectrum used for scaling the DEUCE EUV data. This data extended up to the full 730 Å edge of the EUVE spectrometer, like the spectrum shown in

(but not provided by) the original EUVE publication concerning Epsilon [10] and unlike publicly accessible MAST archival data, which cuts off at 700 Å. The observations provided by Dr. Vallerga were shifted in wavelength to match MAST archival spectra and the original published spectrum. The EUVE data was trimmed to exclude wavelengths below 505 Å, which would experience attenuation by neutral helium that was not accounted for in the fitting, and above 700 Å, where the DEUCE data begins. In this bandpass, EUVE had a resolving power of approximately 300 [1].

To allow for comparison between the models and the full EUVE/DEUCE EUV dataset, the DEUCE and EUVE observations were simply joined together. This combined spectrum is shown in Figure 4.1.

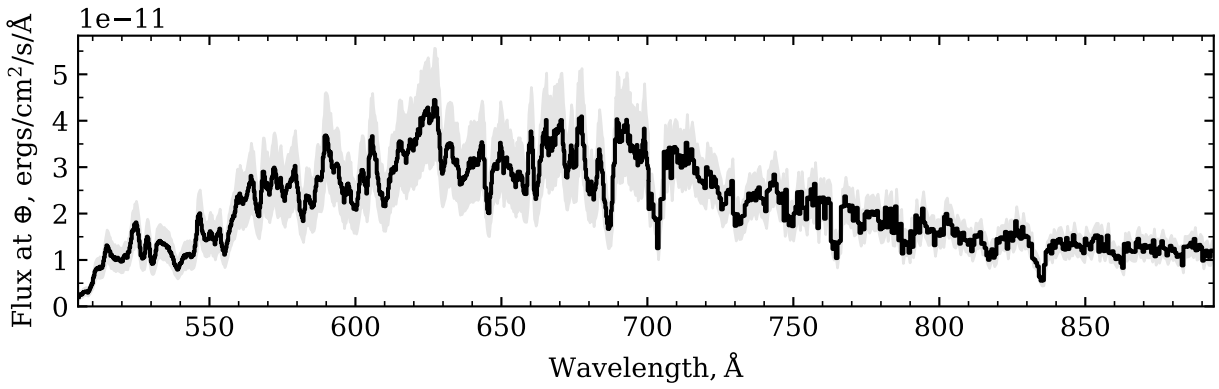

Figure 4.1: The combined 505-894 Å DEUCE/EUVE dataset as used in the model fitting.

4.2.1.1 FUV observations

I performed all FUV fits using the 915-1142 Å portion of the DEUCE small-aperture FUV data, taken at a resolving power of R=1800 and previously shown in Figure 3.16.

4.2.1.2 Combined EUV/FUV observations

I also compared the models against combined EUV and FUV observations. For these fits, the relevant EUV observations (DEUCE, EUVE, combined EUVE/DEUCE) were simply joined to the DEUCE FUV observations.

4.2.2 Conversion to surface fluxes

To facilitate comparison between the DEUCE/EUVE observations, taken at Earth, and the model predictions in units of flux at the stellar surface, all of the observations were scaled into units of surface flux by multiplying by $\frac{d^2}{R^2}$, where d is the distance to Epsilon CMa and R is the stellar radius. Utilizing the relationship between radius, angular diameter, and distance, $R = \frac{\theta}{2}\frac{d}{206265}$, and $\theta = .77 \pm .05\ mas$ as an average of stellar angular diameter estimates [49, 115], this becomes a multiplicative factor of:

$$\frac{d^2}{R^2} = \frac{206265^2 \times 4}{\theta^2} = 2.87 \times 10^{17}\,, \tag{4.1}$$

The error contained in the utilized angular diameter measurement was propagated into the error of the scaled observations. This scaling of the observations into surface fluxes using Epsilon's angular diameter is distinct from the 'scale factor' parameter in the EUV model fitting (Section 4.3.3), which was instead tied to the uncertainty in the scaling of the DEUCE large-aperture flux to EUVE. Since the observations taken at Earth also include the effects of N(H I) absorption present in the stellar sightline, the EUV portions of all models were attenuated by various N(H I) columns as part of the fitting routine (Section 4.4).

4.2.3 Binning of observations/convolution of models

Meaningful comparison of the models and the observations required that each be matched in resolution and bin size/position. χ^2 fitting requires sampling at the same locations for observation-model comparison, so the disparately-spaced data points of the models and observations had to be re-sampled to the same wavelengths without losing information or creating aliasing.

Since there was also a resolution mismatch between the models and observations, narrow, resolved spectral lines present in a high resolution model like Aufdenberg would necessarily not be matched by the lower resolution DEUCE observations and would create spurious error in the χ^2 fit, even if the model were perfectly accurate from a physical/spectroscopic perspective. Similarly,

if a low resolution model like ATLAS9 were compared to the higher resolution, more finely binned DEUCE data, the sub-model-resolution noise and spectral features present in the observations would generate meaningless error.

To account for this, all models with higher resolution than the DEUCE/EUVE data (TLUSTY, Aufdenberg) were convolved to an appropriate Gaussian instrumental profile for the EUV DEUCE/EUVE or FUV DEUCE observations, interpolated, and re-sampled onto the observational data-points. As the interpolation occurred after the convolution to the observational resolution, no excess error was introduced during the interpolation; prior to the interpolation, no features existed in the convolved models on a smaller scale than the resolution of the observations, and the models were smoothly varying and continuous.

When higher resolution observational data was compared to the low resolution ATLAS9 models, the observations were instead binned to the same bin size and location as the ATLAS9 predictions. Convolution of the data to the model resolution was also considered, and was found to match the produced spectrum of the binning procedure to within 10% at all points and often to within just a few percent. Convolution was ultimately not used, however, because while it accurately broadens the observations, it does not correctly treat the observation error, which is reduced by the process of binning to the larger ATLAS9 bin size.

A block-diagram of the data/model preparation process is shown in Figure 4.2, while an example of the convolution and binning processes is shown in Figure 4.3.

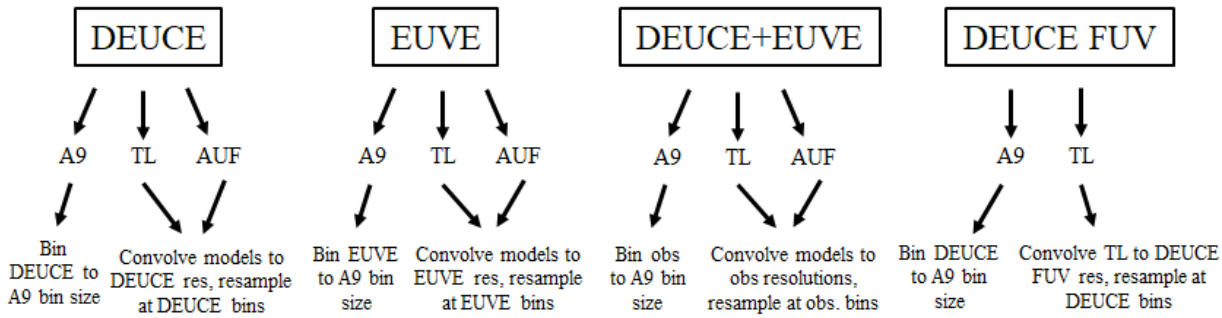

Figure 4.2: The binning/convolution process for each model/observation combination in preparation for the χ^2 fitting.

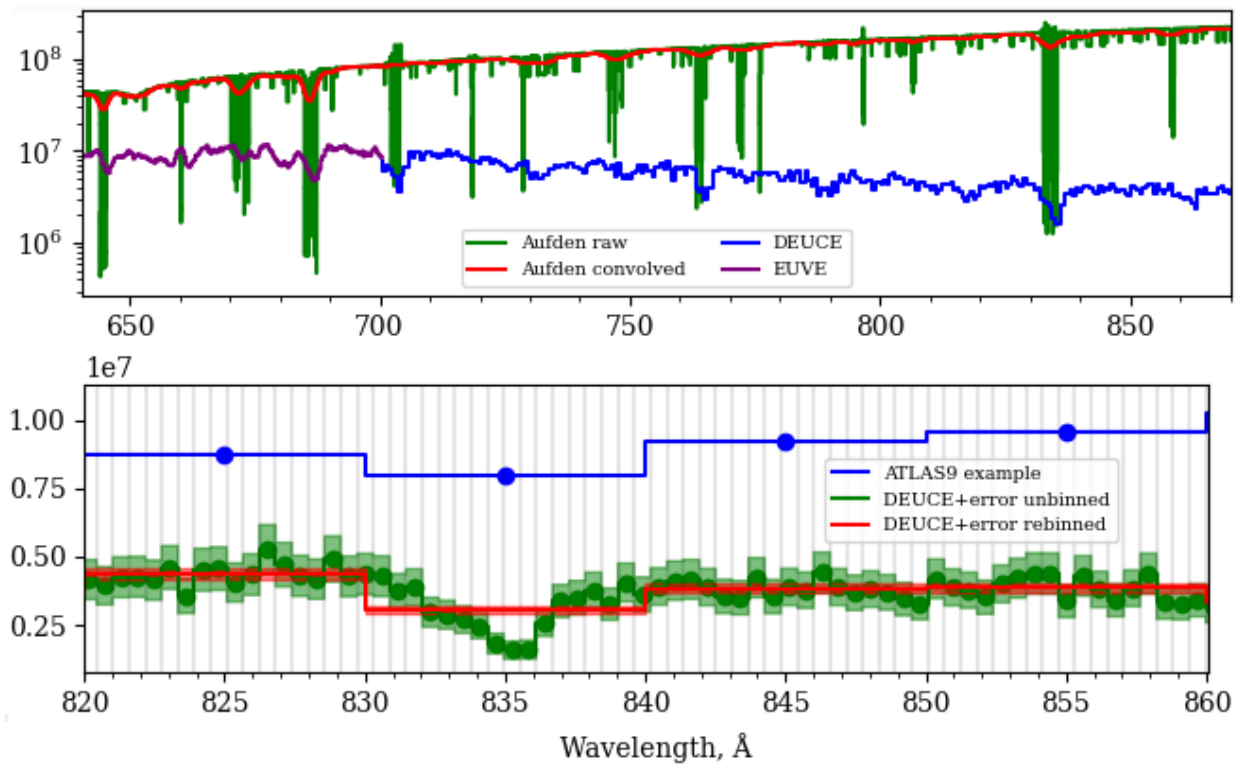

Figure 4.3: The convolution and binning process. Units for both y-axes are surface fluxes in ergs/cm^2/s/Å Top: Convolving and re-sampling the Aufdenberg models to the resolution and spacing of the EUVE and DEUCE observations. Note the different resolution for the EUVE and DEUCE spectral regions. Bottom: Binning the DEUCE observations to the bin size of ATLAS9. Note that the DEUCE bins do not fall cleanly onto the ATLAS9 bins prior to re-sampling. The presented ATLAS9 model has been arbitrarily scaled for clarity of plotting.

4.3 Model fitting parameters

Multiple factors affected the fit between the observations and the stellar models and had to be taken into account during both the EUV and FUV fits.

4.3.1 Fundamental model parameters (T, log g, Z, V_t)

First of all, there were the input parameters of the models themselves, including temperature, surface gravity, metallicity, and turbulent velocity. A T=19,000 K, log g=3 model, for example, will of course predict a substantially different flux than a T=27,000 K, log g=3.5 model. To account for this, the temperature and surface gravity of the models being fit were allowed to vary between

a range of reasonable values (Appendix C) sampled by the pre-published online grids. Instead of fluctuating, the metallicity of all models was constrained to be solar, ($Z/Z_{\odot}$=1) in accordance with recent estimates of [Fe/H]=.01 for Epsilon [57]. Similarly, the turbulent velocity V_t of all models was fixed at 2 km/s, as this is the only possible turbulent velocity for the TLUSTY pre-published online model grids covering the estimated parameter space of Epsilon CMa.

4.3.2 N(H I) column density

Secondly, there was the attenuation of the observed EUV flux due to N(H I) along the sightline to Epsilon CMa. The presence of N(H I) strongly attenuates the sub-912 Å flux of model fits, with higher N(H I) columns allowing hotter and hotter EUV models to be attenuated down to match the level of the EUV observations. The wavelength dependence of this attenuation also imparts a slope to the fitted models, causing stronger attenuation near 911 Å than at lower wavelengths. To account for N(H I) attenuation, continuous absorption as described in Chapter 1 was applied to the models according to a level of N(H I) that was allowed to vary within reasonable values (Appendix D) as part of the fit.

4.3.3 EUV 'scale factor'

Finally, there was the error in the scaling of the DEUCE EUV data to EUVE. Due to the uncertainty present in this scaling (Section 3.3.1), the true DEUCE EUV spectrum may vary within an estimated percentage of its nominal value, which affects the range of EUV model fits that could acceptably describe the observations. As part of the fits, the DEUCE observations were thus allowed to be scaled by a multiplicative free parameter (the "scale factor") within the flux limits set by the 1σ errors of the DEUCE-EUVE flux scaling. A multiplication of the DEUCE fluxes (or a division of the model fluxes) by any value within this limit ensured that the observations were still consistent to the EUVE fluxes while allowing the fitting routine to test if these plausible DEUCE fluxes allowed a better fit to any of the models.

4.3.4 FUV fit parameters

In the FUV, N(H I) attenuation takes the form of interstellar Lyman absorption lines, rather than the strong, continuous absorption it presents in the EUV. Along with interstellar absorption by other species, this effect was ignored; N(H I) did not factor into the FUV model fits. Similarly, as the uncertain DEUCE small-aperture FUV flux was essentially fully tied to the IUE flux to which it was scaled, scale factor was not included in fits of the models to the DEUCE FUV data. Thus, the two parameters allowed to vary for the FUV fits were temperature and surface gravity.

4.3.5 Final parameter space

To reduce computation time, I did not compare *all* of the available models in the model grids with the observations, but instead tested models within a range of reasonable parameters surrounding the best modern estimates of the temperature, surface gravity, and N(H I) column of Epsilon CMa. This final parameter space is shown in Table 4.1. To ensure that this choice of parameter space did not overlook any parameters with fits to the data, a broad, lower resolution χ^2 minimization was performed over a much wider parameter range. This broader fit showed no local minima outside the eventual best fit solutions.

As the Aufdenberg models are individual models, rather than a set of model grids, their EUV fits only varied N(H I) and the scale factor, keeping temperature and surface gravity constant. Furthermore, as they had no FUV predictions above 1000 Å, they were not used for FUV model fits.

Parameter	ATLAS9 Range (Interval)	TLUSTY Range (Interval)	Aufdenberg Range (Interval)
N(H I) $[cm^{-2}]$	$6 \times 10^{16} - 2 \times 10^{18}$ $(.1 \times 10^{16})$	$6 \times 10^{16} - 2 \times 10^{18}$ $(.1 \times 10^{16})$	$6 \times 10^{16} - 2 \times 10^{18}$ $(.1 \times 10^{16})$
Temperature [K]	16,000-30,000 (1000)	16,000-30,000 (1000)	21,750 (–)
Log g [-]	3-4 (.5)	3-4 (.25)	N2: 3.2 (-) N7: 3.5 (-)
Scale factor/1.32 [-]	.74-1.27 (.01)	.74-1.27 (.01)	.74-1.27 (.01)
Metallicity [Z/Z$\odot$]	1	1	1
V_{turb} [km/s]	2	2	2

Table 4.1: The parameter space sampled by the EUV model fitting. The FUV model fitting sampled an identical parameter space, except only temperature and surface gravity were allowed to vary.

4.4 Model fitting procedure

4.4.1 EUV χ^2 minimization

The EUV model fitting procedure occurred as follows. For every combination of temperature, surface gravity, scale factor, and N(H I) column density in the parameter space, a relevant model was loaded. As required, the model was either convolved and sampled to the observations, or the observations binned at the model spacing. The model was then divided by the scale factor parameter and attenuated at every data point according to the N(H I) column density parameter. A χ^2 metric was generated by comparing the attenuated, scaled model to the observations, taking into account the observation error. A reduced χ^2_ν metric was generated using the number of degrees of freedom for each run, which was the number of data points minus the number of free parameters in the fit. There were a total of 4 free parameters for the ATLAS9 and TLUSTY models (N(H I), temperature, log_g, and scale factor) and 2 for the Aufdenberg models (N(H I) and scale factor). Due to the large number of data points in each observational data set, variation of the number of free parameters considered had a small effect on the overall fits. The chi-squared statistic χ^2 and the reduced chi-squared statistic χ^2_ν are formally defined as:

$$\chi^2 \equiv \sum_i \frac{(x_i - \mu_i)^2}{\sigma_i^2} \qquad \chi^2_\nu \equiv \frac{\chi^2}{\nu} \tag{4.2}$$

where x_i, μ_i, and σ_i^2 are the observed fluxes, model values, and observation errors at each wavelength position and ν is the number of degrees of freedom of the fitting.

The χ^2 and χ^2_ν values generated for each model-observation comparison were saved to a database and sorted, with the lowest metric indicating the 'best-fit' model/parameter combination to the observations. This process was repeated for every combination of model (ATLAS9, TLUSTY, Aufdenberg N2, Aufdenberg N7) and EUV observation (DEUCE only, EUVE only, combined DEUCE and EUVE). The best fit parameters and the associated χ^2_ν values for each model-observation combination in the EUV are shown in columns 2-6 of tables Tables 4.2, 4.3, and 4.4.

4.4.2 EUV N(H I) 1D confidence intervals

The error in the DEUCE data precludes a single, authoritative best fit for each stellar parameter, but rather allows for a variety of model fits that each match the observations to within the confidence intervals of the fit. To determine these 1, 2, and 3σ confidence intervals on the N(H I) column to Epsilon CMa, N(H I) was fixed at successive values around the best-fit N(H I) determination and all other parameters were allowed to vary freely in order to find the lowest (best) χ^2 for each value of N(H I) in the sampled parameter space. Using the number of degrees of freedom in the fit, $\Delta\chi^2$ values corresponding to 68.27%, 95%, and 99.73% confidence intervals (1, 2, and 3σ) were calculated and used as χ^2 cutoffs to estimate the limits of the N(H I) determination.

The process of determining confidence intervals is visualized in Figure 4.4, which shows TLUSTY-DEUCE EUV model runs with χ^2 values that fall within the 1, 2, and 3σ $\chi^2_{min} + \Delta\chi^2$ ranges for N(H I). Similar confidence interval plots were generated for all combinations of observations and models are shown in Appendix E.

4.4.3 EUV (T, N(H I)) joint confidence intervals

Joint confidence intervals representing acceptably-fitting model (T, N(H I)) combinations were determined by fixing these two variables at successive locations around their best-fit values and allowing log g and scale factor to vary freely to produce the lowest χ^2 value for each temperature/N(H I) combination. In this way, a series of χ^2 values was generated representing the best-fit solutions for all possible temperature/N(H I) combinations. From this grid, joint intervals of 1, 2, and 3σ confidence for temperature and N(H I) were determined using the same $\Delta\chi^2$ analysis as for the one dimensional confidence intervals, just in two dimensions. Figure 4.5 shows an example of the joint confidence intervals determined using TLUSTY models compared to only the DEUCE data. While this type of joint confidence interval would typically appear as a contour plot, rather than a series of lines, the discrete spacing of the model grid temperatures prevented the generation of a continuous plot. While I could have interpolated the joint confidence intervals between the

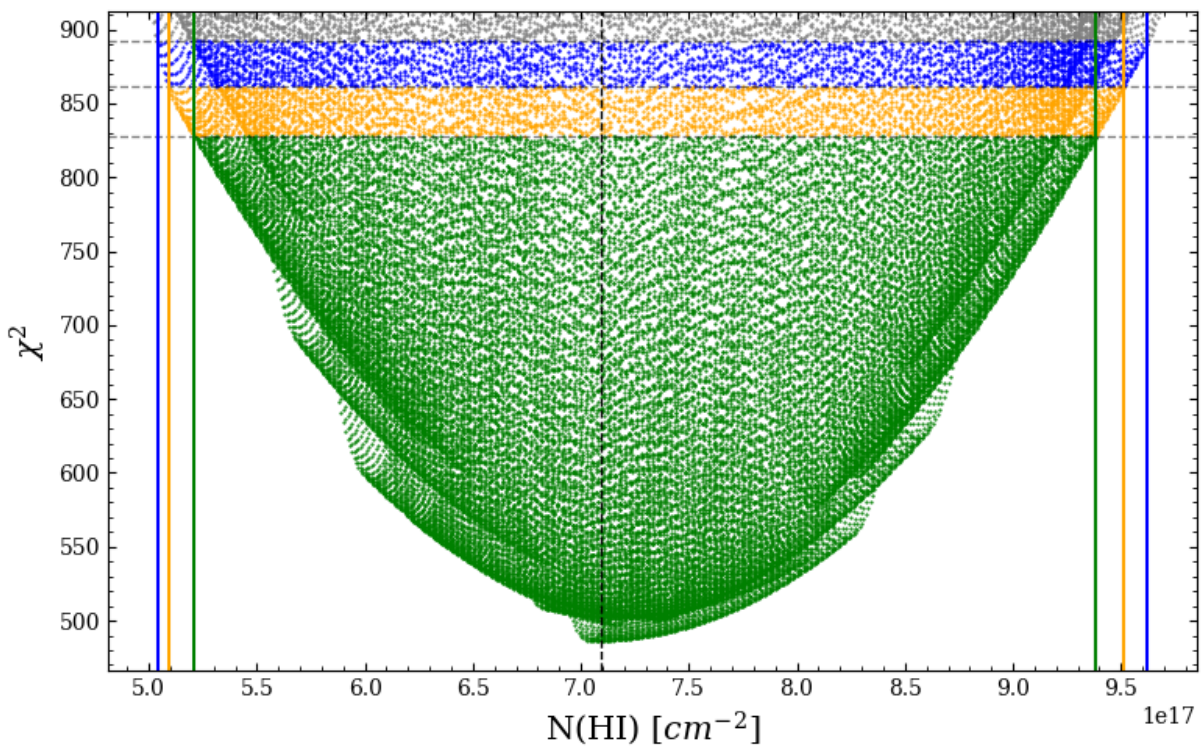

Figure 4.4: An example of the N(H I) and χ^2 value pairs shown for the TLUSTY models compared to the DEUCE data. Each point represents a single model run with a given N(H I), temperature, log g, and scale factor, resulting in a fit with a specific χ^2 value that places the model run in the (N(H I), χ^2) (x,y) plane. Worse fits, with progressively higher χ^2 values, are placed higher and higher on the y-axis, while the best fit represents the minimum of the distribution, indicated by a vertical line. The calculated 1, 2, and 3σ χ^2 cutoffs of $\chi^2_{min} + \Delta\chi^2_{(1,2,3\sigma)}$ are shown by the upper boundaries of the green, yellow, and blue regions (E.g., the 2σ confidence region includes all models with a χ^2 value below that of the upper edge of the yellow region). The vertical green, orange, and blue lines represent the maximum and minimum N(H I) values allowed by each confidence interval. These delimited N(H I) extremes are those quoted in the 1 and 3σ confidence intervals in columns 7-10 of Tables 4.2-4.4. The structure visible in the plot is the result of the superposition of many different models fits as their parameters are slightly varied from run to run, leaving a distinct shape in the N(H I)-χ^2 space. Similar confidence interval plots were generated for all combinations of observations and models are presented in Appendix E.

resolution of the grid, this is only a matter of presentation; all of the (T, N(H I)) information found by the $\Delta\chi^2$ analysis is accurately presented in plots like Figure 4.5.

To further visualize the 2D confidence interval process, a three dimensional plot of the joint confidence intervals is shown in Figure 4.6. This is essentially Figure 4.4 expanded out of the page into a temperature axis, or Figure 4.5 expanded out of the page into a χ^2 axis, allowing the

relationship between temperature, N(H I), and the χ^2 cutoffs to be visualized spatially.

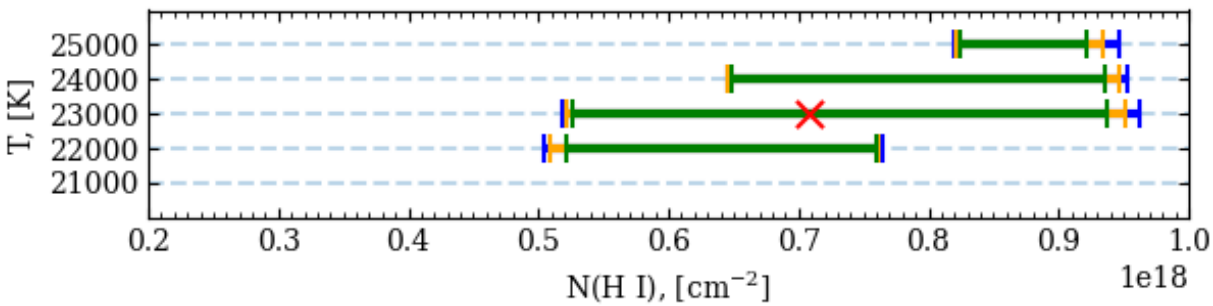

Figure 4.5: An example of the 2D Temperature/N(H I) confidence intervals for the TLUSTY model compared to the DEUCE data. 1, 2, and 3σ confidence regions are shown by green, yellow, and blue error bars, while the best-fit N(H I)/Temperature combination is indicated with a red 'X'. Similar plots for all observation-model combinations are presented in Appendix E.

4.4.4 FUV χ^2 minimization

The FUV χ^2 minimization to find the best model fits was essentially identical to that of the EUV, except that the models were not attenuated by an N(H I) absorption or scaled by the scaling factor, and only ATLAS9 and TLUSTY models were fit, as described in Sections 4.3.4 and 4.3.5.

As the FUV fits did not vary N(H I), no 1D individual N(H I) confidence intervals were generated. The FUV 2D joint confidence intervals were calculated identically to those of the EUV; however, they were based on T and log g, rather than temperature and N(H I), as these were the two parameters allowed to vary during the FUV fitting.

4.4.5 Combined EUV/FUV χ^2 minimization

The fitting process between the models and combined EUV and FUV observations was similar to that described for the individual EUV and FUV observations. For the combined observation fits, however, only the EUV portion of each model was scaled and attenuated. Singular N(H I) and joint (T, N(H I)) confidence intervals for the fits were created identically to those described in the EUV minimization process.

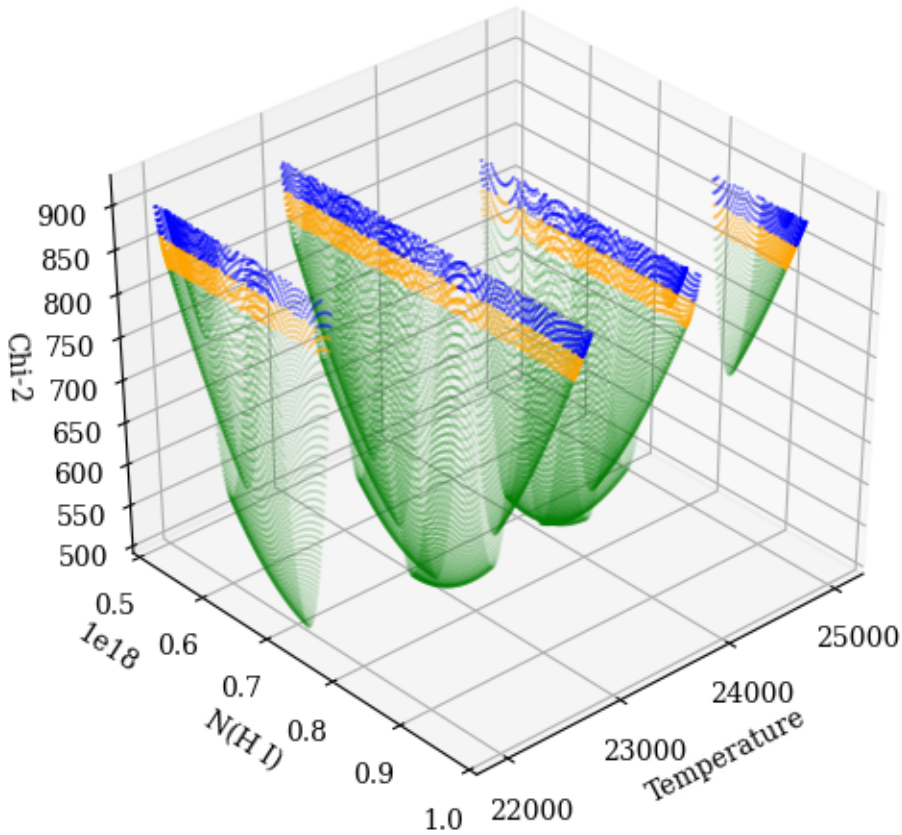

Figure 4.6: A 3D visualization of the joint-confidence intervals for the TLUSTY model compared to the DEUCE data. This is essentially Figure 4.4 expanded into the temperature axis, or Figure 4.5 expanded into the χ^2 axis, simultaneously showing the behavior of the fits with respect to T, N(H I), and χ^2.

4.5 EUV model fitting results

4.5.1 EUV-only 1D confidence Intervals

The best fitting stellar parameters and 1 and 3σ N(H I) individual confidence intervals for every combination of model and EUV observations are presented in Tables 4.2-4.4. The N(H I) ranges estimated for the Epsilon CMa sightline according to each model-observation combination are summarized in Figure 4.7. The best fit N(H I) parameters range from $5.43 - 8.41 \times 10^{17}\ cm^{-2}$, while the 1σ permitted values range from $2.37 - 9.47 \times 10^{17}\ cm^{-2}$. The single best-fit of each model to the DEUCE, EUVE, and combined DEUCE/EUVE observations and their associated χ^2_ν

values are shown in Figures 4.8 and 4.9. For every model-observation combination, 1D N(H I) vs χ^2 confidence intervals are presented in Appendix E.

Model	T (K)	Log g	Scaling	R. χ^2	Best N(H I)	1σ low N(H I)	1σ high N(H I)	3σ low N(H I)	3σ high N(H I)
ATLAS9	24,000	4	1.13	10.76	7.52×10^{17}	7.19×10^{17}	8.12×10^{17}	6.91×10^{17}	8.37×10^{17}
TLUSTY	23,000	3.25	1.23	1.47	7.09×10^{17}	5.21×10^{17}	9.38×10^{17}	5.04×10^{17}	9.62×10^{17}
Aufdenberg N2	21,750	3.2	1.14	1.27	7.26×10^{17}	6.89×10^{17}	8.81×10^{17}	6.86×10^{17}	8.87×10^{17}
Aufdenberg N7	21,750	3.5	1.14	1.21	6.96×10^{17}	6.38×10^{17}	8.33×10^{17}	6.35×10^{17}	8.38×10^{17}

Table 4.2: The best-fitting stellar parameters and N(H I) ranges considering only the DEUCE EUV observations.

Model	T (K)	Log g	Scaling	R. χ^2	Best N(H I)	1σ low N(H I)	1σ high N(H I)	3σ low N(H I)	3σ high N(H I)
ATLAS9	23,000	3	1.21	8.92	6.82×10^{17}	6.47×10^{17}	7.58×10^{17}	6.39×10^{17}	7.89×10^{17}
TLUSTY	23,000	3.25	1.26	1.11	5.43×10^{17}	2.37×10^{17}	9.47×10^{17}	2.09×10^{17}	9.75×10^{17}
Aufdenberg N2	21,750	3.2	1.18	1.07	5.95×10^{17}	4.63×10^{17}	9.31×10^{17}	4.58×10^{17}	9.43×10^{17}
Aufdenberg N7	21,750	3.5	.81	1.06	6.36×10^{17}	3.60×10^{17}	8.16×10^{17}	3.54×10^{17}	8.27×10^{17}

Table 4.3: The best-fitting stellar model parameters and N(H I) ranges considering only the EUVE EUV observations.

Model	T (K)	Log g	Scaling	R. χ^2	Best N(H I)	1σ low N(H I)	1σ high N(H I)	3σ low N(H I)	3σ high N(H I)
ATLAS9	23,000	3	.92	14.44	8.41×10^{17}	8.07×10^{17}	8.75×10^{17}	7.98×10^{17}	8.84×10^{17}
TLUSTY	23,000	3.25	.83	1.57	7.87×10^{17}	6.33×10^{17}	9.15×10^{17}	6.28×10^{17}	9.24×10^{17}
Aufdenberg N2	21,750	3.2	.82	1.48	8.13×10^{17}	6.65×10^{17}	9.15×10^{17}	6.62×10^{17}	9.19×10^{17}
Aufdenberg N7	21,750	3.5	.74	1.59	7.76×10^{17}	6.48×10^{17}	8.48×10^{17}	6.39×10^{17}	8.53×10^{17}

Table 4.4: The best-fitting stellar model parameters and N(H I) ranges considering both the DEUCE and EUVE EUV observations.

4.5.2 EUV-only 2D confidence intervals

The results of the 2D joint (N(H I),T) confidence interval fitting for comparisons between the models and EUV observations are presented in Table 4.5. The permitted temperatures range from 22-25,000 K, and the permitted N(H I) intervals range between $2.09 - 9.75 \times 10^{17}$ cm^{-2}, although the specific range depends on the model temperature considered. For every model-observation combination, 2D N(H I,T) confidence interval plots are presented in Appendix E.

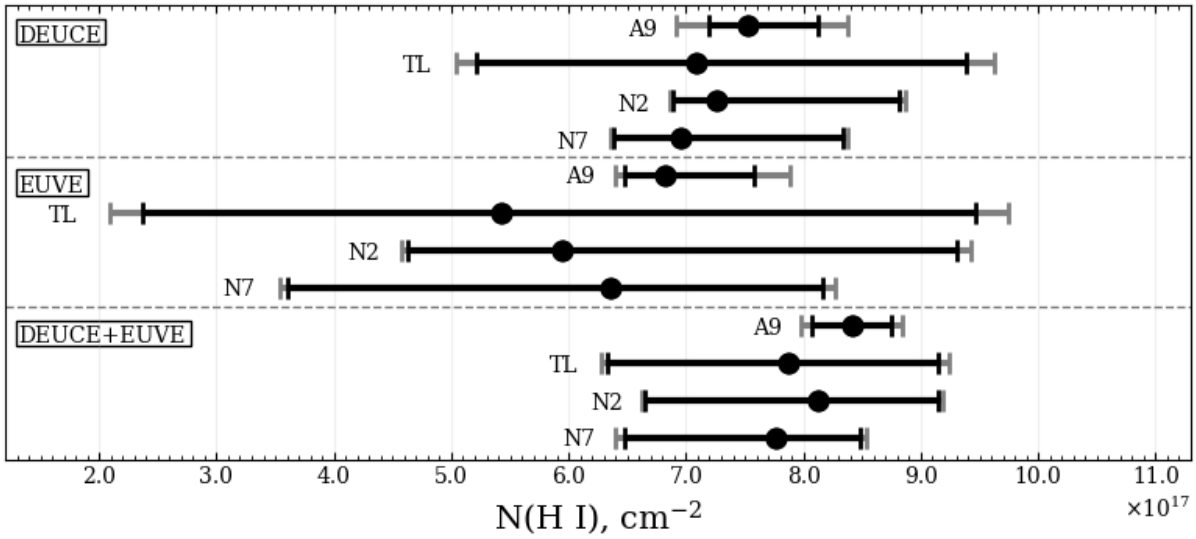

Figure 4.7: The N(H I) ranges to Epsilon CMa generated by the 1D confidence interval $\Delta\chi^2$ analysis of the model fits. The best fit values, along with 1σ (black) and 3σ (grey) limits are shown.

Model	Observation	22,000 low	22,000 high	23,000 low	23,000 high	24,000 low	24,000 high	25,000 low	25,000 high
ATLAS9	DEUCE	7.01	7.2	6.91	8.02	7.16	8.37	-	-
ATLAS9	EUVE	-	-	6.39	7.89	-	-	-	-
ATLAS9	EUVE/DEUCE	-	-	7.98	8.84	8.09	8.40	-	-
TLUSTY	DEUCE	5.04	7.64	5.18	9.62	6.45	9.53	8.19	9.46
TLUSTY	EUVE	2.34	6.49	2.09	9.75	4.04	9.19	-	-
TLUSTY	EUVE/DEUCE	6.72	7.2	6.41	9.24	6.28	9.15	-	-

Table 4.5: A summary of the 2D 3σ joint confidence intervals in N(H I) vs T permitted by the EUV fitting. All table values are N(H I) values in units of 10^{17} cm^{-2}. The 3σ low and high N(H I) value permitted for each temperature are presented for each model/observations combination. If a temperature is not presented or left blank, it was not a permitted solution under the fit. The 2D joint interval plots from which these values were taken are presented in Appendix E.

4.5.3 EUV model fitting discussion

4.5.3.1 ATLAS9 EUV fits

As seen in Tables 4.2-4.4, all of the best ATLAS9 fits to the EUV data have very high χ^2_ν values (∼9-15). These high values are indicative of the stringency of the χ^2 fits after the observations are binned to the ATLAS9 resolution and have their error reduced significantly. As shown in Figure 4.8, these best-fit models clearly need improvement and do not always match the general shape and predicted features of the EUV observations. Nonetheless, these best fit models match the EUV

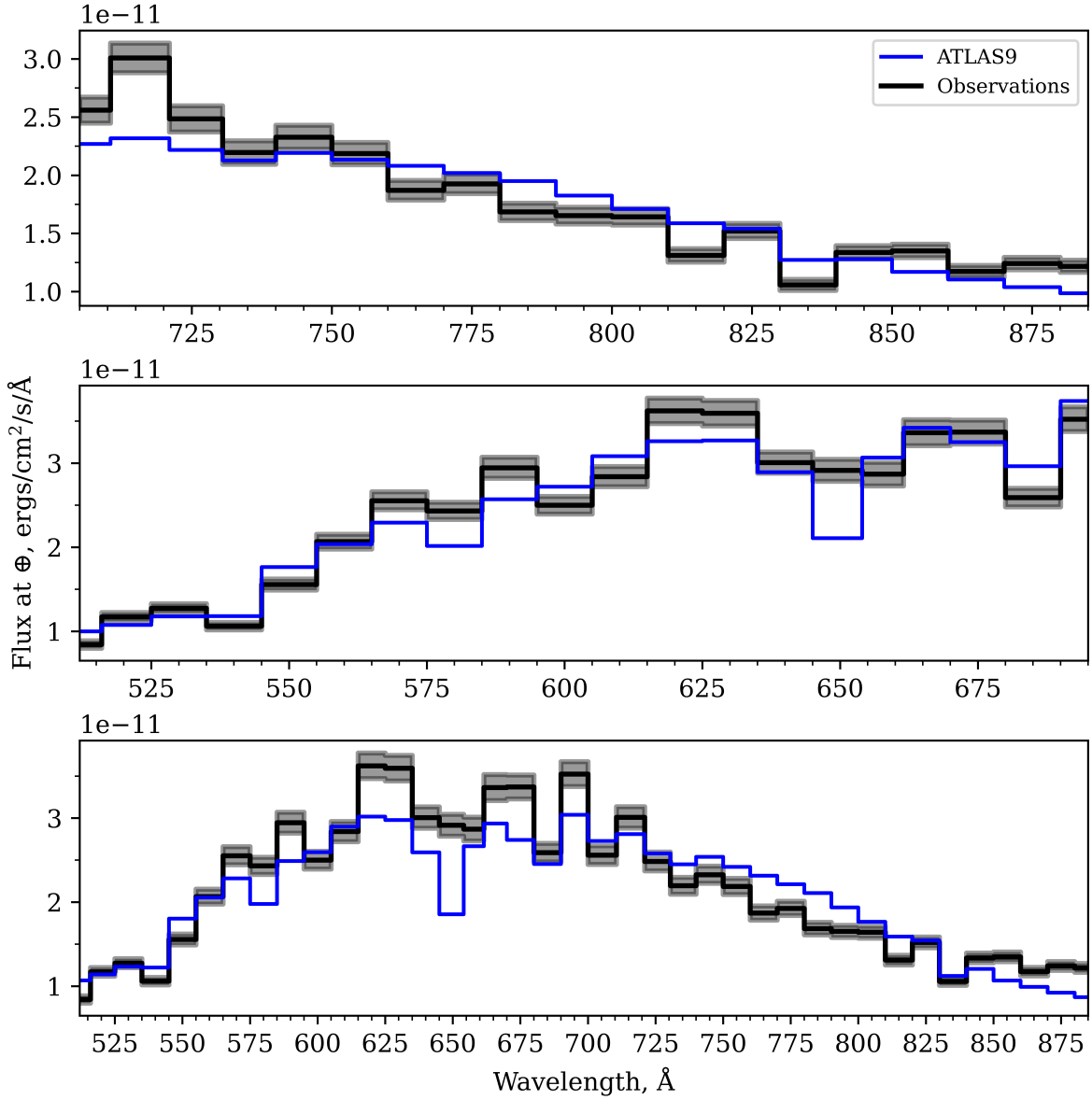

Figure 4.8: The best ATLAS9 fits to observations, generated using the best-fit parameters and N(H I) columns listed in Table 4.2. The observations are presented in the binned, resampled state in which they were compared to the ATLAS9 models. Top: Fits to the DEUCE observations only. Middle: Best model fits to the EUVE observations only. Bottom: Best model fits to the combined DEUCE and EUVE observations. The χ^2_ν values of the ATLAS9 models from top to bottom are: [10.76,8.92,14.44].

flux of the observations to within a factor of 2 at all wavelengths, and often better. The best fit and 1 and 3σ permitted stellar parameters and N(H I) sightlines predicted by the singular and 2D confidence intervals are reasonable, and fall within observational estimates of these parameters

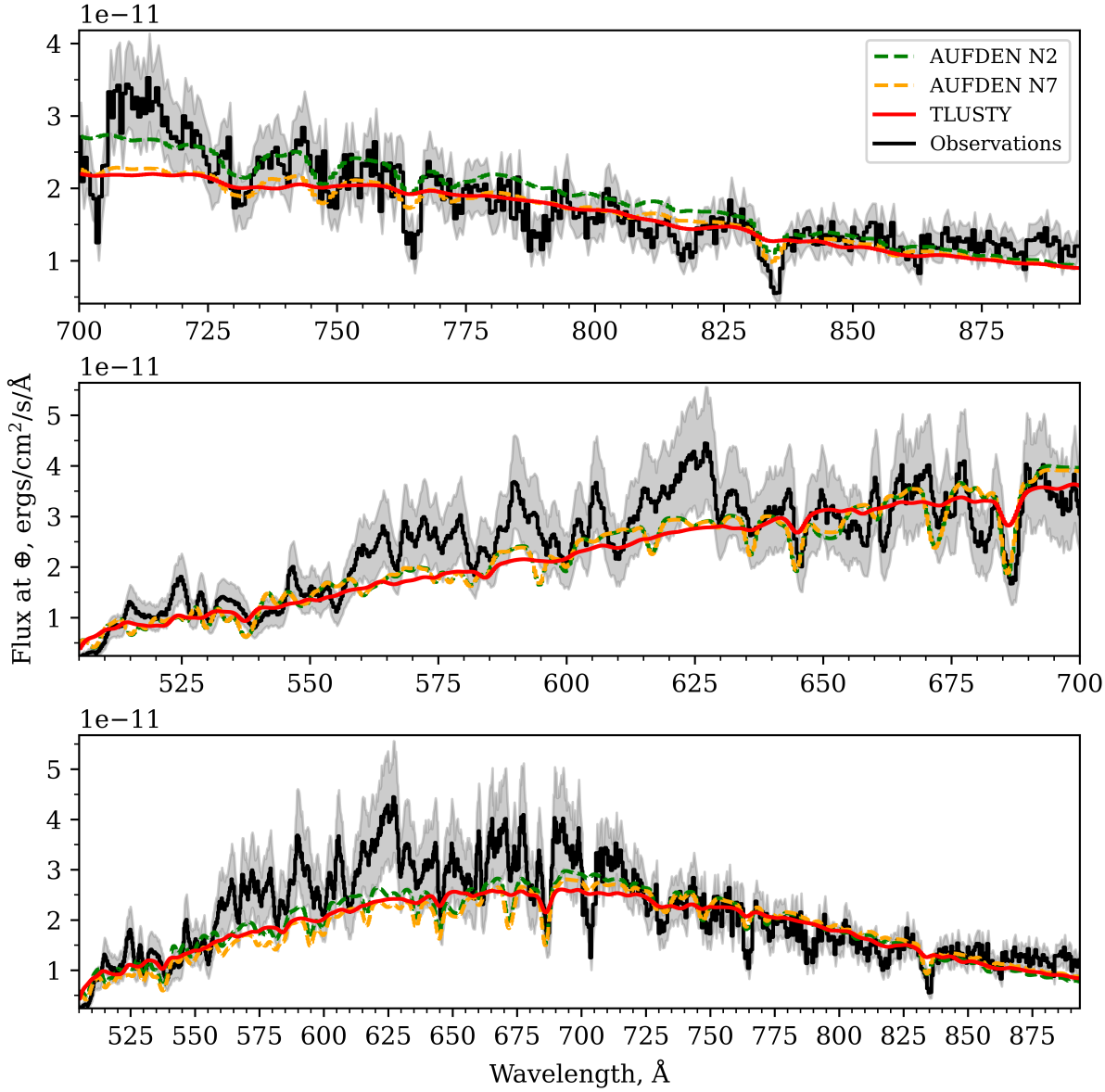

Figure 4.9: The best TLUSTY and Aufdenberg N2/N7 fits to observations, generated using the best-fit parameters and N(H I) columns listed in Table 4.2. The models are convolved to the resolution of the observations. Top: Fits to the DEUCE observations only. Middle: Best model fits to the EUVE observations only. Bottom: Best model fits to the combined DEUCE and EUVE observations. The χ^2_ν values of the TLUSTY models from top to bottom are: [1.47,1.11,1.57]. The χ^2_ν values of the Aufdenberg N2 models from top to bottom are: [1.27,1.07,1.48]. The χ^2_ν values of the Aufdenberg N7 models from top to bottom are: [1.21,1.06,1.59].

for Epsilon CMa (Appendix C). Although the best-fit ATLAS9-DEUCE comparison predicts a surface gravity of 4, this is still barely within the range of the published estimates, considering

that the ATLAS9 models only step by .5. Furthermore, the full 2D confidence intervals for the ATLAS9-DEUCE fittings allow for a surface gravity of 3 and 3.5 at reasonable N(H I) values and temperatures.

4.5.3.2 TLUSTY EUV fits

Unlike the ATLAS9 fits, the TLUSTY EUV fits shown in Figure 4.9 all have χ^2_ν values between 1.11 and 1.57, which indicates a good fit between the models and observations. The EUV best-fit models universally predict a temperature of 23,000 K and a surface gravity of 3.25, which is in line with the most modern estimates of these parameters, considering the .25 log g parameter step size of the TLUSTY models. The 2D confidence intervals similarly predict a reasonable T=22,000-25,000 K and N(H I)=$2.34 - 9.75 \times 10^{17}\ cm^{-2}$. The models clearly fail to predict many of the spectral features of the observations and undoubtedly need refinement in this respect. However, like the ATLAS9 models, they match the flux of the EUV observations to within a factor of 2-3 at all wavelengths, and often better.

4.5.3.3 Aufdenberg EUV fits

Like the TLUSTY fits, the Aufdenberg N2 and N7 EUV fits all have χ^2_ν values between 1.06 and 1.59, indicating good fits to the observations. While the main stellar parameters for the models are fixed, they predict a reasonable range of N(H I) in their 1 and 2D confidence intervals. The Aufdenberg models do a noticeably better job at predicting the location and strength of spectral features than ATLAS9 or TLUSTY, but still miss many lines and the broader structure of the observations (which itself comes from a multitude of spectral lines blanketing one another [17]). Like the other models, however, they correctly predict the overall EUV flux of the observations to within a factor of 2-3 and often better.

4.5.3.4 General EUV fitting comments

None of the models fit the bump in the DEUCE spectrum from 700-725 Å well, and this accounts for some of the errors in the fits. Similarly, the models do a poor job of predicting much of the structure in the EUVE observations. In the combined EUVE-DEUCE fits, it is also apparent that the TLUSTY and Aufdenberg models are more closely fitting the DEUCE data at the expense of the EUVE data. This could indicate that the DEUCE data was scaled to EUVE incorrectly, or simply that the models are unable to match the full spectrum correctly, and need refinement.

4.5.3.5 An observational EUV excess above 860 Å?

At first glance, Figures 4.8 and 4.9 might seem to indicate that all models underpredict the flux of Epsilon CMa from approximately 860 Å to the edge of the DEUCE bandpass, which is the most highly ionizing part of the DEUCE spectrum. It must be noted, however, that these plots show only the single best-fit models to the observations. In reality, all the models within the 1 or 3σ 2D joint confidence intervals are equally acceptable fits to the observations and must be considered viable possibilities. If these 3σ models are all plotted together, as shown in Figure 4.10, it becomes apparent that plausible models exist that both over and under-predict the DEUCE flux above 860 Å, at the expense or benefit of other regions of the spectrum. As all of these models are viable fits, there cannot be definitively said to be a flux excess of the observations over the models above 860 Å.

4.6 FUV model fitting results

4.6.1 FUV-only 2D confidence Intervals

The results of the 2D joint (T, log g) confidence interval fitting for comparisons between the ATLAS9/TLUSTY models and the DEUCE FUV observations are presented in Table 4.6, with each model's best fit indicated. The three items in the table represent the only (T, log g) parameter combinations out of the full parameter space that were acceptable fits to the DEUCE data. The

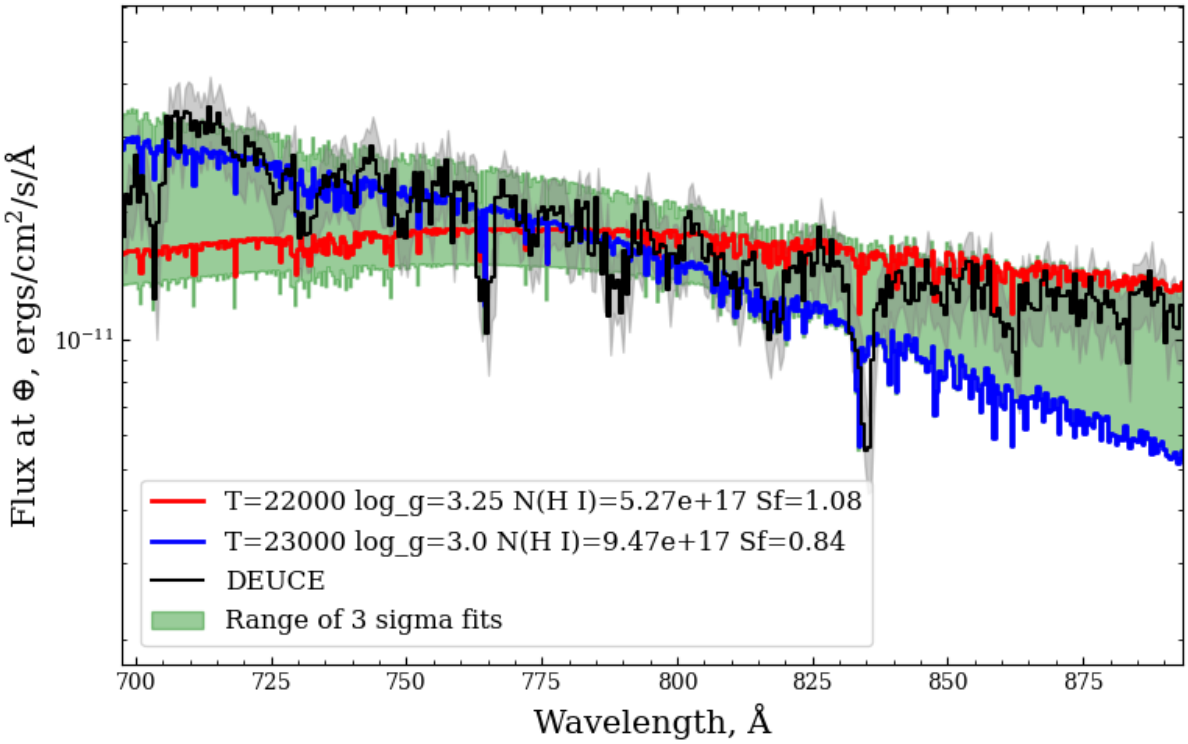

Figure 4.10: The 3σ accepted model fits to the DEUCE data that had the highest and lowest values at 894 Å, and the range of values covered by all 3σ acceptable models. While the best-fit TLUSTY model (Figure 4.9, top) under-predicts the flux at the high end of DEUCE's bandpass, the 3σ fits encompass essentially all values of the DEUCE observations. A similar situation occurs for the ATLAS9 and Aufdenberg models. The TLUSTY models shown here are in native spacing and resolution.

two best fits are shown in Figure 4.11, along with their respective χ^2_ν values.

Model	T (K)	Log g	R. χ^2	Notes
ATLAS9	22,000	3	66.13	Best ATLAS9 FUV fit
TLUSTY	21,000	3	3.14	Best TLUSTY FUV fit
TLUSTY	21,000	3.25	3.67	Second possible TLUSTY FUV fit

Table 4.6: All 3σ permitted stellar model parameters found when comparing the models to only the DEUCE FUV data.

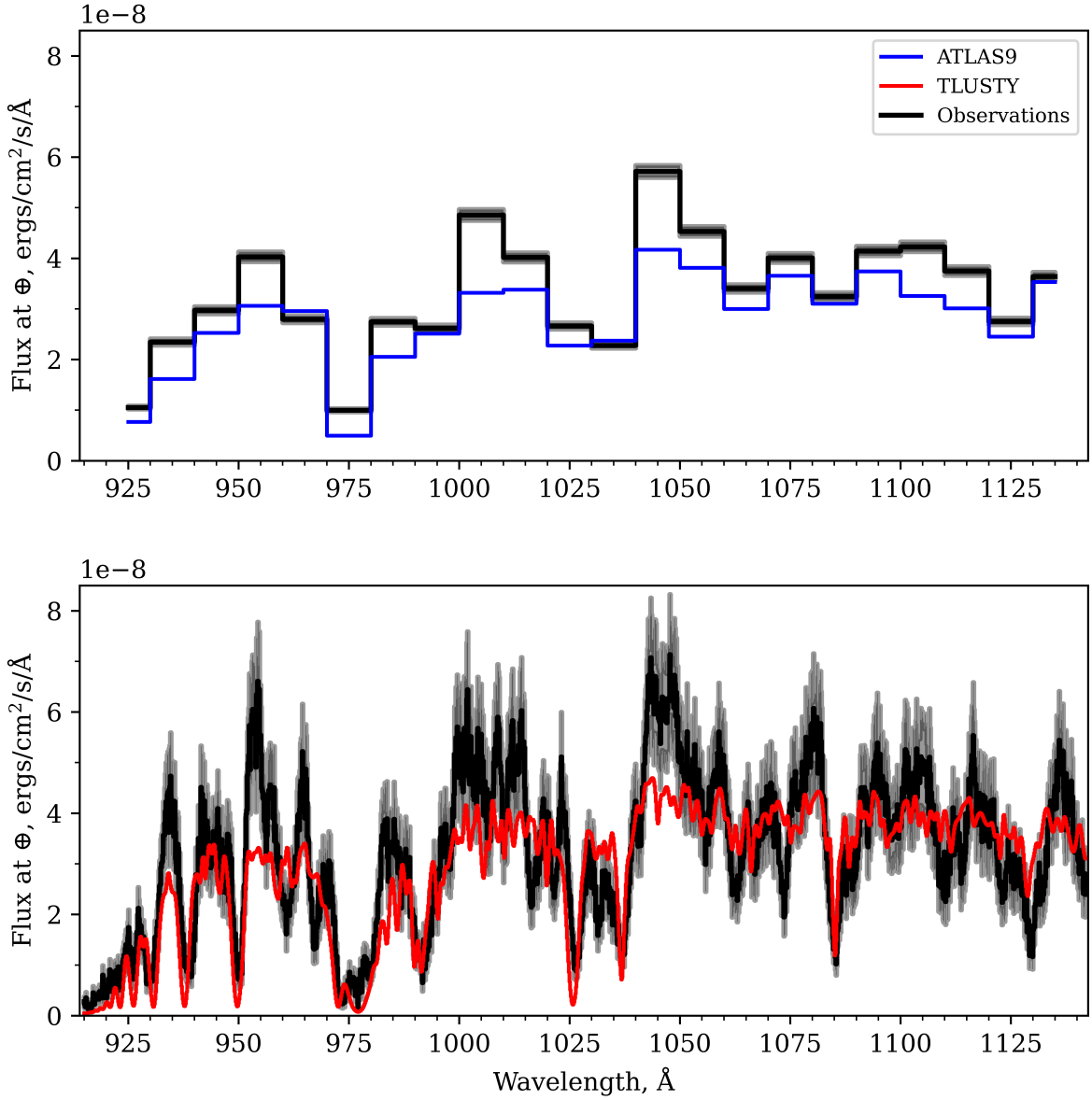

Figure 4.11: The best-fit ATLAS9 and TLUSTY fits to the DEUCE FUV, generated using the parameters shown in Table 4.6. The ATLAS9 fit has a χ^2_ν of 66.13, and the TLUSTY fit has a χ^2_ν of 3.14.

4.6.2 FUV-only model fitting discussion

4.6.2.1 General FUV Fitting Comments

As shown in Table 4.6, the FUV-only model fits only allow for a temperature of 21,000-22,000 K and a surface gravity between 3 and 3.25. These values are closer to those traditionally estimated

for Epsilon (e.g as used by [10]). The permitted ATLAS9 fit, like in the EUV, has an extremely high χ^2_ν due to the small error of the binned observations. However, even the TLUSTY best fits are not 'good' fits, with χ^2_ν values between 3 and 4. Both models clearly fail to correctly match many of the line strengths and the full shape of the spectrum, although the TLUSTY spectrum comes closer. Regardless, both best fits match the flux of the observations to within a factor of 2-3 at all points.

4.6.2.2 EUV-FUV fit discrepancy

It is noteworthy that there is almost no overlap between the permitted temperatures and surface gravities found by the FUV fits (Table 4.6) and the EUV fits (Table 4.5). The TLUSTY FUV fits all predict a temperature of 21,000 K, which is completely precluded by the EUV fits, while the ATLAS9 FUV fits do overlap with the EUV fits at a temperature of 22,000 K and surface gravity of 3 over a small N(H I) region from $7.01 - 7.2 \times 10^{17}\ cm^{-2}$. In general, it can be seen that the FUV fits cluster around a cooler temperature, while the EUV fits predict a wider and hotter range of temperatures. The fact that no one set of model parameters provides a fit to all the observations points to the inability of the models to correctly predict the EUV and FUV of Epsilon CMa simultaneously. This deficiency in the EUV/FUV model fits to Epsilon CMa has been noted by many previous studies [10] [2], and I confirm its continued existence even with more modern models like TLUSTY.

4.7 Simultaneous EUV and FUV model fitting results

4.7.1 Simultaneous EUV and FUV 1D confidence Intervals

The best fitting stellar parameters and 1 and 3σ N(H I) individual confidence intervals for every combination of ATLAS9/TLUSTY model and the combined EUV and FUV observations are presented in Tables 4.7-4.9. The single best-fit of each model to the DEUCE, EUVE, and combined DEUCE/EUVE observations are plotted in Figures 4.12 and 4.13.

Model	T (K)	Log g	Scaling	R. χ^2	Best N(H I)	1σ low N(H I)	1σ high N(H I)	3σ low N(H I)	3σ high N(H I)
ATLAS9	22,000	3	1.13	27.24	6.24×10^{17}	6.10×10^{17}	6.40×10^{17}	6.06×10^{17}	6.44×10^{17}
TLUSTY	22,000	3	1.26	2.94	6.03×10^{17}	3.07×10^{17}	7.28×10^{17}	3.00×10^{17}	7.35×10^{17}

Table 4.7: The best-fitting stellar model parameters and N(H I) ranges considering the DEUCE EUV and DEUCE FUV data.

Model	T (K)	Log g	Scaling	R. χ^2	Best N(H I)	1σ low N(H I)	1σ high N(H I)	3σ low N(H I)	3σ high N(H I)
ATLAS9	22,000	3	1.11	50.25	3.06×10^{17}	2.76×10^{17}	3.36×10^{17}	2.69×10^{17}	3.44×10^{17}
TLUSTY	22,000	3	1.26	2.76	3.02×10^{17}	6.00×10^{16}	5.89×10^{17}	6.00×10^{16}	6.03×10^{17}

Table 4.8: The best-fitting stellar model parameters and N(H I) ranges considering the EUVE EUV and DEUCE FUV data.

Model	T (K)	Log g	Scaling	R. χ^2	Best N(H I)	1σ low N(H I)	1σ high N(H I)	3σ low N(H I)	3σ high N(H I)
ATLAS9	23,000	3	1.26	51.25	7.60×10^{17}	7.46×10^{17}	7.76×10^{17}	7.43×10^{17}	7.79×10^{17}
TLUSTY	22,000	3	1.26	3.53	5.81×10^{17}	4.73×10^{17}	7.05×10^{17}	4.65×10^{17}	7.10×10^{17}

Table 4.9: The best-fitting stellar model parameters and N(H I) ranges considering the combined EUV/DEUCE EUV and DEUCE FUV data.

4.7.2 Simultaneous EUV and FUV 2D confidence intervals

The results of the 2D joint confidence interval fitting in N(H I) vs T for comparisons between the ATLAS9/TLUSTY models and the combined EUV and FUV observations are presented in Table 4.10. The permitted temperatures range from 20,000-23,000 K, and the permitted N(H I) intervals range between 6×10^{16} cm^{-2}, the lower limit of the tested parameter space, and 7.79×10^{17} cm^{-2}, depending on the model temperature considered.

Model	Observation	20,000 low	20,000 high	21,000 low	21,000 high	22,000 low	22,000 high	23,000 low	23,000 high
ATLAS9	DEUCE	-	-	-	-	6.06	6.44	-	-
ATLAS9	EUVE	-	-	-	-	2.69	3.44	-	-
ATLAS9	EUVE/DEUCE	-	-	-	-	-	-	7.44	7.79
TLUSTY	DEUCE	3.00	4.02	3.32	5.72	4.40	7.35	-	-
TLUSTY	EUVE	-	-	.6	1.31	.6	6.03	-	-
TLUSTY	EUVE/DEUCE	-	-	-	-	4.65	7.10	-	-

Table 4.10: A summary of the 2D 3σ joint confidence intervals in N(H I) vs T permitted by the simultaneous EUV/FUV fitting. All table values are N(H I) values in units of 10^{17} cm^{-2}. The 3σ low and high N(H I) value permitted for each temperature are presented for each model/observations combination. If a temperature is not presented or left blank, it was not a permitted solution under the fit.

4.7.3 Simultaneous EUV and FUV model fitting discussion

4.7.3.1 General fitting comments

The models permitted by the simultaneous EUV and FUV fitting all have a temperature between 20,000-23,000 K, with all of the model-observation combinations save one permitting a temperature of 22,000 K. The N(H I) ranges permitted by these fits are all within observational estimates except for the TLUSTY-EUVE combination, which allows an N(H I) as low as the lower limit of the parameter space sampled by the model fits, 6.00×10^{16} cm^{-2}.

There are no parameter combinations that provide acceptable fits to the EUV, FUV, and simultaneous EUV/FUV observations all at once. However, there is overlap between the EUV and simultaneous EUV/FUV acceptable parameters for all of the TLUSTY fits, with each allowing for a temperature of 22,000 K in overlapping N(H I) and log g ranges. There is further overlap

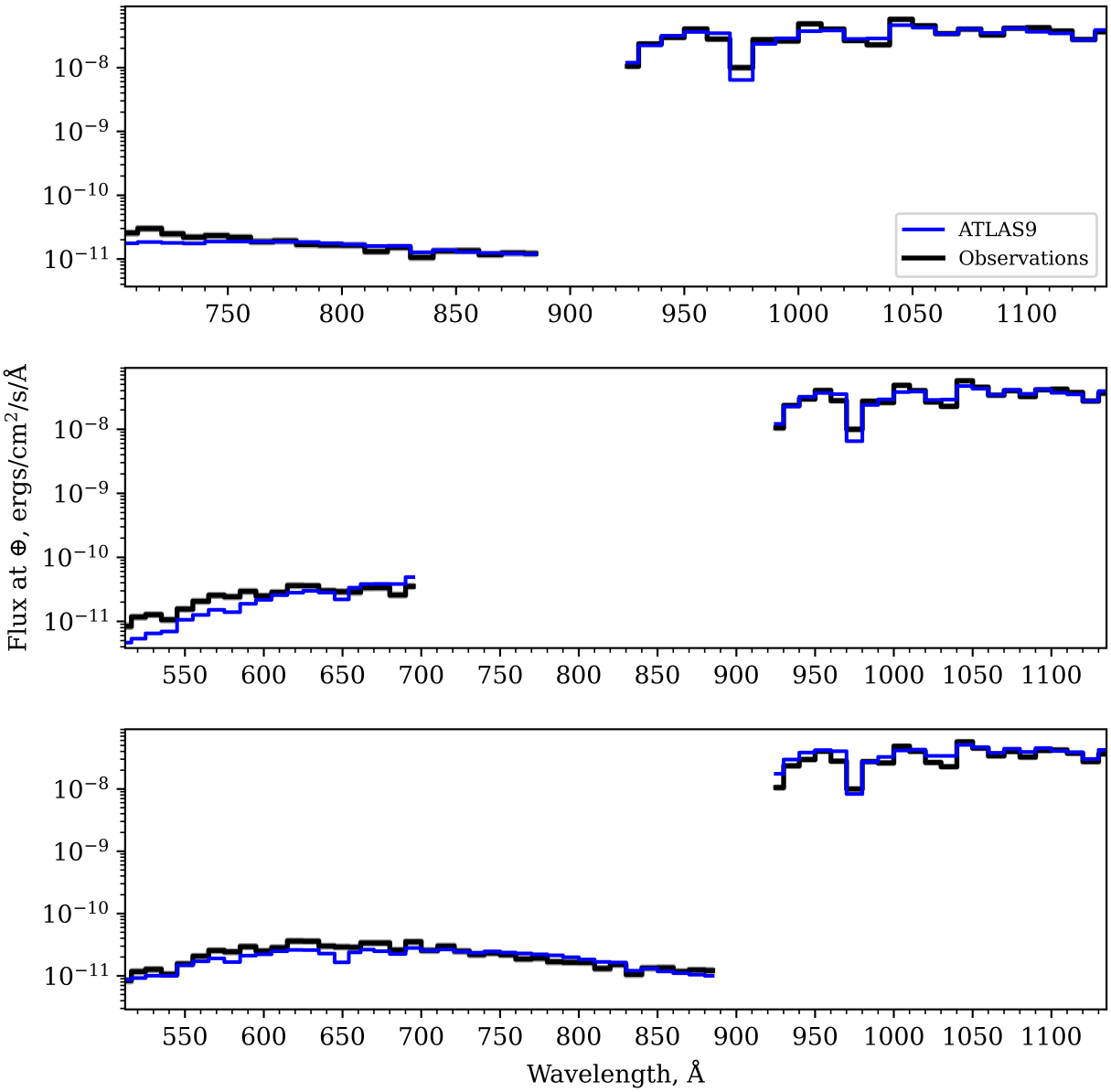

Figure 4.12: The best fit ATLAS9 combined EUV/FUV plots for DEUCE, EUVE, and combined DEUCE EUVE, along with the DEUCE FUV, generated using the model parameters in Tables 4.7, 4.8, and 4.9. The χ^2_ν values for the plots from top to bottom are 27.24, 50.25, and 51.25.

between the FUV-only and simultaneous EUV/FUV fits for the ATLAS9-DEUCE fits, permitting a temperature of 22,000 K and surface gravity of 3.

The fits have χ^2_ν values in Tables 4.7-4.9 that fall squarely in between those in Tables 4.2-4.4 (EUV only) and those in Table 4.6 (FUV only) for the same model-observation combination. As the χ^2_ν values for the simultaneous EUV/FUV fits are higher than those for the EUV-only fits and

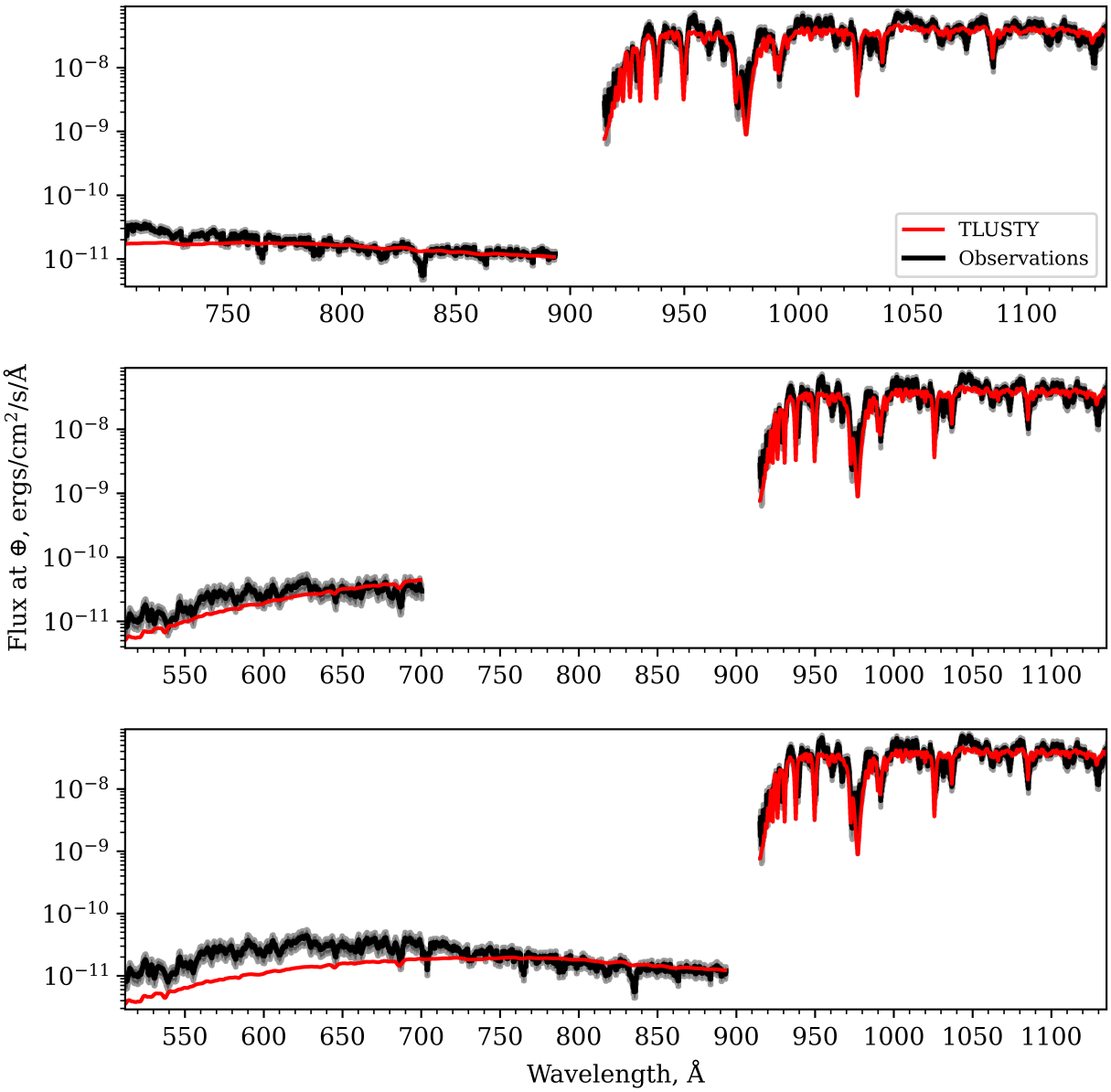

Figure 4.13: The best fit TLUSTY combined EUV/FUV plots for DEUCE, EUVE, and combined DEUCE EUVE, along with the DEUCE FUV, generated using the model parameters in Tables 4.7, 4.8, and 4.9. The χ^2_ν values for the plots from top to bottom are 2.94, 2.76, and 3.53.

lower than those for the FUV-only fits, the simultaneous fits appear to be simply merging the two previous fits together and finding a compromise solution that isn't a particularly great fit for either the EUV or the FUV, while minimizing the error in the overall fit.

I do not consider these 'compromise' fits to be indicative of a true, physically compelling single best set of parameters that well-represents both the EUV and FUV portion of the observations

simultaneously. Nonetheless, these models represent the best available fits to the combined EUVE, DEUCE EUV, and DEUCE FUV data. Even if the models used to generate this fit clearly require refinement to their underlying physics to better match the EUV and FUV fluxes simultaneously without resorting to a compromise solution, these simultaneous EUV/FUV best-fit models still match the EUV spectra to within a factor of 3 at all points (e.g the 512-600 Å region of the TLUSTY-EUVE/DEUCE fit in the bottom of Figure 4.13).

4.8 Summary and improvements

4.8.1 Summary

As outlined in Appendix C, the historically estimated temperature of Epsilon CMa ranges from 21,000-25,000 K, and the most modern estimates cluster around 22,000-23,000 K. Its estimated surface gravity, including the most modern estimates, ranges from 3-3.8. The estimated N(H I) sightline to Epsilon is estimated to be $7 - 11 \times 10^{17}\ cm^{-2}$ from EUVE observations and $< 5, < 2$ and $4.8 - 11 \times 10^{17}\ cm^{-2}$ from optical studies.

The 1σ parameter intervals generated from the ATLAS9 and TLUSTY 2D joint confidence intervals for the EUV model fits all fall within these ranges, and the best fits cluster around T=23,000 K, N(H I) $5 - 8 \times 10^{17}\ cm^{-2}$, in strong accordance with the most modern estimates of its temperature and sightline column density. The best-fitting Aufdenberg models to the EUV observations, at a fixed T=21,750 K, also have reasonable best-fit and 1σ N(H I) intervals. The TLUSTY and Aufdenberg best-fit models furthermore have χ^2_ν values that indicate that they are good overall fits to the observations at these best-fit parameters.

The models, especially ATLAS9, clearly need improvement to better predict specific spectral features and the overall shape of the observations in both the EUV and the FUV. Furthermore, the previously noted inability of the models to simultaneously predict the EUV and FUV flux of Epsilon CMa continues to hold true, even with more modern models like TLUSTY. Even with these limitations, however, all of the best-fit EUV and simultaneous EUV/FUV models correctly predict

the EUV flux of Epsilon CMa to within a factor of 3 at all points, and generally much better, while simultaneously predicting reasonable parameters for its temperature, surface gravity, and N(H I) column.

In light of the general and reasonable agreement of the fits to the EUV observations of both DEUCE and EUVE, there is insufficient evidence to conclude that there is a significant ($\sim 10-20\times$) *flux discrepancy between the current best model predictions for Epsilon CMa and the observations in the EUV.* Unless observational estimates of the parameters of Epsilon CMa change and preclude the hotter temperatures preferred by the EUV and simultaneous EUV/FUV fits, stellar models at these temperatures do a sufficient job of predicting the ionizing flux outputs of B-type stars, and there is currently no need to re-assess the roles of these stars as generally minor contributors to large-scale ionization in the Universe.

4.8.2 Limitations and potential improvements

There are multiply fronts on which the presented analysis and the underlying data and models could be improved or refined.

4.8.2.1 Observational error

One area for improvement is in the observational error, which is perhaps the strongest limitation to the model fits, as error in the observations directly translates into a wider range of model parameters that can acceptably fit the models within that error. The error present in the angular diameter determination of Epsilon, the flux calibration of DEUCE, and the EUV background of the spectrum all permit "looser" fits, allowing bad models to "hide" in the noise; with sufficient observational error, even a truly poor model might register a χ^2_ν value of close to 1 and be considered an adequate fit to the data. When this error is reduced, models must correctly match these cleaner observations, and the model-observation fits become more discerning.

Improvement in the observational error comes from reducing each contribution to that error in the final flux-calibrated observations. Improvements in the angular diameter determination

and subsequent distance scaling are limited by new observations with improved instruments and techniques. Improvements in the flux calibration largely come down to laboratory constraints, such as lower detector noise in the MCP in the square tank, or more time devoted to repeat measurements and whittling down the measurement error. Error from the background could be improved by an even lower scattering grating, or perhaps by a true simulation or physical testing of scatter inside the payload and subsequently improved baffling. Although these are certainly possibilities, the funding and scope of a rocket mission often precludes the hardware, time, and resources available for such a precise measurement.

The ultimate solution to improving the fundamental signal to noise of the observations is of course a longer exposure, which enters the domain of satellite observations, or multiple time-consuming rocket flights. As the EUV bandpass is relatively devoid of targets due to its heavy N(H I) attenuation, new satellites are not common, and Epsilon CMa will likely be excluded from observation by any new satellites due to bright object limits, as was the case with GAIA. As the spectrum of Epsilon CMa obtained by DEUCE is high quality and answers the science question of the mission, approval of a future, repeat rocket or cubesat is highly unlikely. Thus, improving signal to noise by significantly increasing observing time does not have good future prospects.

4.8.2.2 Low resolution

A second, parallel limitation to the fits comes from the low resolution of the DEUCE instrument, which precluded the resolving of many of the absorption lines present in the EUV. While only a few lines appear to be present in the spectrum, these are most likely line-complexes rather than individual lines; higher resolution observations such as UVSTAR and ORFEUS reported observing so many lines that individual identification was difficult, and that the true continuum was likely never seen [42, 17]. This inability to observe the continuum even at higher resolution undoubtedly means that DEUCE is actually observing a multitude of lines in low resolution, which spreads out their absorption and lowers the flux compared to the true continuum level set by N(H I) attenuation. This likely results in an over estimation of the N(H I) values to Epsilon, although

the magnitude of this effect is impossible to estimate. Even on a general scale, a higher-resolution DEUCE spectrum would allow for a keener understanding of exactly what features the models are correctly or incorrectly predicting, and would help refine their underlying physics and allow for a more accurate fit to the observations.

The constraints imposed by the low resolution observation of DEUCE were impossible to resolve for a sounding rocket observation with limited observing time. DEUCE was designed with a large EUV aperture to maximize its effective area as it observed the faint EUV flux from Epsilon. A smaller, high resolution aperture might have been technically capable of measuring the continuum level between lines, but would have allowed dramatically less light into the spectrograph and thus registered no spectrum over the short rocket flight. Resolution of the true continuum likely requires a resolution well above even the DEUCE FUV aperture, which comes with the consequence of an increasingly smaller instrument effective area.

Although this drop in effective area could be balanced by improvements in detector QE, telescope reflectivity, or grating efficiency, these improvements are strongly limited by the technology available. Even with 100% efficiency, such improvements would be unable to match the large reduction in observing efficiency (well over 1000$\times$) created by a dramatically smaller aperture used on the same rocket flight. Short of Epsilon being transported dramatically closer to Earth, the only true solution to the need for higher resolution and a smaller aperture is more observing time, which faces the limitations described previously.

Finally, such a small aperture would be significantly smaller than the telescope spot (like DEUCE's FUV aperture) and would seriously increase the difficulty of the payload calibration, requiring a more thorough study of aperture positions and losses either in flight or on the ground. All of these challenges make the prospect of significantly increasing the EUV resolution of future observations poor.

4.8.2.3 Model grids

A third area for improvement is in the modeling and model grids themselves. The models used for the current analysis were obtained from online grids sampling a discrete parameter space, or directly from their authors in the case of the Aufdenberg models. While this was convenient and highly accessible, the discretization of the utilized models limits the accuracy of the χ^2 minimization; for instance, it is entirely possible that the true best fit to the DEUCE data is an TLUSTY model with parameters T=22,500 K, log g = 3.35. These parameters fall between the discrete units of the published online models and were not tested. This results in the best-fit model of my fits almost certainly not being the same best fit model allowed by a continuous parameter distribution, and results in extra uncertainty in the overall fits.

The solution to this problem is to obtain models on a more finely-spaced grid that can better match the actual properties of Epsilon CMa. Such grids, however, are not published online and must be created personally. This requires learning and understanding the modelling process for multiple different models, which can come with significant nuance and time commitment. It is precisely to avoid this steep task that model grids are published online for the general astronomical community. A much finer grid also significantly increases the computation time for a brute force fit as performed in this analysis. While more clever fitting algorithms could certainly be devised for the fits, obtaining and working with custom models greatly increases the complexity of the project, even though it would undoubtedly increase the accuracy of the fitting.

4.8.2.4 Stellar parameters

Finally, there is the error in the determinations of the stellar parameters of Epsilon CMa themselves. If Epsilon's temperature, surface gravity, N(H I) column, and other parameters were known with total precision, the deficiencies or merits of stellar models estimating its flux would become instantly apparent. Instead, the uncertainty in each of these parameters translates directly into uncertainty into the accuracy of stellar models and confuses the situation significantly. As

future observations narrow down and constrain the parameter space of Epsilon's temperature and surface gravity especially, fitting techniques like this work will have more discriminative power, and the accuracy of stellar models in estimating Epsilon's EUV and FUV flux will be able to be more thoroughly tested.

Bibliography

[1] Mark J. Abbott, William T. Boyd, Pat Jelinsky, Carol Christian, Anne Miller-Bagwell, Michael Lampton, Roger F. Malina, and John V. Vallerga. The Calibration of the EUVE Spectrometers. I. Wavelength Calibration and Resolution. ApJS, 107:451, November 1996.

[2] Aufdenberg, J., Hauschildt, P., Shore, S., and Baron, E. A spherical non-lte line-blanketed stellar atmosphere model of the early B giant Epsilon Canis Majoris. ApJ, 498, 1998.

[3] Thomas R. Ayres. StarCAT: A Catalog of Space Telescope Imaging Spectrograph Ultraviolet Echelle Spectra of Stars. ApJS, 187(1):149–171, March 2010.

[4] A. Boggess, F. A. Carr, D. C. Evans, D. Fischel, H. R. Freeman, C. F. Fuechsel, D. A. Klinglesmith, V. L. Krueger, G. W. Longanecker, and J. V. Moore. The IUE spacecraft and instrumentation. Nature, 275(5679):372–377, October 1978.

[5] R. C. Bohlin. Copernicus observations of interstellar absorption at Lyman Alpha. ApJ, 200:402–414, September 1975.

[6] I. Brott, S. E. de Mink, M. Cantiello, N. Langer, A. de Koter, C. J. Evans, I. Hunter, C. Trundle, and J. S. Vink. Rotating massive main-sequence stars. I. Grids of evolutionary models and isochrones. A&A, 530:A115, June 2011.

[7] G. Bruzual and S. Charlot. Stellar population synthesis at the resolution of 2003. MNRAS, 344(4):1000–1028, October 2003.

[8] Alexander P. Calverley, George D. Becker, Martin G. Haehnelt, and James S. Bolton. Measurements of the ultraviolet background at $4.6 < z < 6.4$ using the quasar proximity effect. MNRAS, 412(4):2543–2562, April 2011.

[9] Webster Cash, Timothy Cook, Clarke Chambellan, Donald Heyse, David Hofmockel, Theodore P. Snow, David Windt, and Clyde Zaidins. A Far Ultraviolet Rocket-Borne Spectrograph. Experimental Astronomy, 1(2):123–143, March 1989.

[10] Cassinelli, J., Cohen, D., MacFarlane, J, and et al. EUVE Spectroscopy of Epsilon Canis Majoris (B2 II) from 70 to 730A. ApJ, 438, 1995.

[11] Cassinelli, J., Cohen, D., MacFarlane, J, and et al. EUVE Spectroscopy of Beta Canis Majoris (B1 II-III) from 500A to 700A. ApJ, 460, 1996.

[12] Fiorella Castelli. Atlas9 Archive and Website, 2020. https://wwwuser.oats.inaf.it/castelli/.

[13] Castelli, F. and Kurucz, R. New Grids of ATLAS9 Model Atmospheres. Proc. IAU, 210, 2004.

[14] N. Castro, L. Fossati, S. Hubrig, S. Simón-Díaz, M. Schöller, I. Ilyin, T. A. Carrol, N. Langer, T. Morel, F. R. N. Schneider, N. Przybilla, A. Herrero, A. de Koter, L. M. Oskinova, A. Reisenegger, H. Sana, and BOB Collaboration. B fields in OB stars (BOB). Detection of a strong magnetic field in the O9.7 V star HD 54879. A&A, 581:A81, September 2015.

[15] A. D. Code and M. R. Meade. Ultraviolet photometry from Orbiting Astronomical Observatory. XXXII. An atlas of ultraviolet stellar spectra. ApJS, 39:195–289, February 1979.

[16] Code, A., Davis, J., Bless, R., and Brown, H. Empirical effective temperatures and bolometric corrections for early-type stars. ApJ, 203, 1976.

[17] Cohen, D., Hurwitz, M., Cassinelli, J., and Bowyer, S. ORFEUS-SPAS II EUV Spectroscopy of epsilon Canis Majoris (B2 II). ApJ, 500, 1998.

[18] Timothy A. Cook, Webster Cash, and James C. Green. Far ultraviolet spectrophotometry of BD +28 4211. Advances in Space Research, 11(11):29–32, January 1991.

[19] Stefan Czesla, Sebastian Schröter, Christian P. Schneider, Klaus F. Huber, Fabian Pfeifer, Daniel T. Andreasen, and Mathias Zechmeister. PyA: Python astronomy-related packages, Jun 2019.

[20] Athanassios Diplas and Blair D. Savage. An IUE Survey of Interstellar H I LY alpha Absorption. I. Column Densities. ApJS, 93:211, July 1994.

[21] J. J. Eldridge, E. R. Stanway, L. Xiao, L. A. S. McClelland, G. Taylor, M. Ng, S. M. L. Greis, and J. C. Bray. Binary Population and Spectral Synthesis Version 2.1: Construction, Observational Verification, and New Results. , 34, November 2017.

[22] Nicholas Erickson. DEUCE Photo Archive, 2020. https://sites.google.com/view/rocket-adventures.

[23] Claude-André Faucher-Giguère. A cosmic UV/X-ray background model update. MNRAS, 493(2):1614–1632, April 2020.

[24] Ferlet, R. Abundence of Interstellar Nitrogen. A&A, 98, 1981.

[25] Ferlet, R., Vidal-Madjar, A., and Gry, C. Na I as a tracer of H I in the diffuse interstellar medium. ApJ, 298, 1985.

[26] C. R. Fierro, J. Borissova, J. Zsargó, A. Díaz-Azuara, R. Kurtev, L. Georgiev, S. Ramírez Alegría, and F. Peñaloza. Atlas of CMFGEN Models for OB Massive Stars. , 127(951):428, May 2015.

[27] Steven L. Finkelstein, Anson D'Aloisio, Jan-Pieter Paardekooper, Jr. Ryan, Russell, Peter Behroozi, Kristian Finlator, Rachael Livermore, Phoebe R. Upton Sanderbeck, Claudio Dalla Vecchia, and Sadegh Khochfar. Conditions for Reionizing the Universe with a Low Galaxy Ionizing Photon Escape Fraction. ApJ, 879(1):36, July 2019.

[28] Brian T. Fleming, Kevin France, Nicholas Nell, Nicholas Kruczek, Robert Kane, James Green, Manuel A. Quijada, Javier Del Hoyo, and Oswald Siegmund. SISTINE: a pathfinder for FUV imaging spectroscopy on future NASA astrophysics missions. In Proc. SPIE, volume 9905 of Society of Photo-Optical Instrumentation Engineers (SPIE) Conference Series, page 99050A, July 2016.

[29] Kevin France, Brian Fleming, Garrett West, Stephan R. McCand liss, Matthew R. Bolcar, Walter Harris, Leonidas Moustakas, John M. O'Meara, Ilaria Pascucci, Jane Rigby, David Schiminovich, and Jason Tumlinson. The LUVOIR Ultraviolet Multi-Object Spectrograph (LUMOS): instrument definition and design. In Society of Photo-Optical Instrumentation Engineers (SPIE) Conference Series, volume 10397 of Society of Photo-Optical Instrumentation Engineers (SPIE) Conference Series, page 1039713, August 2017.

[30] Antonella Fruscione, Isabel Hawkins, Patrick Jelinsky, and Alexandria Wiercigroch. The Distribution of Neutral Hydrogen in the Interstellar Medium. I. The Data. ApJS, 94:127, September 1994.

[31] Gaia Collaboration, A. G. A. Brown, A. Vallenari, T. Prusti, J. H. J. de Bruijne, C. Babusiaux, C. A. L. Bailer-Jones, M. Biermann, D. W. Evans, L. Eyer, F. Jansen, C. Jordi, S. A. Klioner, U. Lammers, L. Lindegren, X. Luri, F. Mignard, C. Panem, D. Pourbaix, S. Randich, P. Sartoretti, H. I. Siddiqui, C. Soubiran, F. van Leeuwen, N. A. Walton, F. Arenou, U. Bastian, M. Cropper, R. Drimmel, D. Katz, M. G. Lattanzi, J. Bakker, C. Cacciari, J. Castañeda, L. Chaoul, N. Cheek, F. De Angeli, C. Fabricius, R. Guerra, B. Holl, E. Masana, R. Messineo, N. Mowlavi, K. Nienartowicz, P. Panuzzo, J. Portell, M. Riello, G. M. Seabroke, P. Tanga, F. Thévenin, G. Gracia-Abril, G. Comoretto, M. Garcia-Reinaldos, D. Teyssier, M. Altmann, R. Andrae, M. Audard, I. Bellas-Velidis, K. Benson, J. Berthier, R. Blomme, P. Burgess, G. Busso, B. Carry, A. Cellino, G. Clementini, M. Clotet, O. Creevey, M. Davidson, J. De Ridder, L. Delchambre, A. Dell'Oro, C. Ducourant, J. Fernández-Hernández, M. Fouesneau, Y. Frémat, L. Galluccio, M. García-Torres, J. González-Núñez, J. J. González-Vidal, E. Gosset, L. P. Guy, J. L. Halbwachs, N. C. Hambly, D. L. Harrison, J. Hernández, D. Hestroffer, S. T. Hodgkin, A. Hutton, G. Jasniewicz, A. Jean-Antoine-Piccolo, S. Jordan, A. J. Korn, A. Krone-Martins, A. C. Lanzafame, T. Lebzelter, W. Löffler, M. Manteiga, P. M. Marrese, J. M. Martín-Fleitas, A. Moitinho, A. Mora, K. Muinonen, J. Osinde, E. Pancino, T. Pauwels, J. M. Petit, A. Recio-Blanco, P. J. Richards, L. Rimoldini, A. C. Robin, L. M. Sarro, C. Siopis, M. Smith, A. Sozzetti, M. Süveges, J. Torra, W. van Reeven, U. Abbas, A. Abreu Aramburu, S. Accart, C. Aerts, G. Altavilla, M. A. Álvarez, R. Alvarez, J. Alves, R. I. Anderson, A. H. Andrei, E. Anglada Varela, E. Antiche, T. Antoja, B. Arcay, T. L. Astraatmadja, N. Bach, S. G. Baker, L. Balaguer-Núñez, P. Balm, C. Barache, C. Barata, D. Barbato, F. Barblan, P. S. Barklem, D. Barrado, M. Barros, M. A. Barstow, S. Bartholomé Muñoz, J. L. Bassilana, U. Becciani, M. Bellazzini, A. Berihuete, S. Bertone, L. Bianchi, O. Bienaymé, S. Blanco-Cuaresma, T. Boch, C. Boeche, A. Bombrun, R. Borrachero, D. Bossini, S. Bouquillon, G. Bourda, A. Bragaglia, L. Bramante, M. A. Breddels, A. Bressan, N. Brouillet, T. Brüsemeister, E. Brugaletta, B. Bucciarelli, A. Burlacu, D. Busonero, A. G. Butkevich, R. Buzzi, E. Caffau, R. Cancelliere, G. Cannizzaro, T. Cantat-Gaudin, R. Carballo, T. Carlucci, J. M. Carrasco, L. Casamiquela, M. Castellani, A. Castro-Ginard, P. Charlot, L. Chemin, A. Chiavassa, G. Cocozza, G. Costigan, S. Cowell, F. Crifo, M. Crosta, C. Crowley, J. Cuypers, C. Dafonte, Y. Damerdji, A. Dapergolas, P. David,

M. David, P. de Laverny, F. De Luise, R. De March, D. de Martino, R. de Souza, A. de Torres, J. Debosscher, E. del Pozo, M. Delbo, A. Delgado, H. E. Delgado, P. Di Matteo, S. Diakite, C. Diener, E. Distefano, C. Dolding, P. Drazinos, J. Durán, B. Edvardsson, H. Enke, K. Eriksson, P. Esquej, G. Eynard Bontemps, C. Fabre, M. Fabrizio, S. Faigler, A. J. Falcão, M. Farràs Casas, L. Federici, G. Fedorets, P. Fernique, F. Figueras, F. Filippi, K. Findeisen, A. Fonti, E. Fraile, M. Fraser, B. Frézouls, M. Gai, S. Galleti, D. Garabato, F. García-Sedano, A. Garofalo, N. Garralda, A. Gavel, P. Gavras, J. Gerssen, R. Geyer, P. Giacobbe, G. Gilmore, S. Girona, G. Giuffrida, F. Glass, M. Gomes, M. Granvik, A. Gueguen, A. Guerrier, J. Guiraud, R. Gutiérrez-Sánchez, R. Haigron, D. Hatzidimitriou, M. Hauser, M. Haywood, U. Heiter, A. Helmi, J. Heu, T. Hilger, D. Hobbs, W. Hofmann, G. Holland, H. E. Huckle, A. Hypki, V. Icardi, K. Janßen, G. Jevardat de Fombelle, P. G. Jonker, Á. L. Juhász, F. Julbe, A. Karampelas, A. Kewley, J. Klar, A. Kochoska, R. Kohley, K. Kolenberg, M. Kontizas, E. Kontizas, S. E. Koposov, G. Kordopatis, Z. Kostrzewa-Rutkowska, P. Koubsky, S. Lambert, A. F. Lanza, Y. Lasne, J. B. Lavigne, Y. Le Fustec, C. Le Poncin-Lafitte, Y. Lebreton, S. Leccia, N. Leclerc, I. Lecoeur-Taibi, H. Lenhardt, F. Leroux, S. Liao, E. Licata, H. E. P. Lindstrøm, T. A. Lister, E. Livanou, A. Lobel, M. López, S. Managau, R. G. Mann, G. Mantelet, O. Marchal, J. M. Marchant, M. Marconi, S. Marinoni, G. Marschalkó, D. J. Marshall, M. Martino, G. Marton, N. Mary, D. Massari, G. Matijevič, T. Mazeh, P. J. McMillan, S. Messina, D. Michalik, N. R. Millar, D. Molina, R. Molinaro, L. Molnár, P. Montegriffo, R. Mor, R. Morbidelli, T. Morel, D. Morris, A. F. Mulone, T. Muraveva, I. Musella, G. Nelemans, L. Nicastro, L. Noval, W. O'Mullane, C. Ordénovic, D. Ordóñez-Blanco, P. Osborne, C. Pagani, I. Pagano, F. Pailler, H. Palacin, L. Palaversa, A. Panahi, M. Pawlak, A. M. Piersimoni, F. X. Pineau, E. Plachy, G. Plum, E. Poggio, E. Poujoulet, A. Prša, L. Pulone, E. Racero, S. Ragaini, N. Rambaux, M. Ramos-Lerate, S. Regibo, C. Reylé, F. Riclet, V. Ripepi, A. Riva, A. Rivard, G. Rixon, T. Roegiers, M. Roelens, M. Romero-Gómez, N. Rowell, F. Royer, L. Ruiz-Dern, G. Sadowski, T. Sagristà Sellés, J. Sahlmann, J. Salgado, E. Salguero, N. Sanna, T. Santana-Ros, M. Sarasso, H. Savietto, M. Schultheis, E. Sciacca, M. Segol, J. C. Segovia, D. Ségransan, I. C. Shih, L. Siltala, A. F. Silva, R. L. Smart, K. W. Smith, E. Solano, F. Solitro, R. Sordo, S. Soria Nieto, J. Souchay, A. Spagna, F. Spoto, U. Stampa, I. A. Steele, H. Steidelmüller, C. A. Stephenson, H. Stoev, F. F. Suess, J. Surdej, L. Szabados, E. Szegedi-Elek, D. Tapiador, F. Taris, G. Tauran, M. B. Taylor, R. Teixeira, D. Terrett, P. Teyssandier, W. Thuillot, A. Titarenko, F. Torra Clotet, C. Turon, A. Ulla, E. Utrilla, S. Uzzi, M. Vaillant, G. Valentini, V. Valette, A. van Elteren, E. Van Hemelryck, M. van Leeuwen, M. Vaschetto, A. Vecchiato, J. Veljanoski, Y. Viala, D. Vicente, S. Vogt, C. von Essen, H. Voss, V. Votruba, S. Voutsinas, G. Walmsley, M. Weiler, O. Wertz, T. Wevers, Ł. Wyrzykowski, A. Yoldas, M. Žerjal, H. Ziaeepour, J. Zorec, S. Zschocke, S. Zucker, C. Zurbach, and T. Zwitter. Gaia Data Release 2. Summary of the contents and survey properties. A&A, 616:A1, August 2018.

[32] C. Georgy, S. Ekström, A. Granada, G. Meynet, N. Mowlavi, P. Eggenberger, and A. Maeder. Populations of rotating stars. I. Models from 1.7 to 15 Msun at Z = 0.014, 0.006, and 0.002 with Ω/Ω_{crit} between 0 and 1. A&A, 553:A24, May 2013.

[33] Gies, D., Lambert, D., , and . Carbon, Nitrogen, and Oxygen Abundances in Early B-Type Stars. ApJ, 387, 1992.

[34] Randy Gladstone. Randy Gladstone SwRI Website, 2020. https://grad.space.swri.edu/people/faculty/rgladstone.html.

[35] Nickolay Y. Gnedin and Nicholas Hollon. Cooling and Heating Functions of Photoionized Gas. ApJS, 202(2):13, October 2012.

[36] James Green, Patrick Jelinsky, and Stuart Bowyer. The Extreme Ultraviolet Spectrum of G191-B2B and the Ionization of the Local Interstellar Medium. ApJ, 359:499, August 1990.

[37] James C. Green, Timothy A. Cook, and Webster Cash. Observations of B stars and Comet Austin from 900-1180 Å. Advances in Space Research, 11(11):25–28, January 1991.

[38] James C. Green, Cynthia S. Froning, Steve Osterman, Dennis Ebbets, Sara H. Heap, Claus Leitherer, Jeffrey L. Linsky, Blair D. Savage, Kenneth Sembach, J. Michael Shull, Oswald H. W. Siegmund, Theodore P. Snow, John Spencer, S. Alan Stern, John Stocke, Barry Welsh, Stéphane Béland, Eric B. Burgh, Charles Danforth, Kevin France, Brian Keeney, Jason McPhate, Steven V. Penton, John Andrews, Kenneth Brownsberger, Jon Morse, and Erik Wilkinson. The Cosmic Origins Spectrograph. ApJ, 744(1):60, January 2012.

[39] James C. Green, Nicholas J. Nell, Nicholas Erickson, Brian T. Fleming, Kevin C. France, Adrian Martin, Oswald Siegmund, and John V. Vallerga. In-flight performance of a 200mm x 200mm microchannel plate detector. In Oswald H. Siegmund, editor, UV, X-Ray, and Gamma-Ray Space Instrumentation for Astronomy XXI, volume 11118, pages 196 – 200. International Society for Optics and Photonics, SPIE, 2019.

[40] James C. Green, Theodore P. Snow, Timothy A. Cook, Webster C. Cash, and Orion Poplawski. The Anomalous Extinction Curve in the Direction of rho Ophiuchi from 950 to 1180 Angstroms. ApJ, 395:289, August 1992.

[41] James C. Green, Erik Wilkinson, Thomas R. Ayres, and Webster C. Cash. Extreme Ultraviolet Spectroscopy of Capella. ApJL, 397:L99, October 1992.

[42] Gregorio, A., Stalio, R., Castelli, F., Hack, M., and Holberg, J. UVSTAR Observations of Adara (Epsilon CMa): 575-1250A. A&A, 383, 2002.

[43] J. H. Groh, S. Ekström, C. Georgy, G. Meynet, A. Choplin, P. Eggenberger, R. Hirschi, A. Maeder, L. J. Murphy, I. Boian, and E. J. Farrell. Grids of stellar models with rotation. IV. Models from 1.7 to 120 $M_\odot$ at a metallicity Z = 0.0004. A&A, 627:A24, July 2019.

[44] Gry, C. and Dupin, O. The Line of Sight to Epsilon Canis Majoris: Depletion and Extent of the Local Cloud. LNP, 506, 1998.

[45] Gry, C. and Jenkins, E. Local clouds: Ionization, temperatures, electron densities and interfaces, from GHRS and IMAPS spectra of Epsilon Canis Majoris. A&A, 367, 2001.

[46] Gry, C., Lemonon, L., Vidal-Madjar, A., Lemoine, M., and Ferlet, R. The interstellar void in the direction to epsilon canis majoris: local clouds and hot gas. A&A, 302, 1995.

[47] S. B. Gudennavar, S. G. Bubbly, K. Preethi, and Jayant Murthy. A Compilation of Interstellar Column Densities. ApJS, 199(1):8, March 2012.

[48] Francesco Haardt and Piero Madau. Radiative Transfer in a Clumpy Universe. IV. New Synthesis Models of the Cosmic UV/X-Ray Background. ApJ, 746(2):125, February 2012.

[49] Hanbury Brown, R., Davis, J., and Allen, L.R. The Angular Diameter of 32 Stars. MNRAS, 167, 1974.

[50] Timothy M. Heckman, Sanchayeeta Borthakur, Roderik Overzier, Guinevere Kauffmann, Antara Basu-Zych, Claus Leitherer, Ken Sembach, D. Chris Martin, R. Michael Rich, David Schiminovich, and Mark Seibert. Extreme Feedback and the Epoch of Reionization: Clues in the Local Universe. ApJ, 730(1):5, March 2011.

[51] Akira Hiruma. Hamamatsu Photonics MCP Diagram, 2020. https://www.hamamatsu.com/resources/pdf/news/2020_09_30_en.pdf.

[52] Hoare, M., Drew, J., and Denby, M. The first measurement of the Lyman continuum emission from normal stars. MNRAS, 262, 1993.

[53] L. M. Hobbs. Observations of interstellar lines of Na I, and/or Ca II toward 47 stars. ApJS, 38:129–146, October 1978.

[54] Vincent Hue, G. Randall Gladstone, Thomas K. Greathouse, Joshua A. Kammer, Michael W. Davis, Bertrand Bonfond, Maarten H. Versteeg, Denis C. Grodent, Jean-Claude Gérard, Scott J. Bolton, Steven M. Levin, and Ben D. Byron. In-flight Characterization and Calibration of the Juno-ultraviolet Spectrograph (Juno-UVS). AJ, 157(2):90, February 2019.

[55] C. M. Humphries, K. Nandy, and E. Kontizas. Ultraviolet energy distributions of luminous early-type stars from TD1 satellite observations. ApJ, 195:111–119, January 1975.

[56] Edward B. Jenkins, Michael A. Reale, Paul M. Zucchino, and Ulysses J. Sofia. High Resolution Spectroscopy in the Far UV: Observations of the Interstellar Medium by IMAPS on ORFEUS-SPAS. Ap&SS, 239(2):315–360, September 1996.

[57] Koleva, M. and Vazdekis, A. Stellar Population Models in the UV. A&A, 538, 2012.

[58] Juna A. Kollmeier, David H. Weinberg, Benjamin D. Oppenheimer, Francesco Haardt, Neal Katz, Romeel Davé, Mark Fardal, Piero Madau, Charles Danforth, Amanda B. Ford, Molly S. Peeples, and Joseph McEwen. The Photon Underproduction Crisis. ApJL, 789(2):L32, July 2014.

[59] Kramida, A., Ralchenko, Y., Reader, J., and NIST ASD Team. NIST Atomic Spectra Database (ver. 5.7.1). 2019.

[60] Nicholas Kruczek, Nicholas Nell, Kevin France, Keri Hoadley, Brian Fleming, Robert Kane, Stefan Ulrich, Arika Egan, and Dawson Beatty. The third flight of the Colorado high-resolution echelle stellar spectrograph (CHESS): improvements, calibrations, and preliminary results. In Society of Photo-Optical Instrumentation Engineers (SPIE) Conference Series, volume 10397 of Society of Photo-Optical Instrumentation Engineers (SPIE) Conference Series, page 103971G, August 2017.

[61] Nicholas Kruczek, Nicholas Nell, Kevin France, Keri Hoadley, Brian Fleming, Stefan Ulrich, Alexander D. Miller, Arika Egan, Emily Witt, and Robert Kane. The fourth flight of CHESS: spectral resolution enhancements for high-resolution FUV spectroscopy. In Space Telescopes and Instrumentation 2018: Ultraviolet to Gamma Ray, volume 10699 of Society of Photo-Optical Instrumentation Engineers (SPIE) Conference Series, page 106990K, July 2018.

[62] M. R. Krumholz, M. R. Bate, H. G. Arce, J. E. Dale, R. Gutermuth, R. I. Klein, Z. Y. Li, F. Nakamura, and Q. Zhang. Star Cluster Formation and Feedback. In Henrik Beuther, Ralf S. Klessen, Cornelis P. Dullemond, and Thomas Henning, editors, Protostars and Planets VI, page 243, January 2014.

[63] R. L. Kurucz. Model Atmospheres for Population Synthesis. In Beatriz Barbuy and Alvio Renzini, editors, The Stellar Populations of Galaxies, volume 149, page 225, January 1992.

[64] Lanz, T. and Hubeny, I. A grid of non-LTE line-blanketed model atmospheres of early B-type stars. ApJS, 169, 2007.

[65] Lanz, T. and Hubeny, I. Tlusty web repository, 2020. http://tlusty.oca.eu/.

[66] Claus Leitherer, Daniel Schaerer, Jeffrey D. Goldader, Rosa M. González Delgado, Carmelle Robert, Denis Foo Kune, Duília F. de Mello, Daniel Devost, and Timothy M. Heckman. Starburst99: Synthesis Models for Galaxies with Active Star Formation. ApJS, 123(1):3–40, July 1999.

[67] J. M. Lerner, J. Flamand, J. P. Laude, G. Passereau, and A Thevenon. Diffraction Gratings Ruled And Holographic - A Review. Proc. SPIE, 0240, 1981.

[68] Lesh, J.R. New Kinematical Data for Bright Southern OB Stars. A&A, 5, 1972.

[69] J. Linsky, S. Redfield, and D. Tilipman. The interface between the outer heliosphere and the inner LISM: Morphology of the LIC, its hydrogen hole, Stromgren shells, and 60Fe accretion. In American Astronomical Society Meeting Abstracts #235, volume 235 of American Astronomical Society Meeting Abstracts, page 442.01, January 2020.

[70] Abraham Loeb and Rennan Barkana. The Reionization of the Universe by the First Stars and Quasars. ARA&A, 39:19–66, January 2001.

[71] Renata Longo, Roberto Stalio, Ronald S. Polidan, and Lucio Rossi. Intrinsic Ultraviolet (912–3200 Angstrom) Energy Distribution of OB Stars. ApJ, 339:474, April 1989.

[72] L. S. Lyubimkov, S. I. Rostopchin, T. M. Rachkovskaya, D. B. Poklad, and D. L. Lambert. Surface abundances of light elements for a large sample of early B-type stars - IV. The magnesium abundance in 52 stars - a test of metallicity. MNRAS, 358(1):193–201, March 2005.

[73] Xiangcheng Ma, Philip F. Hopkins, Daniel Kasen, Eliot Quataert, Claude-André Faucher-Giguère, Dušan Kereš, Norman Murray, and Allison Strom. Binary stars can provide the 'missing photons' needed for reionization. MNRAS, 459(4):3614–3619, July 2016.

[74] Xiangcheng Ma, Daniel Kasen, Philip F. Hopkins, Claude-André Faucher-Giguère, Eliot Quataert, Dušan Kereš, and Norman Murray. The difficulty of getting high escape fractions of ionizing photons from high-redshift galaxies: a view from the FIRE cosmological simulations. MNRAS, 453(1):960–975, October 2015.

[75] Xiangcheng Ma, Eliot Quataert, Andrew Wetzel, Philip F. Hopkins, Claude-André Faucher-Giguère, and Dušan Kereš. No missing photons for reionization: moderate ionizing photon escape fractions from the FIRE-2 simulations. MNRAS, 498(2):2001–2017, October 2020.

[76] Piero Madau and Francesco Haardt. Cosmic Reionization after Planck: Could Quasars Do It All? ApJL, 813(1):L8, November 2015.

[77] D. Massa and E. L. Fitzpatrick. A Recalibration of IUE NEWSIPS Low-Dispersion Data. ApJS, 126(2):517–535, February 2000.

[78] Ian D. McGreer, Andrei Mesinger, and Valentina D'Odorico. Model-independent evidence in favour of an end to reionization by z ≈ 6. MNRAS, 447(1):499–505, February 2015.

[79] Christopher F. McKee and Jonathan P. Williams. The Luminosity Function of OB Associations in the Galaxy. ApJ, 476(1):144–165, February 1997.

[80] A. F. McLeod, J. E. Dale, C. J. Evans, A. Ginsburg, J. M. D. Kruijssen, E. W. Pellegrini, S. K. Ramsay, and L. Testi. Feedback from massive stars at low metallicities: MUSE observations of N44 and N180 in the Large Magellanic Cloud. MNRAS, 486(4):5263–5288, July 2019.

[81] J. Meaburn, R. X. McGee, and L. M. Newton. Complex and broad HI profiles in the vicinity of giant LMC shells. MNRAS, 206:705–711, February 1984.

[82] Sz. Mészáros, C. Allende Prieto, B. Edvardsson, F. Castelli, A. E. García Pérez, B. Gustafsson, S. R. Majewski, B. Plez, R. Schiavon, M. Shetrone, and A. de Vicente. New ATLAS9 and MARCS Model Atmosphere Grids for the Apache Point Observatory Galactic Evolution Experiment (APOGEE). AJ, 144(4):120, October 2012.

[83] Johan Meuris, Bernardi Martín, Alexander Wolf, Guillaume Chéreau, Georg Zotti, Marcos Cardinot, Hans Lambermont, and Khalid AlAjaji. Stellarium Astronomy Software, 2020. https://stellarium.org/.

[84] David M. Meyer, M. Jura, and Jason A. Cardelli. The Definitive Abundance of Interstellar Oxygen. ApJ, 493(1):222–229, January 1998.

[85] H. W. Moos, W. C. Cash, L. L. Cowie, A. F. Davidsen, A. K. Dupree, P. D. Feldman, S. D. Friedman, J. C. Green, R. F. Green, C. Gry, J. B. Hutchings, E. B. Jenkins, J. L. Linsky, R. F. Malina, A. G. Michalitsianos, B. D. Savage, J. M. Shull, O. H. W. Siegmund, T. P. Snow, G. Sonneborn, A. Vidal-Madjar, A. J. Willis, B. E. Woodgate, D. G. York, T. B. Ake, B. G. Andersson, J. P. Andrews, R. H. Barkhouser, L. Bianchi, W. P. Blair, K. R. Brownsberger, A. N. Cha, P. Chayer, S. J. Conard, A. W. Fullerton, G. A. Gaines, R. Grange, M. A. Gummin, G. Hebrard, G. A. Kriss, J. W. Kruk, D. Mark, D. K. McCarthy, C. L. Morbey, R. Murowinski, E. M. Murphy, W. R. Oegerle, R. G. Ohl, C. Oliveira, S. N. Osterman, D. J. Sahnow, M. Saisse, K. R. Sembach, H. A. Weaver, B. Y. Welsh, E. Wilkinson, and W. Zheng. Overview of the Far Ultraviolet Spectroscopic Explorer Mission. ApJL, 538(1):L1–L6, July 2000.

[86] Morel, T., Hubrig, S., and Briquet, M. Nitrogen enrichment, boron depletion and magnetic fields in slowly-rotating B-type dwarfs. A&A, 481, 2008.

[87] F. Nicastro, J. Kaastra, Y. Krongold, S. Borgani, E. Branchini, R. Cen, M. Dadina, C. W. Danforth, M. Elvis, F. Fiore, A. Gupta, S. Mathur, D. Mayya, F. Paerels, L. Piro, D. Rosa-Gonzalez, J. Schaye, J. M. Shull, J. Torres-Zafra, N. Wijers, and L. Zappacosta. Observations of the missing baryons in the warm-hot intergalactic medium. Nature, 558(7710):406–409, June 2018.

[88] J. S. Nichols and J. L Linsky. The final archive and recalibration of the international ultraviolet explorer (iue) satellite. AL, 111:1, 1996.

[89] A. Palacios, A. Lèbre, M. Sanguillon, and P. Maeght. The POLLUX database of synthetic stellar spectra. In Philippe Prugniel and Harinder P. Singh, editors, Astronomical Society of India Conference Series, volume 6 of Astronomical Society of India Conference Series, page 63, January 2012.

[90] Nino Panagia. Some Physical parameters of early-type stars. AJ, 78:929–934, November 1973.

[91] F. Paresce, S. Kumar, and C. S. Bowyer. Continuous discharge line source for the extreme ultraviolet. ApOpt, 10:1904–1908, January 1971.

[92] Shaghayegh Parsa, James S. Dunlop, Ross J. McLure, and Alice Mortlock. The galaxy UV luminosity function at z 2-4; new results on faint-end slope and the evolution of luminosity density. MNRAS, 456(3):3194–3211, March 2016.

[93] A. Pauldrach, J. Puls, and R. P. Kudritzki. Radiation-driven winds of hot luminous stars. Improvements of the theory and first results. A&A, 164:86–100, August 1986.

[94] Jeff Percival. Star Tracker 5000, 2020. http://www.sal.wisc.edu/st5000/rockets/36.311

[95] Perryman M., Lindegren L., Kovalevsky J., and et al. The Hipparcos Catalogue. A&A, 323, 1997.

[96] Geraldine J. Peters. The Chemical Compositions of Three Fundamental Early B-Type Standards. IUE Proposal, January 1994.

[97] Planck Collaboration, P. A. R. Ade, N. Aghanim, M. Arnaud, M. Ashdown, J. Aumont, C. Baccigalupi, A. J. Banday, R. B. Barreiro, J. G. Bartlett, N. Bartolo, E. Battaner, R. Battye, K. Benabed, A. Benoît, A. Benoit-Lévy, J. P. Bernard, M. Bersanelli, P. Bielewicz, J. J. Bock, A. Bonaldi, L. Bonavera, J. R. Bond, J. Borrill, F. R. Bouchet, F. Boulanger, M. Bucher, C. Burigana, R. C. Butler, E. Calabrese, J. F. Cardoso, A. Catalano, A. Challinor, A. Chamballu, R. R. Chary, H. C. Chiang, J. Chluba, P. R. Christensen, S. Church, D. L. Clements, S. Colombi, L. P. L. Colombo, C. Combet, A. Coulais, B. P. Crill, A. Curto, F. Cuttaia, L. Danese, R. D. Davies, R. J. Davis, P. de Bernardis, A. de Rosa, G. de Zotti, J. Delabrouille, F. X. Désert, E. Di Valentino, C. Dickinson, J. M. Diego, K. Dolag, H. Dole, S. Donzelli, O. Doré, M. Douspis, A. Ducout, J. Dunkley, X. Dupac, G. Efstathiou, F. Elsner, T. A. Enßlin, H. K. Eriksen, M. Farhang, J. Fergusson, F. Finelli, O. Forni, M. Frailis, A. A. Fraisse, E. Franceschi, A. Frejsel, S. Galeotta, S. Galli, K. Ganga, C. Gauthier, M. Gerbino, T. Ghosh, M. Giard, Y. Giraud-Héraud, E. Giusarma, E. Gjerløw, J. González-Nuevo, K. M. Górski, S. Gratton, A. Gregorio, A. Gruppuso, J. E. Gudmundsson, J. Hamann, F. K. Hansen, D. Hanson, D. L. Harrison, G. Helou, S. Henrot-Versillé, C. Hernández-Monteagudo, D. Herranz, S. R. Hildebrand t, E. Hivon, M. Hobson, W. A. Holmes, A. Hornstrup, W. Hovest, Z. Huang, K. M. Huffenberger, G. Hurier, A. H. Jaffe, T. R. Jaffe, W. C. Jones, M. Juvela, E. Keihänen, R. Keskitalo, T. S. Kisner, R. Kneissl, J. Knoche, L. Knox, M. Kunz, H. Kurki-Suonio, G. Lagache, A. Lähteenmäki, J. M. Lamarre, A. Lasenby, M. Lattanzi, C. R. Lawrence, J. P. Leahy, R. Leonardi, J. Lesgourgues, F. Levrier, A. Lewis, M. Liguori,

P. B. Lilje, M. Linden-Vørnle, M. López-Caniego, P. M. Lubin, J. F. Macías-Pérez, G. Maggio, D. Maino, N. Mandolesi, A. Mangilli, A. Marchini, M. Maris, P. G. Martin, M. Martinelli, E. Martínez-González, S. Masi, S. Matarrese, P. McGehee, P. R. Meinhold, A. Melchiorri, J. B. Melin, L. Mendes, A. Mennella, M. Migliaccio, M. Millea, S. Mitra, M. A. Miville-Deschênes, A. Moneti, L. Montier, G. Morgante, D. Mortlock, A. Moss, D. Munshi, J. A. Murphy, P. Naselsky, F. Nati, P. Natoli, C. B. Netterfield, H. U. Nørgaard-Nielsen, F. Noviello, D. Novikov, I. Novikov, C. A. Oxborrow, F. Paci, L. Pagano, F. Pajot, R. Paladini, D. Paoletti, B. Partridge, F. Pasian, G. Patanchon, T. J. Pearson, O. Perdereau, L. Perotto, F. Perrotta, V. Pettorino, F. Piacentini, M. Piat, E. Pierpaoli, D. Pietrobon, S. Plaszczynski, E. Pointecouteau, G. Polenta, L. Popa, G. W. Pratt, G. Prézeau, S. Prunet, J. L. Puget, J. P. Rachen, W. T. Reach, R. Rebolo, M. Reinecke, M. Remazeilles, C. Renault, A. Renzi, I. Ristorcelli, G. Rocha, C. Rosset, M. Rossetti, G. Roudier, B. Rouillé d'Orfeuil, M. Rowan-Robinson, J. A. Rubiño-Martín, B. Rusholme, N. Said, V. Salvatelli, L. Salvati, M. Sandri, D. Santos, M. Savelainen, G. Savini, D. Scott, M. D. Seiffert, P. Serra, E. P. S. Shellard, L. D. Spencer, M. Spinelli, V. Stolyarov, R. Stompor, R. Sudiwala, R. Sunyaev, D. Sutton, A. S. Suur-Uski, J. F. Sygnet, J. A. Tauber, L. Terenzi, L. Toffolatti, M. Tomasi, M. Tristram, T. Trombetti, M. Tucci, J. Tuovinen, M. Türler, G. Umana, L. Valenziano, J. Valiviita, F. Van Tent, P. Vielva, F. Villa, L. A. Wade, B. D. Wandelt, I. K. Wehus, M. White, S. D. M. White, A. Wilkinson, D. Yvon, A. Zacchei, and A. Zonca. Planck 2015 results. XIII. Cosmological parameters. A&A, 594:A13, September 2016.

[98] R. S. Polidan and R. Stalio. Voyager Observations of Hot Luminous Stars. In C. W. H. De Loore, A. J. Willis, and P. Laskarides, editors, Luminous Stars and Associations in Galaxies, volume 116, page 117, January 1986.

[99] H. Remie and H. J. G. L. M. Lamers. Effective temperatures, and radii of luminous O and B stars : a test for the accuracy of the model atmospheres. A&A, 105:85–97, January 1982.

[100] Blair D. Savage and Edward B. Jenkins. A Survey of Local Interstellar Hydrogen from OAO-2 Observations of Lyman Alpha Absorption. ApJ, 172:491, March 1972.

[101] D. Schaerer and A. de Koter. Combined stellar structure and atmosphere models for massive stars. III. Spectral evolution and revised ionizing fluxes of O3-B0 stars. A&A, 322:598–614, June 1997.

[102] Xuejian Shen, Philip F. Hopkins, Claude-André Faucher-Giguère, D. M. Alexander, Gordon T. Richards, Nicholas P. Ross, and R. C. Hickox. The bolometric quasar luminosity function at z = 0-7. MNRAS, 495(3):3252–3275, May 2020.

[103] J. Michael Shull, Joshua Moloney, Charles W. Danforth, and Evan M. Tilton. The Metagalactic Ionizing Background: A Crisis in UV Photon Production or Incorrect Galaxy Escape Fractions? ApJ, 811(1):3, September 2015.

[104] J. Michael Shull, Britton D. Smith, and Charles W. Danforth. The Baryon Census in a Multiphase Intergalactic Medium: 30% of the Baryons May Still be Missing. ApJ, 759(1):23, November 2012.

[105] Shull, M. and Van Steenberg, M. Galactic Interstellar Abundance Surveys with IUE 1. Neutral Hydrogen. ApJ, 294, 1985.

[106] Oswald H. W. Siegmund. Advances in microchannel plate detectors for UV/visible astronomy. In J. Chris Blades and Oswald H. W. Siegmund, editors, Future EUV/UV and Visible Space Astrophysics Missions and Instrumentation., volume 4854 of Society of Photo-Optical Instrumentation Engineers (SPIE) Conference Series, pages 181–190, February 2003.

[107] Jr. Snow, T. P. and E. B. Jenkins. A catalog of 0.2 Å resolution far-ultraviolet stellar spectra measured with Copernicus. ApJS, 33:269–360, March 1977.

[108] Lyman Spitzer. Physical Processes in the Interstellar Medium. John Wiley and Sons, 1978.

[109] Charles C. Steidel, Milan Bogosavljević, Alice E. Shapley, Naveen A. Reddy, Gwen C. Rudie, Max Pettini, Ryan F. Trainor, and Allison L. Strom. The Keck Lyman Continuum Spectroscopic Survey (KLCS): The Emergent Ionizing Spectrum of Galaxies at z $\sim$ 3. ApJ, 869(2):123, December 2018.

[110] S. A. Stern, D. Slater, W. Cash, E. Wilkinson, J. Green, and R. Gladstone. Rocket FUV observations of the Io plasma torus during the Shoemaker-Levy/9 impacts. Geophys. Res. Lett., 22(13):1837–1840, January 1995.

[111] Amiel Sternberg, Tadziu L. Hoffmann, and A. W. A. Pauldrach. Ionizing Photon Emission Rates from O- and Early B-Type Stars and Clusters. ApJ, 599(2):1333–1343, December 2003.

[112] Taylor, M. TOPCAT & STIL: Starlink Table/VOTable Processing Software. ASP Conference Series, 347, 2005.

[113] G. I. Thompson, K. Nandy, C. Jamar, A. Monfils, L. Houziaux, D. J. Carnochan, and R. Wilson. Catalogue of stellar ultraviolet fluxes [...from...] the ESRO satellite TD-1. 1978.

[114] Michael W. Topping and J. Michael Shull. The Efficiency of Stellar Reionization: Effects of Rotation, Metallicity, and Initial Mass Function. ApJ, 800(2):97, February 2015.

[115] Underhill, A., Divan, L., Prevot-Burnichon, M., and Doazan, V. Effective temperatures, angular diameters, distances and linear radii for 160 O and B stars. MNRAS, 189, 1979.

[116] J. V. Vallerga and B. Y. Welsh. Epsilon Canis Majoris and the Ionization of the Local Cloud. ApJ, 444:702, May 1995.

[117] John V. Vallerga, Peter W. Vedder, and Barry Y. Welsh. Intense Extreme Ultraviolet Emission from the B Star epsilon Canis Majoris. ApJL, 414:L65, September 1993.

[118] van Leeuwen F. Validation of the new Hipparcos reduction. A&A, 653, 2007.

[119] Welsh, B. The Interstellar Tunnel of Neutral-Free Gas Towards Beta Canis Majoris. ApJ, 373, 1991.

[120] E. Wilkinson, J. C. Green, R. McLean, and B. Welsh. Extreme Ultraviolet Spectrum of epsilon Canis Majoris between 600-920 Angstroms. In American Astronomical Society Meeting Abstracts #188, volume 188 of American Astronomical Society Meeting Abstracts, page 58.02, May 1996.

[121] Erik Wilkinson. Extreme Ultraviolet Opacity Sources in the DA White Dwarf G191-B2B. PhD thesis, Colorado Univ., Boulder., September 1993.

[122] Erik Wilkinson, James C. Green, and Webster Cash. Extreme Ultraviolet Spectroscopy of G191-B2B: Direct Observation of Ionization Edges. ApJL, 397:L51, September 1992.

[123] Erik Wilkinson, James C. Green, and Webster Cash. The Extreme Ultraviolet Spectrograph: A Radial Groove Grating, Sounding Rocket–borne, Astronomical Instrument. ApJS, 89:211, November 1993.

[124] Erik Wilkinson, James C. Green, Barry Y. Welsh, and Ryan McLean. BDSR: instrument design and initial calibration results. In Pierre Y. Bely and James B. Breckinridge, editors, Space Telescopes and Instruments, volume 2478 of Society of Photo-Optical Instrumentation Engineers (SPIE) Conference Series, pages 153–159, June 1995.

[125] David L. Windt and Webster Cash. The soft X-ray/EUV calibration facility at the University of Colorado. In Proc. SPIE, volume 689 of Society of Photo-Optical Instrumentation Engineers (SPIE) Conference Series, pages 167–177, January 1986.

[126] Zorec J., Cidale L., Arias M.L., and et al. Fundamental Parameters of B supergiants from the BCD system: I Calibration of the lambda, D parameters into Teff. A&A, 501, 2009.

Appendix A

Timelines of major payload events, integration, and launch

Table A.1: A list of major events in the payload life cycle

Date	Event
Mar 2014	DEUCE proposed
Sep 2014	DEUCE awarded
Jun 2015	Grating ordered from JY
Oct 2015	Telescope focal point measured
Nov 2015	Grating produced by JY
Feb 2016	Chess 36.297 launch
Mar 2016	Telescope removed from old skins
Jun 2016	Telescope cleaned
Sep 2016	Nocturn sky tested
Nov 2016	Detector build begun at Sensor Sciences
Dec 2016	Grating acquired and coated at Goddard Space Flight Center
Jan 2017	Detector plates/anode installed at Sensor Sciences
Mar 2017	Nocturn vibe tested at WFF
Apr 2017	Detector coated at Sensor Sciences and acquired
Apr-May 2017	Parts acquired/anodized/helicoiled
May 2017	Delay line measured/coiled, detector HV set, nocturn heat cycled/vacuum tested
Jun 2017	Telescope installed in bulkhead, e-deck construction begun, bonding practice
Late Jun 2017	Pins pressed into grating mount, grating bonded
Early Jul 2017	Skins arrive, spectrograph can assembled, e-deck and e-deck cable layout finalized, first skin assembly/pump down/leak check, telescope installed in skins

Mid Jul 2017	Spectrograph bulkhead built up, grating installed in catcher's mitt, nocturn/counterweights/gauges/baffling installed, cables potted, HV box/power supply potted
Late Jul 2017	Thermistors installed, cable clamp tabs epoxied, feedthroughs installed in spectrograph bulkhead, bellows/grating section installed, grating installed, detector mount installed on spectrograph bulkhead, ion repeller grids installed, shutter door installed/tested, ST5000 mass model installed, initial cabling over spectrograph can, telescope and spectrograph sections connected, detector installed/electrically connected, optically-complete spectrograph section pumped down for the first time.
Early Aug	Payload GSE built, aperture substrate/apertures installed, screws staked
Mid Aug	Long tank testing, final HV adjustments, final spectrum alignment, potting/staking of e-deck, lock-in/staking of grating alignment
Late Aug	Packing/shipping to WFF
Early Sep	WFF Integration
Late Sep	Long Tank Testing, deep wavelength calibration spectra taken
Early Oct 2017	Shipment to WSMR
Late Oct 2017	Pre-launch testing, installation of ST5000
Oct 30, 2017	Launch #1, Beta CMa (failure)
Feb-Jul 2018	End-to end calibration attempts
Mar 2018	Re-epoxying of cable clamp holders
Jul 2018	HV set for flight 2
Oct 2018	LT testing, staking of payload
Dec 2018	Integration at WSMR, launch #2 scrubbed and delayed
Dec 19, 2018	Launch #2, Epsilon CMa
Jan 2019	Entrance aperture transmission testing
Feb 2019	Disassembly of payload, removal of detector
April 2019	Detector QE testing
May 2019	Grating efficiency testing

Table A.2: A timeline of integration operations for the November 2018 DEUCE integration

Date	Event
Oct 28-31	Shipment to WSMR
Nov 5	Travel to WSMR
Nov 6	NSROC/Exp Team unpack, Experiment Setup and Checks, Battery charging/cycling, CACS Burst Cell, Pre-fire range meeting
Nov 7	S19 Leak Check, Experiment Setup and Checks, Skin CACS Mass Model deck, CACS Burst Cell, TM Checks, Gyro Drift Tests, Jamloader Checks
Nov 8	Boost Pump to Gas Shed, Experiment Setup and Checks, FTS VSWR/Test with Range, Fit Checks FTSC/CDI, CDI/Shutter Door, TM Checks, S19, CACS + NFORSe Integration, ST5k Wiring Check, Install ST5k Mass Model
Nov 9	LVT Travel to WSMR, Experiment Build up, TM in the Skin Mate/De-mate, Build up for ST5k Alignment Testing
Nov 12	Pre-vibe ST5k to EXP Alignment Measurement, Unpack Motors, Install HVSS Springs, Turn on test all sub systems and Exp, TM RFI Test, Pre-vibe Sequence in Air, Draw Vacuum
Nov 13	Pre-vibe Sequence in Vacuum, Inspect Terrier, Install FTSC Mass Model, Build up for Vibe, Vibration (3-axis random)
Nov 14	Risk Matrix signed by PI, Post-Vibe sequence in Vacuum, Install/set Terrier fins/interstage assembly, Back fill with N2, Post-vibe Sequence in Air
Nov 15	Build up for Mass Props, Inspect Brant, Install CACS/Remove CACS MM, Install FTSC flight units for MOI's, Install Flight Chute for Balance, Balance/MOI
Nov 16	Post-vibe Checks, Final Mass Props to Mechanical/ACS/FP, Install and set Brant Fins, Interstage, Install lgr, Break TM and sub-system down, Bend, All altitude switches pumped down

Nov 19	Post-vibe Checks, Post-vibe ST5k to EXP Alignment Check, Remove ST5k MM, Install flight unit, Fit check igniter housing/exit cone, ST5k Align to EXP, Walk downs and torque check sheets complete, TM prepared for flight and back in skin, S19 Pyro Mech Install
Nov 20	MRR Inputs due to MM, CUS/Cradle Practice, Experiment data to ASCL Check, Install balance weights and Chute, Check Balance, Flight Build-up, Pump overnight, Return payload to cart
Nov 21	Any other experiment post-vibe checks, Open Loop Test/All Fire in Air/Range Horizontal, Install TTS, Landlines Installed and tested, FTS/CDI GSE Launcher Checks, Weight and CG motors, CACS to NFORSe wiring check, pump overnight
Nov 26	FTS Checks/FTS Install, Stage Motors, MRR, Install Pyros, ACS Phasing Checks, Vacuum Payload, Payload on Cart
Nov 27	MRRAI Received, Payload and pump to rail, begin pumping, Boom test, ACS-TM Test, ACS Rail Leak Test
Nov 28	MRRAI Closure, Payload Walkdown, FRR
Nov 29	Exp Checks, Measure ACS roll alignment, Horizontal/Vertical/FTS Checks, SRPO Approval to Launch

Table A.3: A timeline of launch operations for the October 2017 DEUCE launch

Date	Event
Oct 2-6	Shipping
Oct 9-10	Check out landlines
Oct 11	FTS VSWRs w/MFS
Oct 12-13	ORSA Field Checks
Oct 15	Team Travel to WSMR, LVT Travel
Oct 16	Unpack/setup, Pre-Fire Range Briefing, ACS/S19 Burst Cell, TM Checks, Motor Inspections, Unpack/Motors on Carts
Oct 17	Jam Loader Checks, TM Checks, Build up Terrier, Experiment Vacuum Test
Oct 18	NFORSe/S19/CACS Integrations, Experiment/SD/CDI/FTS Integration, Build up Terrier, Experiment Vacuum Test
Oct 19	TM Final Walkdown in the Skin, S19 Pyro Mech Install, Build up ACS/TM/Exp sections, ORSA Install flight chute, Build up Brant
Oct 23	Vacuum All-fire, Build up for Flight, Check Balance, Pot BB Nozzle, Build up Brant
Oct 24	ACS Phasing, Range Horizontal in air, GSE transport to blockhouse, FTS Install, Motors to the Rail
Oct 25	Payload Pyros, Payload and pump to rail, Boom test, ACS/S19 Rail leak check
Oct 26	Exp pumping, Range Vertical, Rigging, Vehicle Walkdowns, FRR
Oct 27	Exp Pumping, Project Vertical, IRT Briefing, Prelim Arming
Oct 30	Launch, Recover/Pack, Hardness Test Exp Skins, Sabre Electrical FTS Assembly

Appendix B

Previous UV observations of Epsilon CMa

B.1 OAO-2, 1968

OAO-2 was the first successful UV satellite launched by NASA in 1968. A predecessor to Copernicus, it observed Epsilon CMa using its scanning spectrometers from 1160-3600 Å with R∼100. The raw data was published and is accessible online [15]. No paper specifically describing the Epsilon CMa observations was ever published.

B.2 TD-1, 1975

TD-1 was a European UV satellite launched in 1972 that observed Epsilon CMa with the Belgian/UK Ultraviolet Sky Survey Telescope (S2/68) from 1350-2550 Å at R=56. Photometric fluxes in four bandpasses are archived online [113], and a flux-calibrated spectrum of Epsilon CMa in the satellite bandpass was published [55] but the raw data is not available. No paper specifically describing the Epsilon CMa observations was ever published.

B.3 Copernicus (OAO-3), 1977

The Copernicus satellite observed Epsilon CMa from 895-1790 Å [107, 5] using its telescope-spectrometer at a resolution of .2 Å (R=∼5000), although the sensitivity of the U2 phototube used in the observations is low below 1000 Å. Epsilon was also observed with the higher resolution (R=∼20,000) U1 phototube, yielding equivalent widths for multiple absorption lines. No paper specifically describing the Epsilon CMa observations was ever published.

B.4 IUE, 1978

The International Ultraviolet Explorer (IUE) satellite [4] took multiple observations of Epsilon CMa between 1978 and 1995 from 1150-3125 Å with a resolving power of 10-15k. Access to this data is available online in the MAST archive, although science paper specific to Epsilon was ever published.

B.5 Voyager 1, 1982

Voyager 1 obtained spectra of Epsilon CMa in 1982 using its UVS instrument, spanning the 500-1700 Å range with R$\sim$30-115 and 20% calibration accuracy [71, 98]. No flux was detected below 912 Å [42]. No paper specifically describing the Epsilon CMa observations was ever published, although the Voyager spectrum is presented in [42].

B.6 ROSAT, 1992

The ROSAT X-ray telescope [52] photometrically observed Epsilon CMa using its Wide Field Camera through a Sn/Al P2 filter transmitting 520-730 Å with a 600 Å peak. These were the first measurements of Lyman Continuum emission from massive, hot stars. The observations similarly found B2 II Epsilon to be brighter than BI II-III Beta CMa and assigned this difference to an unusually low N(H I) column density.

B.7 EUVE, 1993

The Extreme Ultraviolet Explorer (EUVE) mission observed Epsilon CMa as part of its photometric EUV all-sky survey in 1992 [117], followed by spectral observations in 1993 [10], spanning 70 to 730 Å at an average resolving power of 250 and a flux calibration of approximately 25%. Epsilon was unexpectedly shown to be 10-20$\times$ brighter than the previous brightest known EUV source, white dwarf HZ 43. Epsilon was shown to be the dominant source of local ionizing radiation above 450 Å and to individually produce 6.9$\times$ as much ionizing flux as all previously known,

EUV-bright stars combined [116]. Epsilon's strong flux was attributed to an extremely low neutral column density, with n_e <.002 cm^{-3} and N(H I)=$.7 - 1.2 \times 10^{18}$ cm^{-2}.

The EUVE observations were not well matched by either LTE or nLTE models with T=21,000K and log g=3.2, showing higher than predicted flux in the Lyman and helium continua. By examining Epsilon's mid-IR flux, which was assumed to be generated in the same layer at the LyC, the LyC region was estimated to be 2000 K hotter than predicted by stellar models. On this basis, blackbody curves matching the mid-IR observations were generated for the stellar interior, attenuated in the EUV by neutral hydrogen, and compared to the observations to predict a $.7 - 1.2 \times 10^{18}$ cm^{-2} N (H I) column density as shown in Table D.1.

A variety of absorption lines were identified in the EUVE observations, as well as wind and emission lines. It was noted that heavy line-blending was present, with almost all absorption features generated by a minimum of two transitions.

B.8 UVSTAR, 1995

UVSTAR [42] was a shuttle-based UV spectrograph present on the STS 69 and STS 95 shuttle missions (1995-1998) that observed Epsilon CMa between 575 and 1250 Å with a resolving power of R=∼300. The raw data of the observations is not publicly accessible. The observation suffered from scattered FUV light, limiting the accuracy of the flux calibration in the EUV, which was found to have higher levels of flux than than measured by EUVE. The mission nonetheless identified a variety of FUV and EUV lines in the spectrum while noting that the large number of lines rendered line identification difficult. The FUV spectra were well-matched by an ATLAS9 model with T=21,500, log g=3.2, [M/H]= 0.0, ξ = 8 km/s or by an Aufdenberg model with T=21,750, log g=3.5, [M/H] = 0.0, ξ =8 km/s. Rapid, unexplained flux variation were also observed in the 949-962, 977-990, 1040-1052, and 1074-1079 Å wavelength bands. The EUV data was not well fit by the models and showed a different overall shape and stronger line intensities than predicted. The final conclusion of the mission was that the EUV results were likely not well calibrated or were impacted by stellar variability.

B.9 ORFEUS SPAS II, 1996

The Berkeley spectrograph aboard the shuttle based ORFEUS-SPAS II EUV mission [17] obtained a count-space spectra of Epsilon CMa from 520-665 Å with a resolving power of R=1250. Although the spectrum is uncalibrated, the spectrograph was estimated to have roughly 3 times the effective area of EUVE in this bandpass. The spectrum is accessible online through the MAST archive under BEFS data.

The observations were compared to a TLUSTY 21,000 K log g=3.2 nLTE synthetic spectrum, as well as hotter models. Asymmetric wind features were observed mostly in O V, along with spectral features from He I, N II, Ar II, Ar III, Fe III, Fe IV, S IV, Cl III, Si III, C II, Cr IV, O II, O III, O IV, O V, and Ni III. Even with a resolving power of 1250, the spectrum suffered from high line blending due to a high density of features, and it is not clear that the continuum level of the spectrum was ever observed.

During the same ORFEUS SPAS II mission, spectra of Epsilon were also obtained with the Interstellar Medium Absorption Profile Spectrograph (IMAPS) instrument [56] at a resolution of 60,000 and spectral coverage from 950-1150 Å. The 1039 O I line was specifically observed; although it was contaminated with telluric O I, it helped constrain fits for later O I observations and H I column density estimates [45].

B.10 BDSR, 1996

The Big Dog Sounding Rocket (BDSR) [120, 124] attempted to obtain a 600-920 Å spectrum of Epsilon CMa in 1996, but did not succeed due to high levels of scattered light.

B.11 GHRS, 2001

Epsilon CMa was initially observed with the GHRS aboard the Hubble Space Telescope using the G160M (1150-2100 Å) grating at a resolution of R=20,000 and the Echelle B grating (1677-3209 Å) at R=85,000 due to a failure of the higher resolution Echelle A mode [46]. Epsilon

was later revisited by GHRS using the repaired Echelle A grating (1050-1729 Å) at a resolution of R=∼100,000 [45]. These high-resolution observations confirmed and identified multiple diffuse clouds on the sightline to Epsilon and constrained their abundances, temperatures, electron densities, and ionization fractions, including the neutral hydrogen column along the full sightline. The spectra obtained in both sets of observations are available on the MAST archive.

B.12 STIS, 2017

STIS spectra of Epsilon CMa were taken at a resolving power of R=120,000 from 1160-1348 Å and 2330-3047 Å and a resolving power of R=30,000 from 1167-2364 Å as part of the ASTRAL catalog [3].

B.13 JUNO UVS, 2019

The JUNO UVS instrument [54] is a photon-counting imaging spectrograph operating from 680-2100 Å with resolving power R=52 at 680 Å. En route to Jupiter on its main mission, JUNO-UVS observed several B stars, including Epsilon CMa, for calibration of the spectrograph against IUE archival data. This data was low resolution and did not detect any signal below approximately 1000 Å, where the UVS had a low efficiency.

B.14 FUSE/COS, —

No Far Ultraviolet Spectroscopic Explorer (FUSE) [85] or Cosmic Origins Spectrograph (COS) [38] spectra of Epsilon were ever taken because Epsilon exceeds the bright object limits of each instrument.

B.15 Compilation of UV studies

Mission	Year	Bandpass (Å)	Resolving Power	Citation
OAO-2	1968	1160-3600	100	[15]
TD-1	1975	1350-2750	~ 56	[55]
Copernicus	1977	912-1560	$\sim$5000,$\sim$20,000	[107]
IUE	1978	1150-3200	15,000	[4]
Voyager 1	1982	500-1700	30-115	[71],[98]
ROSAT	1992	600 (520-730)	photometry	[52]
EUVE	1993	70-730	$\sim$250	[10]
UVSTAR	1995	500-1250	~ 300	[42]
ORFEUS-SPAS II (Berkeley)	1996	520-665	1250	[17]
ORFEUS-SPAS II (IMAPS)	1996	950-1150	60,000	[45],[56]
GHRS	2001	1190-1550	$\sim$100,000	[45]
STIS	2017	1160-3047	120,000/60,000	[3]
JUNO	2019	680-2100	52	[54]

Table B.1: Previous UV Observations of Epsilon CMa

Appendix C

Stellar parameters of Epsilon CMa

Estimates of the stellar parameters of temperature, angular diameter, distance/parallax, stellar radius, surface gravity, and metallicity for Epsilon CMa are provided in the sections below. The methods used to obtain the estimates are briefly outlined.

C.1 Temperature

T (K)	Method	Notes	Year	Citation
20,990 ± 760	IBF	Used in EUVE analysis [10]	1976	[16]
22,668 ± 332	IBF	-	1979	[115]
21,000	IBF	-	1982	[99]
24,750	BJ	-	1992	[33]
23,000	SLF	-	2008	[86]
22,010 ± 1400	IBF	-	2009	[126]
22,205	SLF	-	2012	[57]
22,500 ± 300	SLF	-	2015	[14]

Table C.1: Temperature estimates for Epsilon CMa.

IBF: Integrated Bolometric Flux. Uses the Stefan Boltzmann law to estimate a star's temperature given its angular diameter and its bolometric luminosity integrated across the entire spectrum. May use model spectra to fill in gaps in observations.

SLF: Spectral Line Fitting. Compares observed stellar spectra to a variety of synthetic line profiles and finds the best-fit stellar parameters. Requires high resolution spectra and relies on stellar models and line-formation computations.

BJ: Balmer jump. Correlates the magnitude of the Balmer jump of a star to its temperature.

C.2 Angular diameter

Angular diameter (mas)	Method	Year	Citation
$.77 \pm .05$	IF	1974	[49]
$.775 \pm .055$	MP	1979	[115]
$.79 \pm .004$	MP	1982	[99]

Table C.2: Angular diameter estimates for Epsilon CMa

IF: Direct interferometry.

MP: Model Prediction. A star's angular diameter is computed by comparing its monochromatic flux emergent at Earth to its surface flux as predicted by stellar models.

C.3 Distance/parallax

Various other references similar to [68] (e.g. [115]) exist for estimates of Epsilon CMa's distance prior to measurement by Hipparcos, and were typically obtained by assuming an absolute magnitude from its spectral type and calculating a distance given its apparent magnitude. I judged these methods to be inferior to the dedicated Hipparcos measurements for parallax and did not include them.

Although the GAIA [31] satellite has produced updated parallax for a large number of stars, Epsilon CMa was not included in either GAIA DR1 or GAIA DR2 as it exceeded the $G(\approx V)= 3$ bright magnitude limit of the survey.

Parallax (mas)	Distance (pc)	Notes	Year	Citation
-	188 pc	Used in EUVE analysis [10]	1972	[68]
$7.57 \pm .57$	132.1 ± 9.9	-	1997	[95]
$8.05 \pm .14$	124.2 ± 2.2	-	2007	[118]

Table C.3: Distance estimates for Epsilon CMa

C.4 Radius

Radius (R_{sun})	Method	Notes	Year	Citation
12.7	FOP	Pre-Hipparcos	1979	[115]
12.7	FOP	Pre-Hipparcos	1982	[99]
8.9	ET	Pre-Hipparcos	1992	[33]
16.2 ± 1.2	FOP	Pre-Hipparcos	1995	[10]
11.3 ± 1.1	MF	-	1998	[2]
$12.0^{+1.7}_{-1.5}$	ET	Using stellar tracks from [32]	2015	[14]
$10.1^{+.7}_{-.5}$	ET	Using stellar tracks from [6]	2015	[14]

Table C.4: Radius estimates for Epsilon CMa

FOP: From Other Parameters. A star's radius is computed from other parameters including angular diameter, distance, and effective temperature. This method is as reliable as the input parameters.

ET: Evolutionary Tracks. Derives stellar properties by comparing observations to simulated evolutionary tracks.

MF: Model Fitting. Observed spectra are fit by stellar models which predict stellar parameters.

C.5 Surface gravity, log g

Log g	Method	Year	Citation
3.65	BLF	1992	[33]
3.19 ± .15	-	1993	[52]
3.2 ± .15	BLF	1995	[10]
3.39	MF	2004	[72]
3.3 ± .15	BLF	2008	[86]
3.35 ± .45	MF	2012	[57]
3.4 ± .08	MF	2015	[14]

Table C.5: Surface gravity estimates for Epsilon CMa

BLF: Balmer Line Fitting. Balmer line profiles are fit and compared to synthetic line profiles to yield stellar temperature and surface gravity.

C.6 Metallicity

Metallicity [Fe/H]	Method	Citation
.01 ± .18	MF	[57]

Table C.6: Metallicity estimates for Epsilon CMa

Appendix D

Historical N(H I) estimates for the Epsilon CMa sightline

The main techniques used to obtain N(H I) column densities to nearby stars in the ISM are briefly reviewed. All known N(H I) estimates for the Epsilon CMa sightline are tabulated in Table D.1.

D.1 N(H I) estimates

D.1.1 Ly-α absorption fitting

Early estimates of Epsilon's N(H I) sightline utilized H I 1216 Å Lyman Alpha (Ly-α) fitting, where the interstellar Ly-α line and surrounding continuum are observed and N(H I) is estimated by removing the effects of a N(H I) damping absorption profile from the spectrum until the Ly-α line matches the continuum level ("continuum reconstruction" [5]). This technique assumes that the Ly-α line exhibits a pure damping profile and that it is separable from the underlying stellar line and other contaminating spectral lines like Si III 1206 Å. These conditions are largely met for spectral types B2-3 and earlier and for N(H I) columns above $5 - 10 \times 10^{18}\ cm^{-2}$. For stars later than B3, the stellar Ly-α line is too strong and contaminates the spectrum, while for lower column densities the stellar line makes up an appreciable fraction of the observed line profile, rendering continuum placement difficult. Geocoronal Ly-α is typically narrower than the interstellar line and does not affect the fits.

Considering these limitations, Ly-α absorption fitting of Epsilon CMa is rendered difficult due to Epsilon's low column density. All estimates of its N(H I) column by this method have

significant uncertainties or are only an upper limit due to the unknown contribution of stellar Ly-α to the line profile.

D.1.2 Line proxies

Another technique to estimate N(H I) comes from the observed and calculated relationship between hydrogen and other proxy absorption lines in both the optical and the ultraviolet. Typically, multiple stellar lines are observed from both neutral and highly ionized regions of the ISM (e.g. [46]) in as high resolution as possible (ideally R>100,000). These observations are then fit with Voigt profiles convolved with instrumental broadening, characterizing the clouds producing the lines according to column density, radial velocity, and the broadening/thermal b value. Multiple lines of the same element, with different oscillator strengths, are typically fit simultaneously to a single shared column density for each individual cloud to ensure consistency ([30]). The total sightline column density for that species is the sum of the column densities the species for the individual clouds. Finally, a relationship between the abundance of an observed species and neutral hydrogen (e.g. Na I, [25], N I, OI, [45]) is used to estimate the N(H I) column to the star.

Limitations of this technique include error in the observed equivalent widths used to derive cloud column densities, assumptions about ISM metallicities/elemental depletion rates, error in the relationships between various species and N(H I), and the fact that these general relationships may not apply to specific sightlines in the ISM.

D.1.3 EUV observation with attenuated models

The most direct method for estimating N(H I) is through comparison between EUV observations of a star and stellar EUV models accounting for N(H I) attenuation. In this method, a star is directly observed by ultraviolet, space based instruments in the 50-912 Å region (e.g. [36]). Since the observation consists of the intrinsic stellar spectrum attenuated by the N(H I) sightline, it can be compared to models including simulated N(H I) attenuation (Section 1.5) to obtain the column density. As this method is both direct and requires few assumptions, it is generally considered

the most accurate method for estimating N(H I) column densities [30]. The DEUCE model fitting described in Chapter 4 utilizes this method for N(H I) estimation.

D.2 Table of N(H I) estimates

N(H I) $[cm^{-2}]$	Method	Year	Citation
$1 - 4 \times 10^{18}$	Ly-α, OAO-2	1972	[100]
$< 5 \times 10^{18}$	Ly-α, Copernicus	1975	[5]
$< 3.0 \times 10^{19}$	Ly-α, IUE	1985	[105]
$< 3.5 \times 10^{18}$	Proxy, Na I, using [25]	1991	[119]
$< 9 \times 10^{17}$	EUV Observation, ROSAT	1993	[52]
$1.05 \pm .05 \times 10^{18}$	EUV Observation, EUVE	1993	[117]
$< 2.95 \pm .94 \times 10^{19}$	Ly-α, IUE	1994	[20]
$< 4 \times 10^{19}$	Proxy, Na I, using [53]	1994	[30]
$7 \times 10^{17} - 1.2 \times 10^{18}$	EUV Observation, EUVE	1995	[10]
$< 5 \times 10^{17}$	Proxy, N I, Mg II, using [24]	1995	[46]
$< 2 \times 10^{17}$	Proxy, S II + others, GHRS	1998	[44]
$4.8 \times 10^{17} - 1.1 \times 10^{18}$	Proxy, O I, using [84]	2001	[45]

Table D.1: Previous sightline N(H I) estimates for Epsilon CMa

Appendix E

All 1 and 2D confidence intervals for the EUV model fitting

The following pages present the 1D singular N(H I) and 2D joint (T, N(H I)) confidence intervals determined by least squares minimization for all combinations of model (ATLAS9, TLUSTY, Aufdenberg N2, Aufdenberg N7) and EUV observation (DEUCE, EUVE, DEUCE and EUVE). In each plot, the green, yellow, and blue regions respectively refer to the 1, 2, and 3σ confidence regions determined by the fit, while the best-fit solution is marked by either a vertical dashed black line or a red X.

E.0.1 ATLAS9, DEUCE

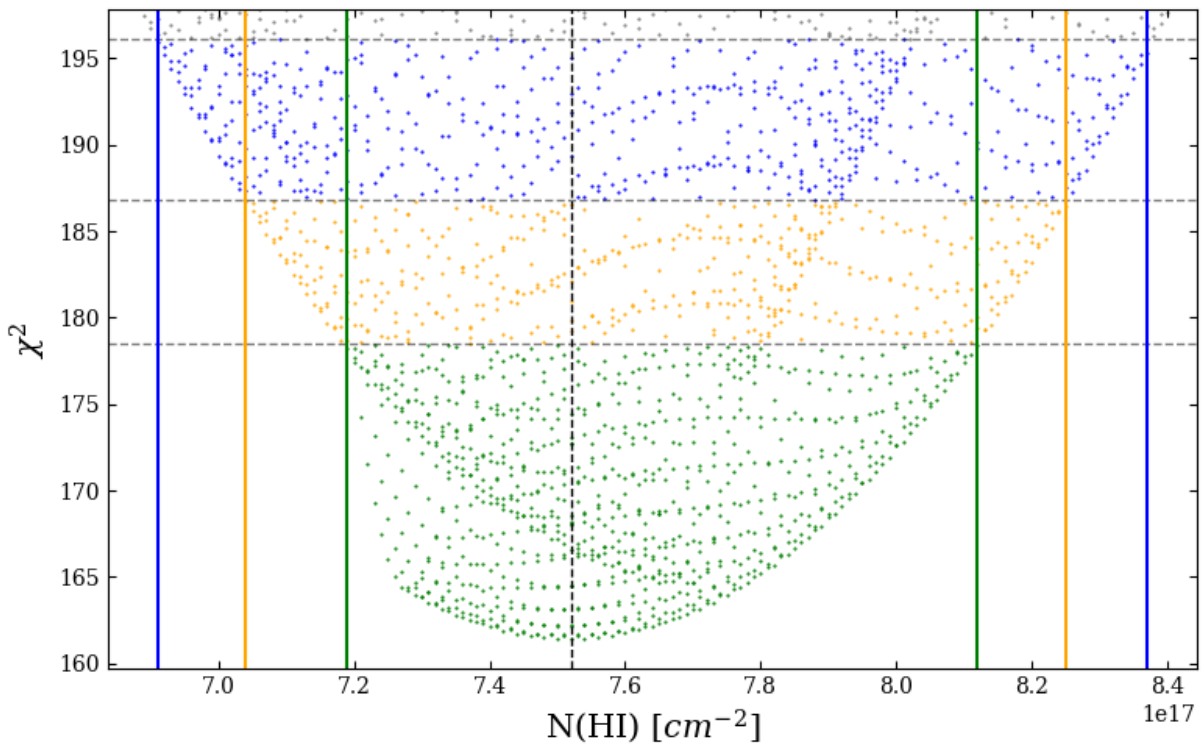

Figure E.1: N(H I) vs χ^2 plot with 1, 2, and 3σ N(H I) individual confidence intervals, shown for the ATLAS9 model compared to the DEUCE data.

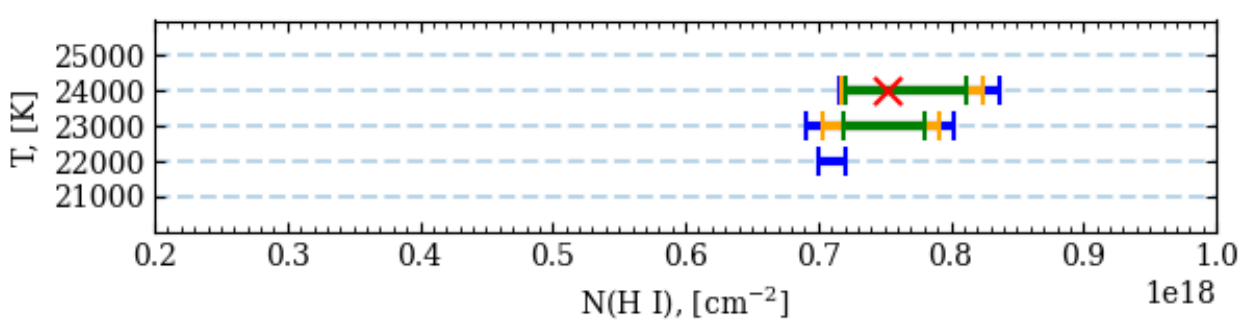

Figure E.2: Joint confidence intervals for T vs N(H I), with 1, 2, and 3σ N(H I) intervals, shown for the ATLAS9 model compared to the DEUCE data.

E.0.2 ATLAS9, EUVE

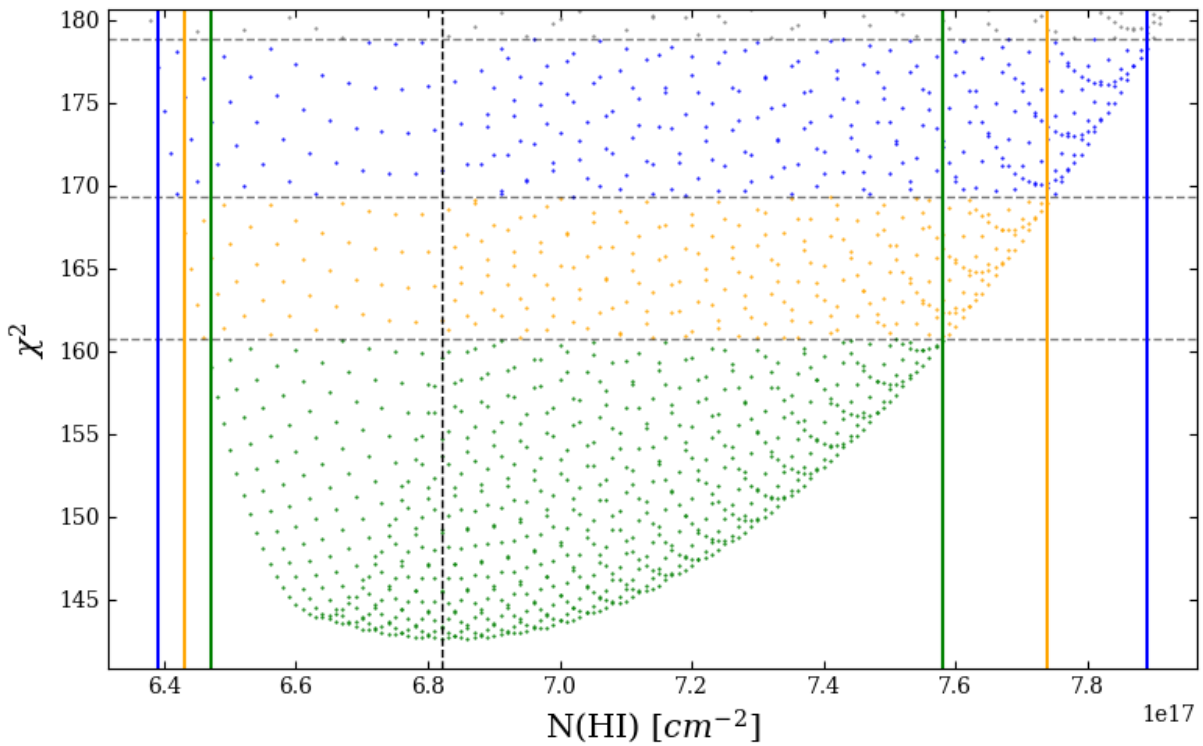

Figure E.3: N(H I) vs χ^2 plot with 1, 2, and 3σ N(H I) individual confidence intervals, shown for the ATLAS9 model compared to the EUVE data.

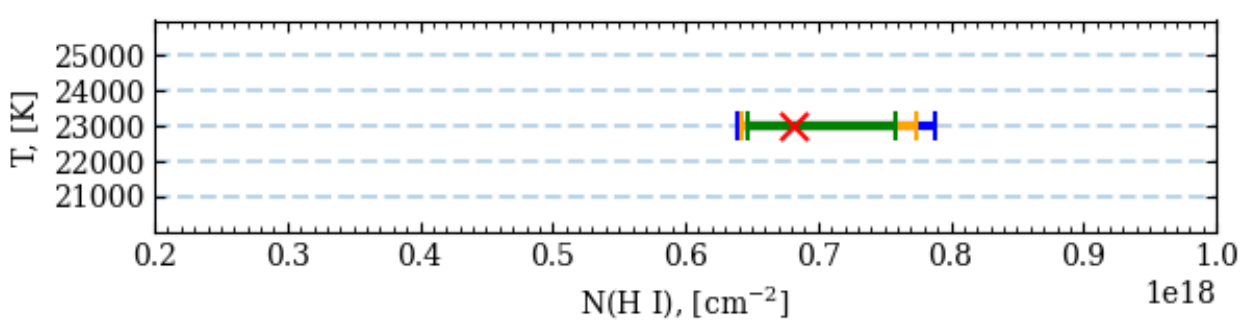

Figure E.4: Joint confidence intervals for T vs N(H I), with 1, 2, and 3σ N(H I) intervals, shown for the ATLAS9 model compared to the EUVE data.

E.0.3 ATLAS9, DEUCE and EUVE

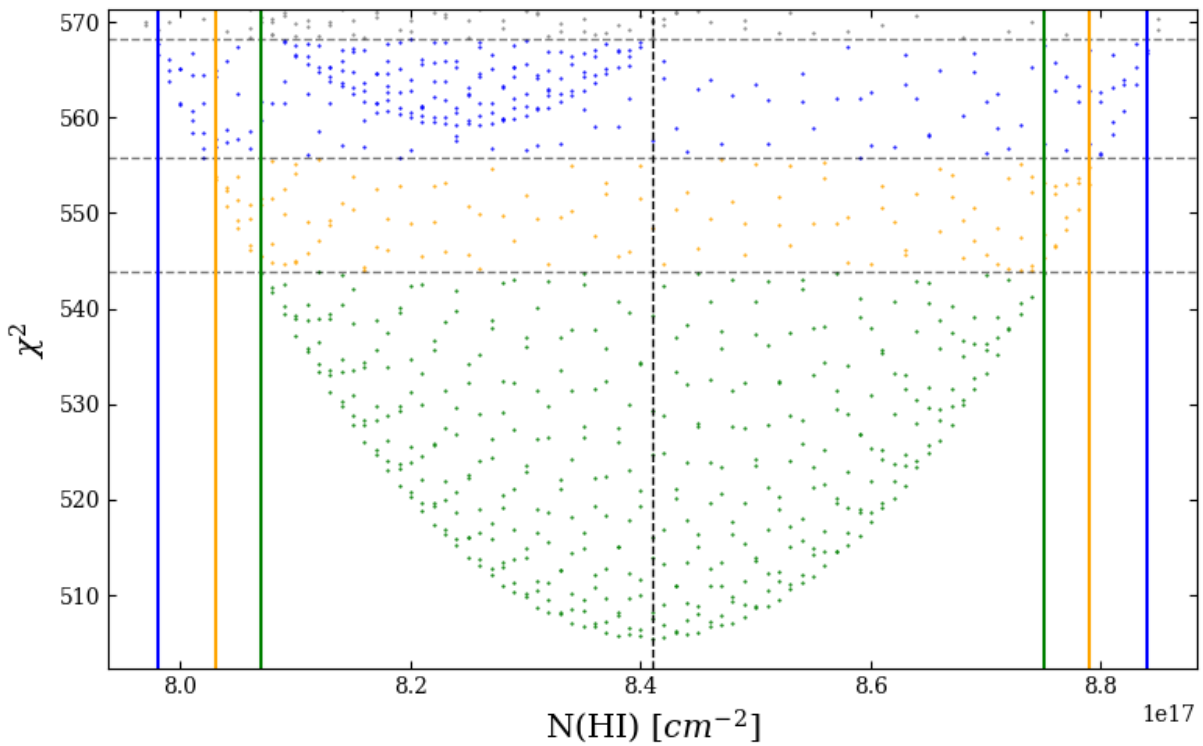

Figure E.5: N(H I) vs χ^2 plot with 1, 2, and 3σ N(H I) individual confidence intervals, shown for the ATLAS9 model compared to the combined EUVE and DEUCE data.

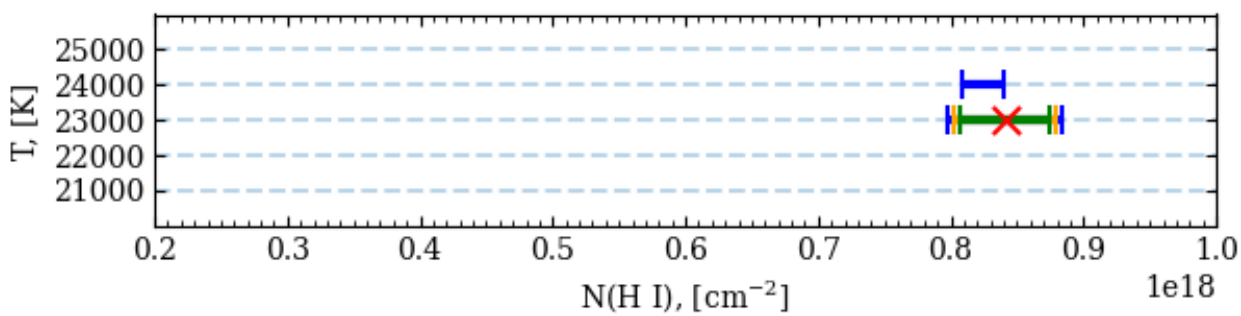

Figure E.6: Joint confidence intervals for T vs N(H I), with 1, 2, and 3σ N(H I) intervals, shown for the ATLAS9 model compared to the combined EUVE and DEUCE data.

E.0.4 TLUSTY, DEUCE

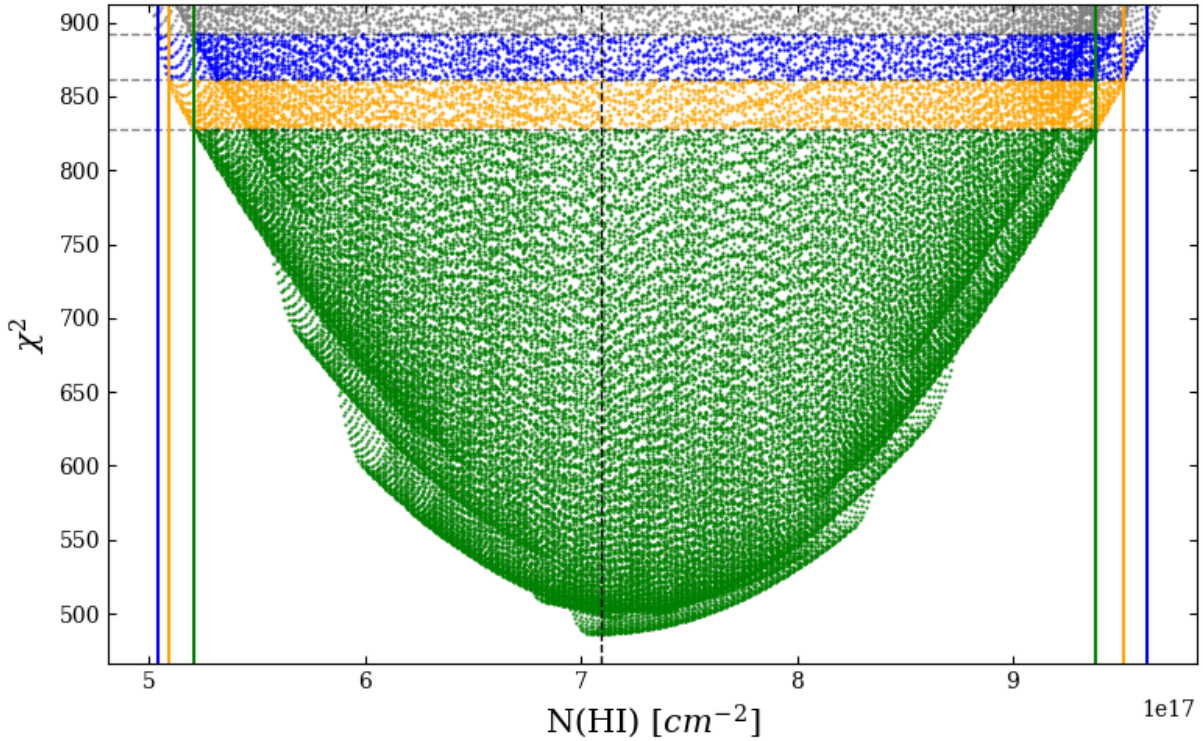

Figure E.7: N(H I) vs χ^2 plot with 1, 2, and 3σ N(H I) individual confidence intervals, shown for the TLUSTY model compared to the DEUCE data.

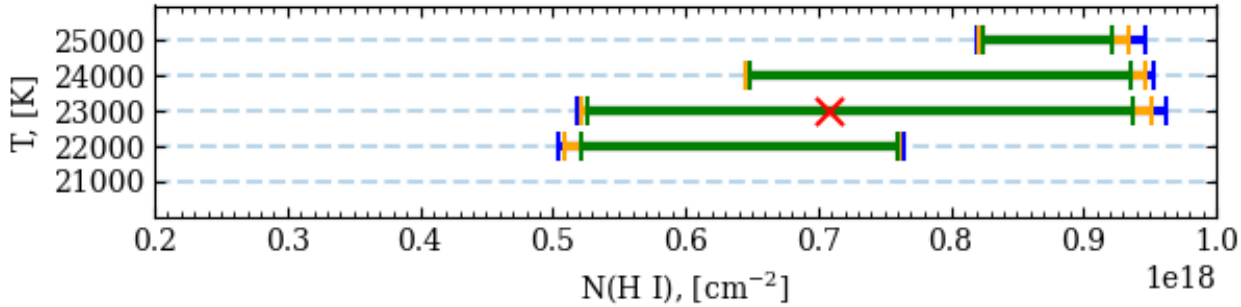

Figure E.8: Joint confidence intervals for T vs N(H I), with 1, 2, and 3σ N(H I) intervals, shown for the TLUSTY model compared to the DEUCE data.

E.0.5 TLUSTY, EUVE

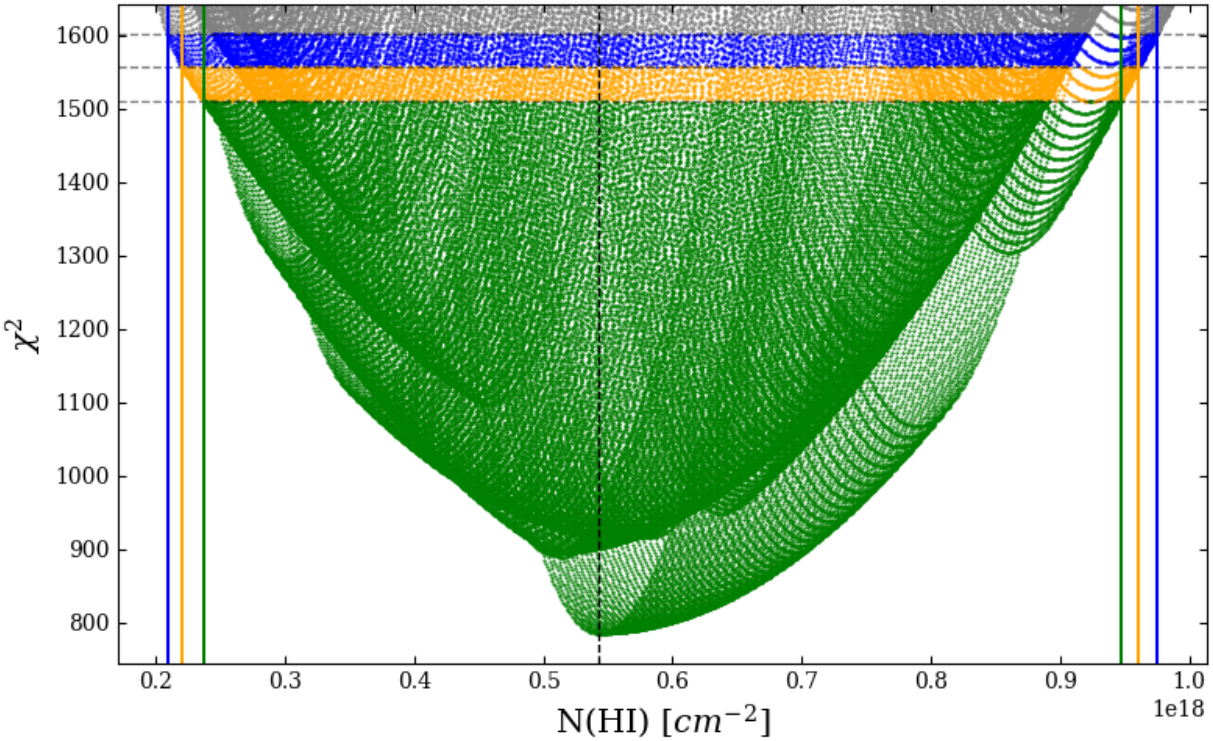

Figure E.9: N(H I) vs χ^2 plot with 1, 2, and 3σ N(H I) individual confidence intervals, shown for the TLUSTY model compared to the EUVE data.

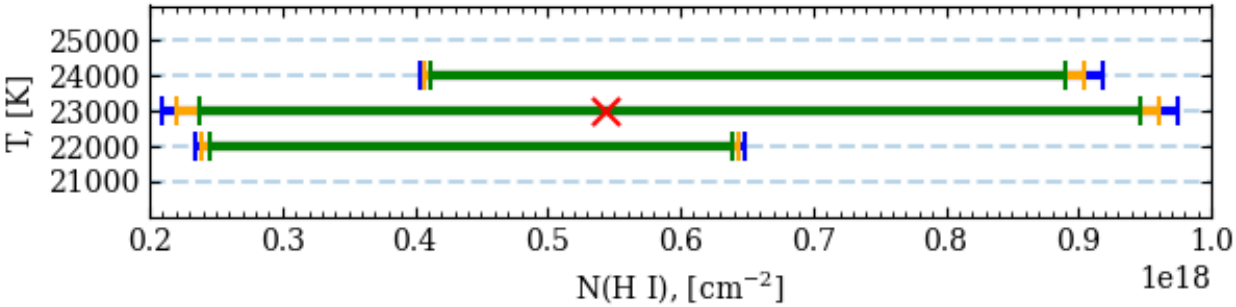

Figure E.10: Joint confidence intervals for T vs N(H I), with 1, 2, and 3σ N(H I) intervals, shown for the TLUSTY model compared to the EUVE data.

E.0.6 TLUSTY, DEUCE and EUVE

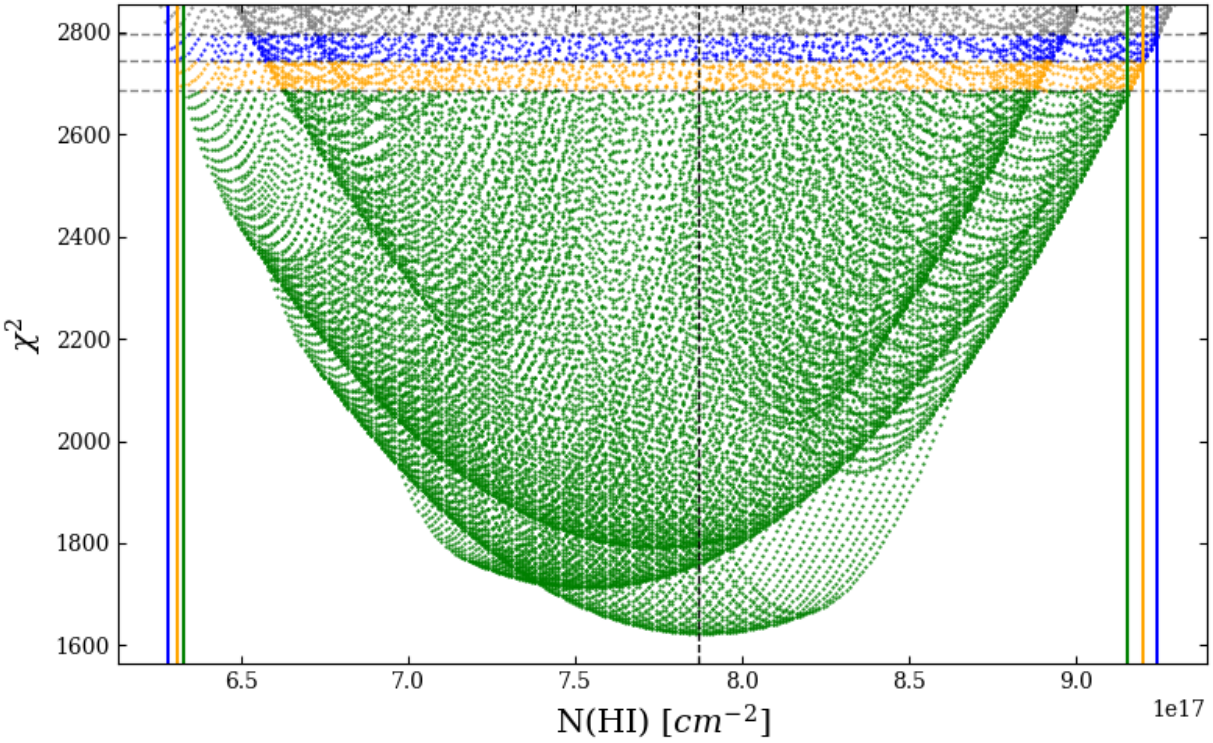

Figure E.11: N(H I) vs χ^2 plot with 1, 2, and 3σ N(H I) individual confidence intervals, shown for the TLUSTY model compared to the combined EUVE and DEUCE data.

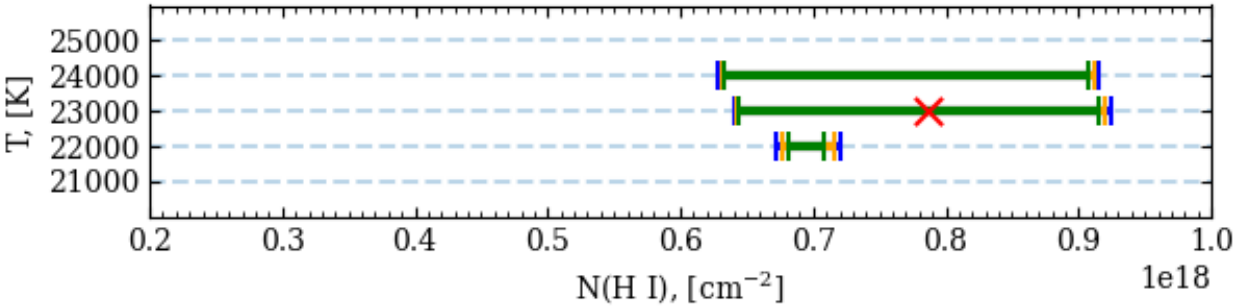

Figure E.12: Joint confidence intervals for T vs N(H I), with 1, 2, and 3σ N(H I) intervals, shown for the TLUSTY model compared to the combined EUVE and DEUCE data.

E.0.7 Aufdenberg N2, DEUCE

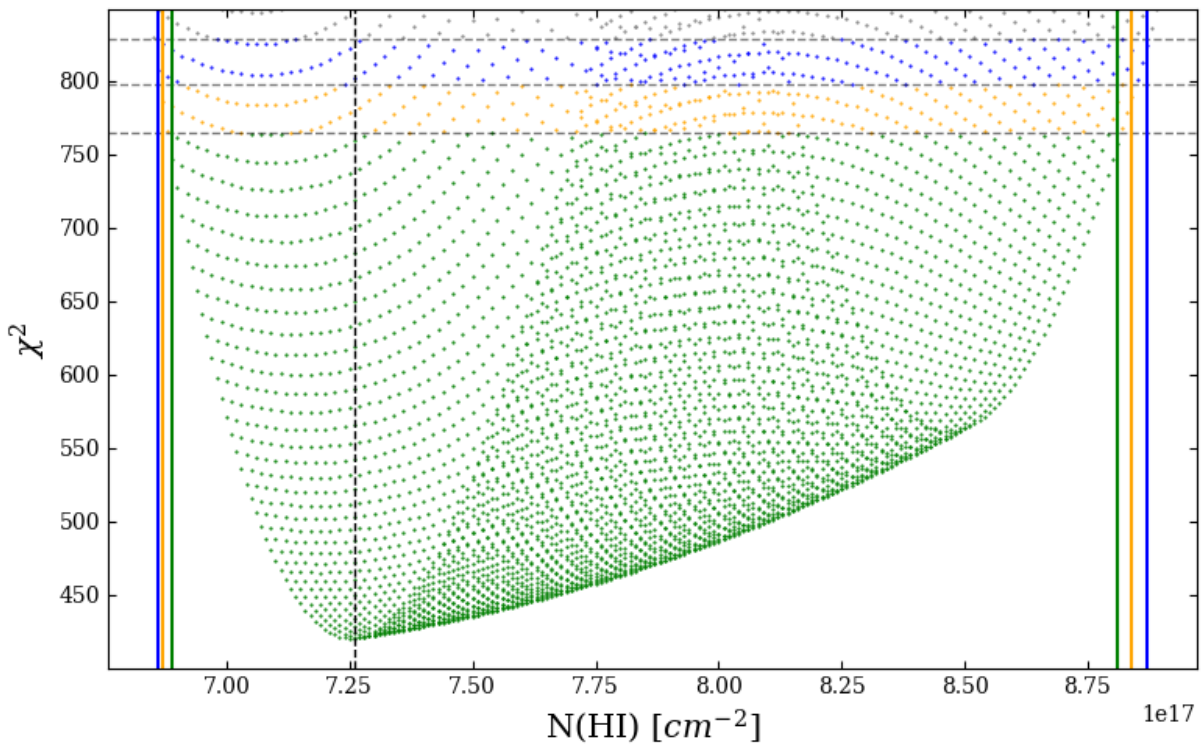

Figure E.13: N(H I) vs χ^2 plot with 1, 2, and 3σ N(H I) individual confidence intervals, shown for the Aufdenberg N2 model compared to the DEUCE data.

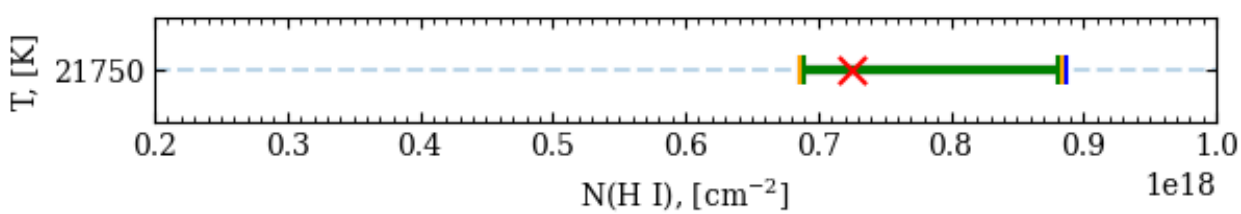

Figure E.14: Joint confidence intervals for T vs N(H I), with 1, 2, and 3σ N(H I) intervals, shown for the Aufdenberg N2 model compared to the DEUCE data.

E.0.8 Aufdenberg N2, EUVE

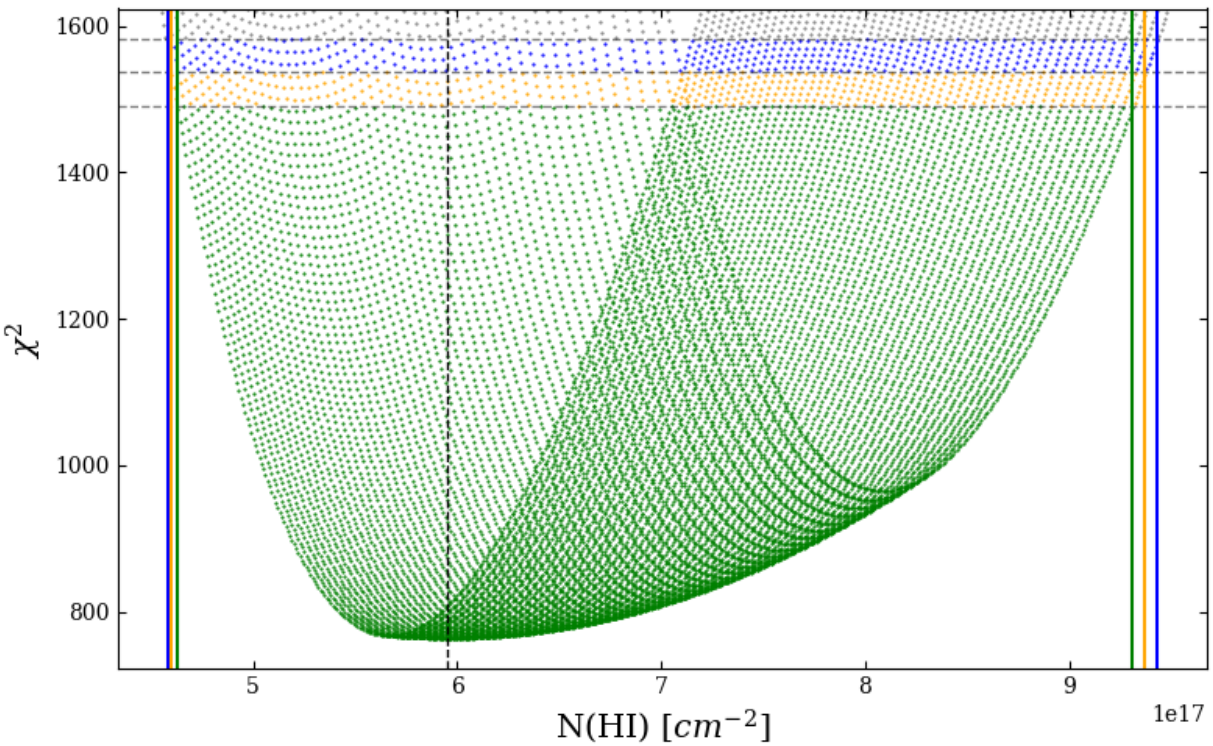

Figure E.15: N(H I) vs χ^2 plot with 1, 2, and 3σ N(H I) individual confidence intervals, shown for the Aufdenberg N2 model compared to the EUVE data.

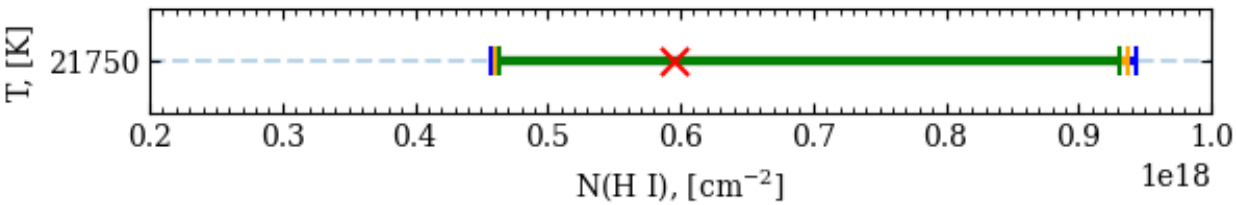

Figure E.16: Joint confidence intervals for T vs N(H I), with 1, 2, and 3σ N(H I) intervals, shown for the Aufdenberg N2 model compared to the EUVE data.

E.0.9 Aufdenberg N2, DEUCE and EUVE

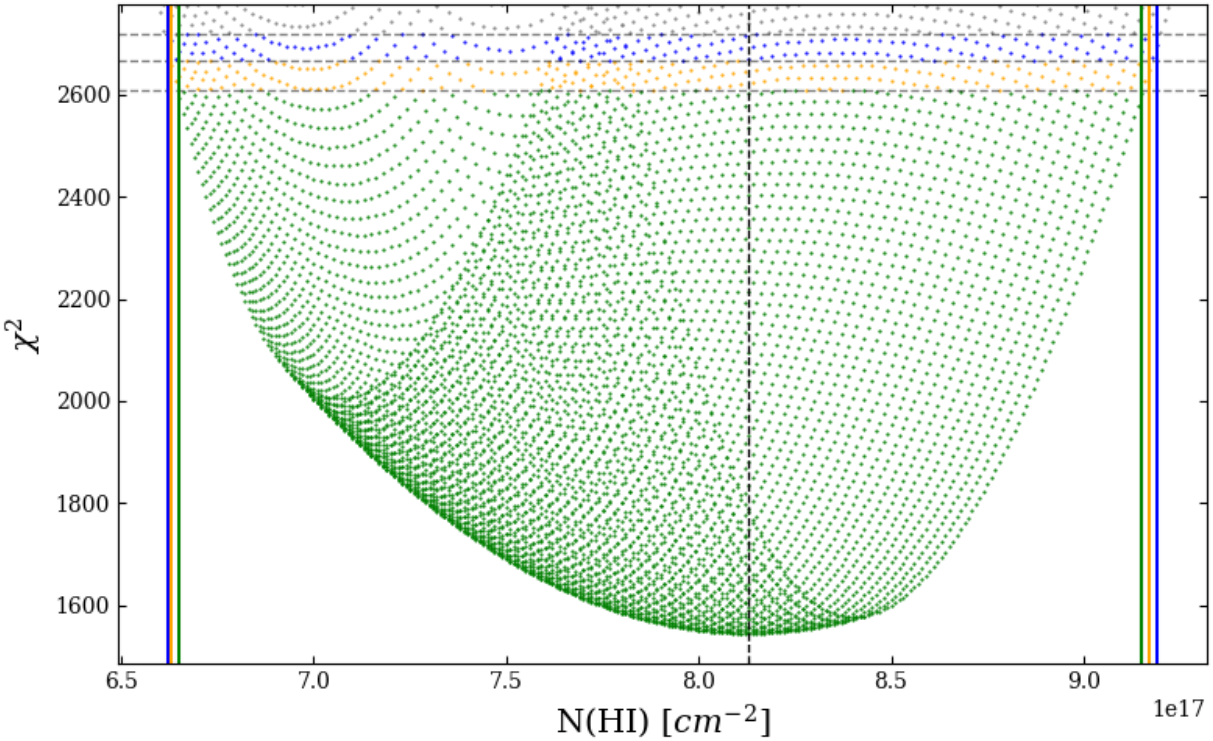

Figure E.17: N(H I) vs χ^2 plot with 1, 2, and 3σ N(H I) individual confidence intervals, shown for the Aufdenberg N2 model compared to the combined EUVE and DEUCE data.

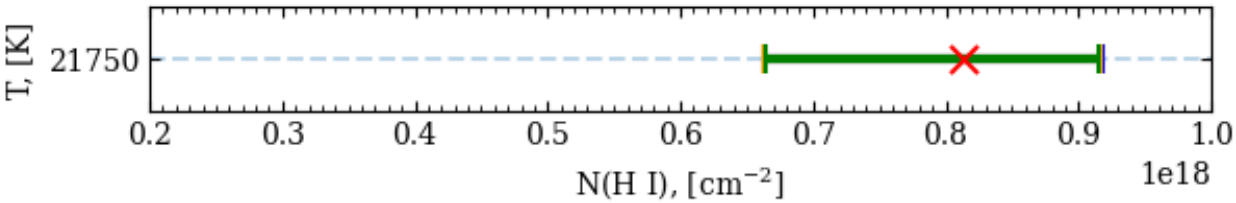

Figure E.18: Joint confidence intervals for T vs N(H I), with 1, 2, and 3σ N(H I) intervals, shown for the Aufdenberg N2 model compared to the combined EUVE and DEUCE data.

E.0.10 Aufdenberg N7, DEUCE

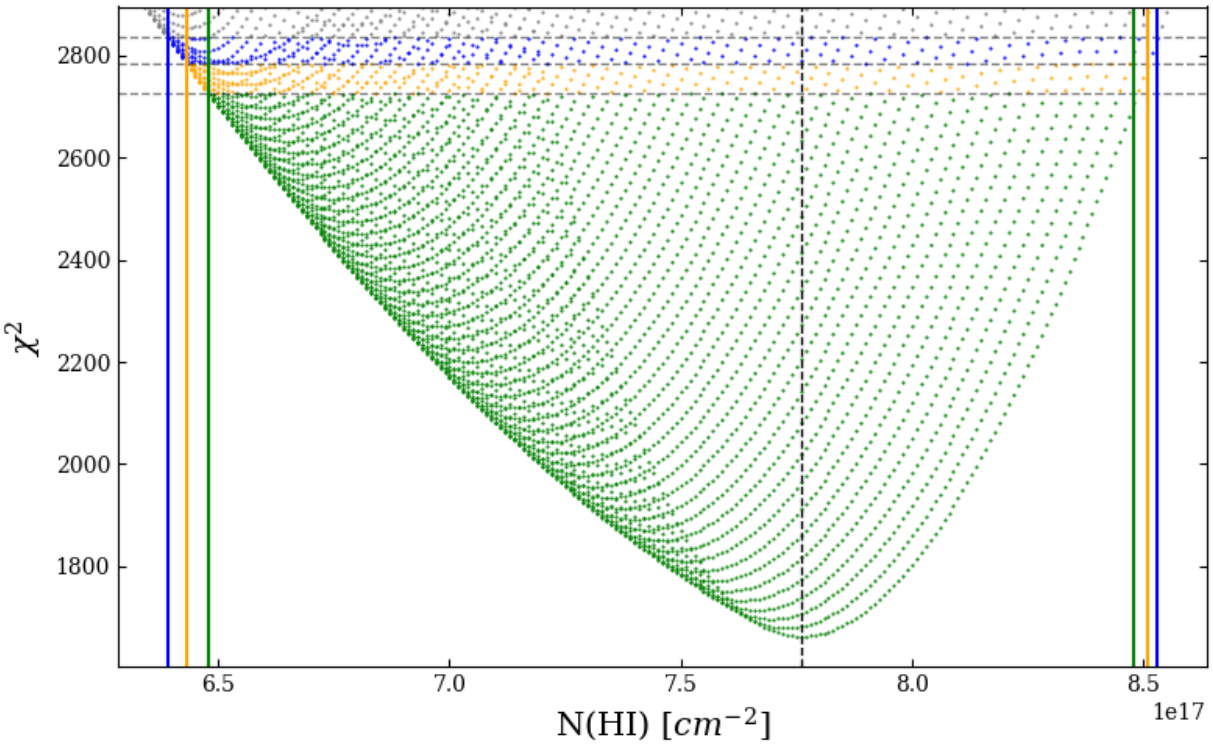

Figure E.19: N(H I) vs χ^2 plot with 1, 2, and 3σ N(H I) individual confidence intervals, shown for the Aufdenberg N7 model compared to the DEUCE data.

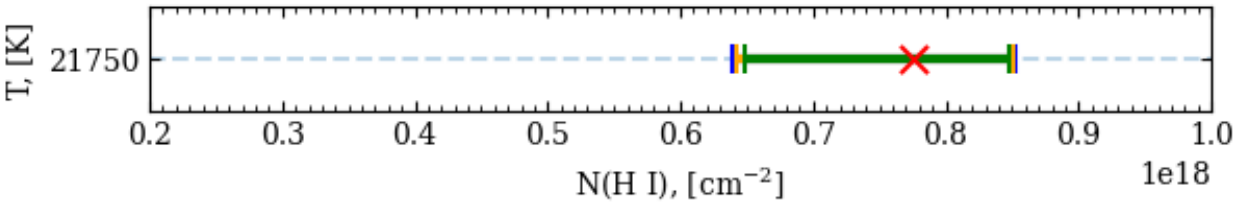

Figure E.20: Joint confidence intervals for T vs N(H I), with 1, 2, and 3σ N(H I) intervals, shown for the Aufdenberg N7 model compared to the DEUCE data.

E.0.11 Aufdenberg N7, EUVE

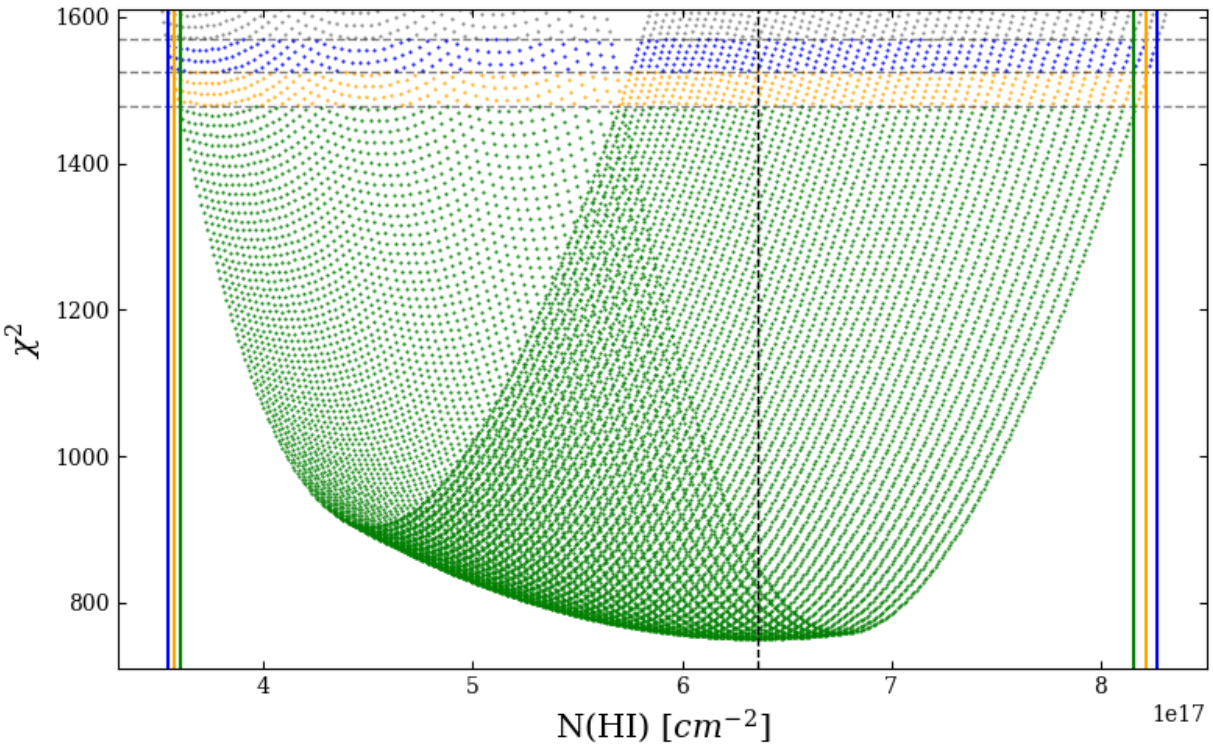

Figure E.21: N(H I) vs χ^2 plot with 1, 2, and 3σ N(H I) individual confidence intervals, shown for the Aufdenberg N7 model compared to the EUVE data

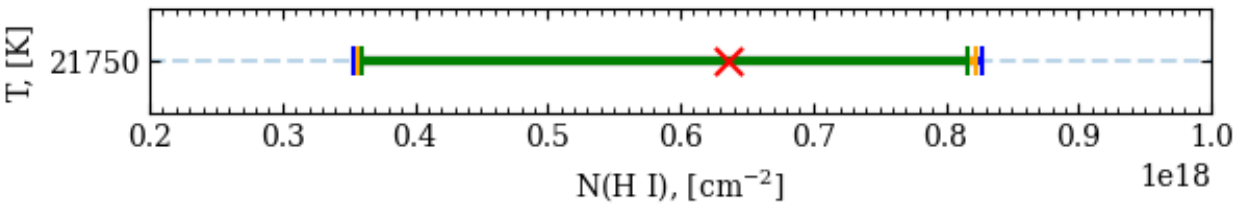

Figure E.22: Joint confidence intervals for T vs N(H I), with 1, 2, and 3σ N(H I) intervals, shown for the Aufdenberg N7 model compared to the EUVE data.

E.0.12 Aufdenberg N7, DEUCE and EUVE

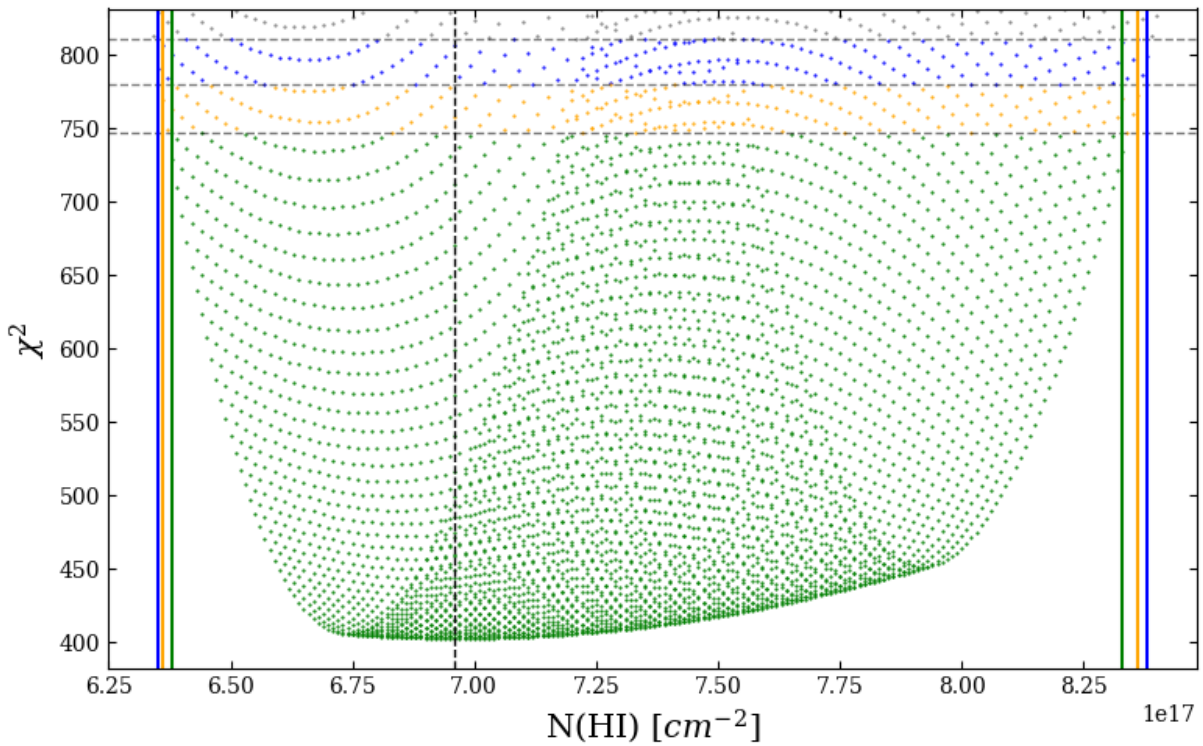

Figure E.23: N(H I) vs χ^2 plot with 1, 2, and 3σ N(H I) individual confidence intervals, shown for the Aufdenberg N7 model compared to the combined EUVE and DEUCE data

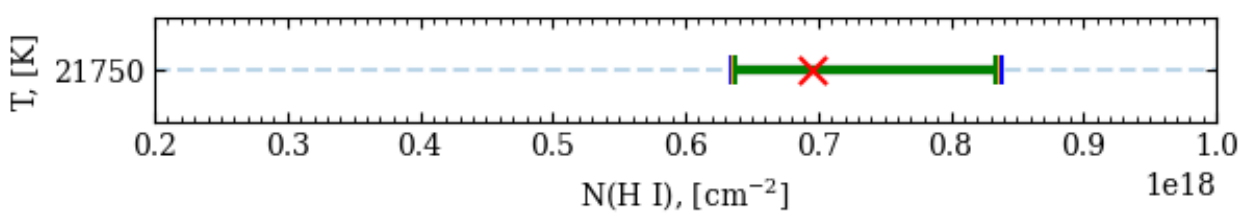

Figure E.24: Joint confidence intervals for T vs N(H I), with 1, 2, and 3σ N(H I) intervals, shown for the Aufdenberg N7 model compared to the combined EUVE and DEUCE data.